Ocean Modelling 130 (2018) 79–139

Contents lists available at ScienceDirect

Ocean Modelling

journal homepage: www.elsevier.com/locate/ocemod

JRA-55 based surface dataset for driving ocean–sea-ice models (JRA55-do)

Hiroyuki Tsujino[*,a], Shogo Urakawa[a], Hideyuki Nakano[a], R. Justin Small[b], Who M. Kim[b], Stephen G. Yeager[b], Gokhan Danabasoglu[b], Tatsuo Suzuki[c], Jonathan L. Bamber[d], Mats Bentsen[e], Claus W. Böning[f], Alexandra Bozec[g], Eric P. Chassignet[g], Enrique Curchitser[h], Fabio Boeira Dias[i,j,k,l], Paul J. Durack[m], Stephen M. Griffies[n], Yayoi Harada[a], Mehmet Ilicak[e,o], Simon A. Josey[p], Chiaki Kobayashi[a], Shinya Kobayashi[q], Yoshiki Komuro[c], William G. Large[b], Julien Le Sommer[r], Simon J. Marsland[l,k,j,i], Simona Masina[s,t], Markus Scheinert[f], Hiroyuki Tomita[u], Maria Valdivieso[v], Dai Yamazaki[c,v]

[a] JMA Meteorological Research Institute, Tsukuba, Japan
[b] National Center for Atmospheric Research (NCAR), Boulder, CO, USA
[c] Japan Agency for Marine-Earth Science and Technology (JAMSTEC), Yokohama, Japan
[d] University of Bristol, Bristol, UK
[e] Uni Research Climate, Bjerknes Centre for Climate Research, Bergen, Norway
[f] GEOMAR Helmholtz Centre for Ocean Research Kiel, Kiel, Germany
[g] Center for Ocean-Atmospheric Prediction Studies (COAPS), Florida State University, Tallahassee, FL, USA
[h] Rutgers University, New Brunswick, NJ, USA
[i] Institute for Marine and Antarctic Studies, University of Tasmania, Australia
[j] Antarctic Climate and Ecosystems Cooperative Research Centre, University of Tasmania, Australia
[k] ARC Centre of Excellence for Climate System Science, Australia
[l] CSIRO Oceans and Atmosphere, Australia
[m] Program for Climate Model Diagnosis and Intercomparison, Lawrence Livermore National Laboratory, Livermore, CA, USA
[n] NOAA Geophysical Fluid Dynamics Laboratory (GFDL), Princeton, NJ, USA
[o] Eurasia Institute of Earth Sciences, Istanbul Technical University, Istanbul, Turkey
[p] National Oceanography Centre (NOC), Southampton, UK
[q] Japan Meteorological Agency (JMA), Tokyo, Japan
[r] Université Grenoble Alpes/CNRS/IRD/G-INP, IGE,, Grenoble, France
[s] Centro Euro-Mediterraneo sui Cambiamenti Climatici (CMCC), Bologna, Italy
[t] Istituto Nazionale di Geofisica e Vulcanologia (INGV), Bologna, Italy
[u] Institute for Space-Earth Environmental Research (ISEE), Nagoya University, Nagoya, Japan
[v] University of Reading, Reading, UK

ARTICLE INFO

Keywords:
Ocean model forcing
Surface fluxes
COREs
OMIP
JRA55-do

ABSTRACT

We present a new surface-atmospheric dataset for driving ocean–sea-ice models based on Japanese 55-year atmospheric reanalysis (JRA-55), referred to here as JRA55-do. The JRA55-do dataset aims to replace the CORE interannual forcing version 2 (hereafter called the CORE dataset), which is currently used in the framework of the Coordinated Ocean-ice Reference Experiments (COREs) and the Ocean Model Intercomparison Project (OMIP). A major improvement in JRA55-do is the refined horizontal grid spacing (~ 55 km) and temporal interval (3 hr). The data production method for JRA55-do essentially follows that of the CORE dataset, whereby the surface fields from an atmospheric reanalysis are adjusted relative to reference datasets. To improve the adjustment method, we use high-quality products derived from satellites and from several other atmospheric reanalysis projects, as well as feedback on the CORE dataset from the ocean modelling community. Notably, the surface air temperature and specific humidity are adjusted using multi-reanalysis ensemble means. In JRA55-do, the downwelling radiative fluxes and precipitation, which are affected by an ambiguous cloud parameterisation employed in the atmospheric model used for the reanalysis, are based on the reanalysis products. This approach represents a notable change from the CORE dataset, which imported independent observational products. Consequently, the JRA55-do dataset is more self-contained than the CORE dataset, and thus can be continually updated in near real-time. The JRA55-do dataset extends from 1958 to the present, with updates expected at

* Corresponding author.
E-mail address: htsujino@mri-jma.go.jp (H. Tsujino).

https://doi.org/10.1016/j.ocemod.2018.07.002
Received 7 December 2017; Received in revised form 3 July 2018; Accepted 10 July 2018
Available online 27 July 2018

least annually. This paper details the adjustments to the original JRA-55 fields, the scientific rationale for these adjustments, and the evaluation of JRA55-do. The adjustments successfully corrected the biases in the original JRA-55 fields. The globally averaged features are similar between the JRA55-do and CORE datasets, implying that JRA55-do can suitably replace the CORE dataset for use in driving global ocean–sea-ice models.

1. Introduction

The framework of the Coordinated Ocean-ice Reference Experiments (COREs; Griffies et al. 2009, Danabasoglu et al. 2014) and the subsequent Ocean Model Intercomparison Project (OMIP; Griffies et al., 2016) provides ocean and climate modellers with a common facility for performing coupled global ocean–sea-ice simulations. This framework defines protocols for running coupled ocean–sea-ice models with boundary forcing derived from common atmospheric datasets. Its most essential element is the forcing dataset developed by Large and Yeager (2004; 2009), hereafter referred to as the CORE dataset, which is largely based on the surface-atmospheric fields derived from NCEP/NCAR atmospheric reanalysis (Kalnay et al. 1996; Kistler et al. 2001). To reduce biases and uncertainties in the reanalysis fields, surface-atmospheric fields such as winds, air temperature, and specific humidity are adjusted with respect to available observations. The reanalysis products also contain downward surface fluxes such as the downwelling shortwave and longwave radiative fluxes and precipitation (rain and snow), but these data are replaced by estimates that are more directly based on observational data, such as from satellites.

Although the CORE framework has become increasingly visible and successfully distributed, no significant developments or maintenance of the dataset or protocol have occurred since 2009. For the CORE dataset, the discontinuity in the source data for radiation fields is the main reason for prohibiting updates. Given that the scientific success of COREs has only recently been demonstrated to the broader community, this situation might be expected. However, the foundation of CORE/OMIP cannot remain frozen indefinitely. Furthermore, although the present CORE dataset and protocol have become widely used, there are various shortcomings revealed through many recent studies based on the CORE protocol (Griffies et al. 2009; Danabasoglu et al. 2014; Griffies et al. 2014; Downes et al. 2015; Farneti et al. 2015; Wang et al. 2016a; 2016b; Ilicak et al. 2016; Danabasoglu et al. 2016; Tseng et al. 2016). Hence, there is an urgent need to advance the scientific and engineering foundation of the CORE/OMIP framework. This advance must proceed in a timely manner to benefit ocean modelling communities around the world.

The ocean modelling community requires the following features of a forcing dataset:

- All forcing datasets must be up-to-date (currently, the CORE dataset is available only through 2009).
- The datasets must not be tuned and adjusted to improve simulation results of a particular ocean–sea-ice model or to conform to a particular choice of a set of numerical schemes and parameters for ocean interior processes in coupled ocean–sea-ice models.
- The heat and water budgets of forcing datasets must be balanced with respect to the applied surface flux bulk formulae.
- The spatial and temporal resolutions of the datasets must be as sufficient as possible for forcing high-resolution (e.g., eddying, coastal) ocean and sea-ice models. The horizontal resolution of the CORE dataset is approximately 200 km (T62 grids).
- All available datasets, such as other reanalysis products, and radiation datasets, should be considered.
- The datasets should be extended to include pre-1948 data.

The CORE dataset satisfied only the second (no model-based tuning) and third (global balance) items in the above list.

The following scientific and engineering backgrounds of forcing datasets also warrant revisiting:

- The assumptions and corrections made in Large and Yeager (2009), who created the CORE dataset;
- Incorporation of new corrections based on new/different observational data;
- Forcing over regions covered by sea-ice;
- Surface ocean wave fields;
- River runoff field, including runoff from ice-sheet melting;
- Diurnal cycling of wind and solar radiation.

By referring to new datasets that resolve some of the above issues, ocean modellers hope to better simulate recent extreme climate events, such as sea-ice reduction in the Arctic and the on-going El Niño/La Niña cycle, and to understand these events in the context of long-term variability. The present developmental study is an international collaborative effort to produce a new atmospheric dataset for driving coupled ocean–sea-ice models. Based on the Japanese 55-year Reanalysis (JRA-55; Kobayashi et al., 2015) project conducted by the Japan Meteorological Agency (JMA), it aims to complement and eventually replace the existing forcing dataset from Large and Yeager (2009).

JRA-55 is among the more recent long-term reanalysis projects. It adopts a relatively high-resolution (~ 55 km) atmospheric model and uses state-of-the-art assimilation techniques. The dataset extends from 1958 to the present, and will be updated in forthcoming years as part of the JMA operational climate services. All atmospheric variables necessary for computing surface fluxes are taken from the forecast phase of JRA-55. The temporal interval is 3 h. Data are originally provided on the reduced TL319 (~ 55 km) grid. But as a forcing dataset for ocean modelling, we interpolate the data onto the normal TL319 grid (see Appendix A.1 for details). The necessary variables are the downward shortwave and longwave radiative fluxes, precipitation (separated into rain and snow), 10-m wind vector, sea level pressure, and the air temperature and specific humidity at 10 m (shifted from their original 2-m height). Our preliminary evaluation indicated that the surface fields of JRA-55 must be adjusted (bias-corrected locally and modified globally to impose flux balances) similarly to the NCEP/NCAR reanalysis in the CORE dataset and the ECMWF reanalysis in the DRAKKAR forcing set (Brodeau et al., 2010) (see also Fig. 1). We adjust all variables except the sea level pressure. We also consider time-dependent adjustments to correct the abrupt shifts in the data quality of JRA-55. These shifts are introduced by changes in the observing systems. However, to provide data in near real-time, the adjustment factors for the most recent decades will be continually used for future updates.

The JRA55-do forcing dataset also includes the daily river runoff produced by operationally running a global river hydrodynamic model forced by an adjusted runoff from the land-surface component of JRA-55 (Suzuki et al., 2017). However, river runoff from Greenland and Antarctica is derived from observational climatology based on independent estimates that account for the discharge and melting of ice-sheets and ice-shelves.

The JRA55-do dataset does not satisfy all the above-listed items. Specifically, future development is required to extend the data to pre-1948, to incorporate surface ocean wave effects, and to improve atmospheric fields over regions covered by sea-ice.

In this paper we introduce the new forcing dataset, JRA55-do (based on JRA-55), designed for driving ocean–sea-ice models. As part of this presentation, we describe general features of JRA55-do, the adjustment methods used in its construction, and overall assessments of its quality.

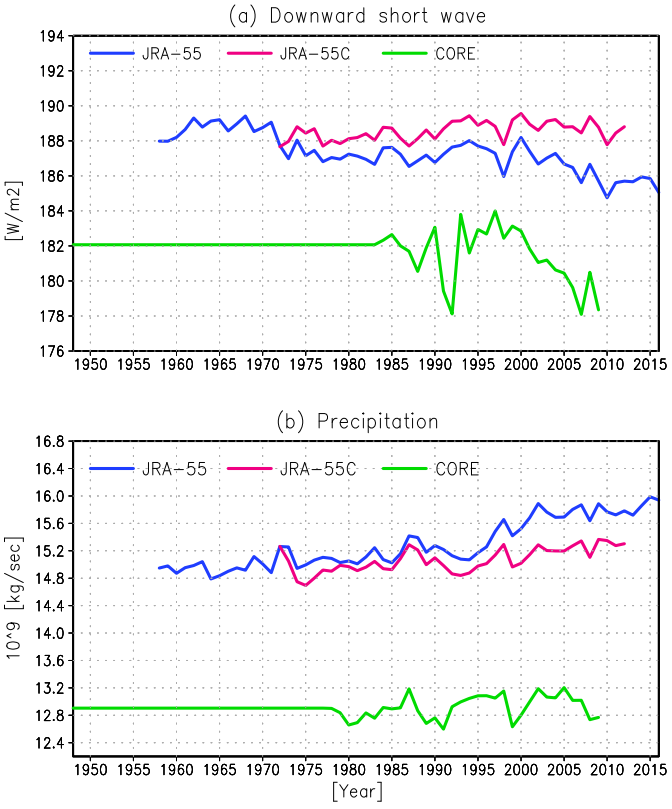

Fig. 1. Comparison of annual mean data over the ocean in the JRA-55 (blue), JRA-55C (magenta), and CORE (green) datasets; (a) global ocean averaged downward shortwave radiation ($\mathrm{W\,m^{-2}}$) and (b) global ocean-integrated precipitation ($\mathrm{kg\,s^{-1}}$). (For interpretation of the references to colour in this figure legend, the reader is referred to the web version of this article.)

Because (at least in the foreseeable future) JRA55-do is intended mainly for global modelling in the CORE/OMIP framework, our assessments focus on large-scale features and global balances of the surface fluxes. In a companion paper (Taboada et al., 2018), we assess the wind patterns regionally including the eastern-boundary upwelling zones. In Section 2 of the present paper, we define the variables needed for forcing ocean–sea-ice models. Section 3 explains the method and rationale for adjusting the surface-atmospheric variables of JRA-55. Section 4 details the river runoff fields, and Section 5 discusses the final adjustment procedure for global flux balance. The large-scale features of the dataset are evaluated in Section 6. Finally, in Section 7 we present a summary and concluding remarks.

We offer a suite of appendices that present the many technical details relevant for JRA55-do. Appendix A explains the processing of the raw JRA-55 data. Appendix B presents formulas to compute properties of moist air that we advocate as a replacement to those used by the current CORE/OMIP framework. Appendix C gives details of the dataset. Appendix D introduces the sea-surface temperature dataset (COBESST; Ishii et al., 2005) which was used extensively in JRA-55 and the present study. Appendix E explains the evaluation and adjustment of the surface radiative fluxes of CERES-EBAF-Surface_Ed2.8 (Kato et al., 2013), which we adopted as the reference data to adjust the radiative fluxes of JRA-55. Appendix F presents a detailed comparison of surface meteorological variables with buoy observations. Appendix G shows an atlas of annual mean surface fluxes of JRA55-do and their comparison with the CORE dataset.

2. Variables necessary for forcing ocean–sea-ice models

In this section we briefly review the sea-surface flux calculations and then derive the necessary surface-atmospheric variables for forcing the ocean–sea-ice system. Although given in Section 2 of Large and Yeager (2009), we provide the expressions here in support of the adjustment methods encountered later in this paper.

The ocean is forced at the sea-surface by the fluxes of momentum $\vec{\tau}$, heat Q, and freshwater F. The ocean surface is covered by either atmosphere or sea-ice and the fluxes are computed separately by different formulas. When computing the surface flux in an ocean grid cell, we assume that a normalised fraction f_o of the cell is exposed to the atmosphere. The momentum, heat, and freshwater fluxes are respectively expressed as follows:

$$\vec{\tau} = f_o \vec{\tau}_{AO} + (1 - f_o)\vec{\tau}_{IO}, \tag{1}$$

$$Q = f_o Q_{AO} + (1 - f_o) Q_{IO} + Q_R, \tag{2}$$

$$F = f_o F_{AO} + (1 - f_o) F_{IO} + R, \tag{3}$$

where the subscripts AO and IO denote the fluxes at the air - ocean and ice - ocean interfaces, respectively. In Eqs. (2) and (3), R denotes the total continental runoff. The river runoff is treated as part of the surface freshwater flux in Eq. (3) and Q_R represents the heat transport due to runoff.

At present, it is difficult to compute the ice - ocean fluxes from observational data. Moreover, the computations are strongly affected by the imperfect representation of the thermodynamic and dynamic processes in sea-ice models. Therefore, we do not try to adjust local ice - ocean fluxes in this study. However, we use their global ocean averaged values for the purpose of closing the global ocean averaged heat and freshwater flux budget in a multi-decadal time scale (see Section 3.2.3). We use approximate global mean ice - ocean fluxes derived from a global ocean–sea-ice model simulation. In a global ocean–sea-ice simulation under the CORE dataset conducted at the Meteorological Research Institute (MRI) (e.g., Tsujino et al., 2011), the annual mean global ocean averaged cooling due to $(1 - f_o)Q_{IO}$ is roughly $1.4\,\mathrm{W m^{-2}}$. For the freshwater flux, we close the budget of the ocean–sea-ice system. Therefore, instead of F_{IO}, we consider the freshwater flux due to sublimation (S) over the sea-ice or snow:

$$F_{ocean+ice} = f_o F_{AO} + (1 - f_o)(P + S) + R, \tag{4}$$

where P represents precipitation. Based on a global ocean–sea-ice simulation, the global ocean integrated, long-term mean sublimation is taken as $0.05 \times 10^9\,\mathrm{kg s^{-1}}$ (upward). We should revise this value in a future version when an observational estimate for this quantity becomes available. In general, a global balance of the surface momentum fluxes is not required.

The air - ocean heat and freshwater fluxes are the sums of their components:

$$Q_{AO} = Q_{SW} + Q_{LW} + Q_{LA} + Q_{SE} + Q_{P+E} \tag{5}$$

$$F_{AO} = P + E, \tag{6}$$

where the positive direction of all fluxes is downward. The shortwave radiation flux Q_{SW} is computed by

$$Q_{SW} = (1 - \alpha) Q_{DSW}, \tag{7}$$

where Q_{DSW} is the downward shortwave radiation flux and the albedo α (a function of latitude) is taken from Large and Yeager (2009).

The longwave radiation flux Q_{LW} is computed by

$$Q_{LW} = Q_{DLW} - \epsilon\sigma\theta_O^4, \tag{8}$$

where Q_{DLW} is the downward longwave radiation flux, ϵ is the emissivity (here assumed as 1.0 to account for the small fraction of Q_{DLW} that is reflected (Lind and Katsaros, 1986)), $\sigma = 5.67 \times 10^{-8}\mathrm{W m^{-2} K^{-4}}$ is the Stefan-Boltzmann constant, and θ_O is the sea-surface temperature. The latent heat flux Q_{LA} is equivalent to the evaporation E as follows:

$$E = \rho_a C_E (q_A - q_{\mathrm{sat}}(\theta_O)) |\Delta\vec{U}|, \tag{9}$$

$$Q_{LA} = \quad LE, \tag{10}$$

where ρ_a and q_A respectively denote the density and the specific humidity of air, C_E is the bulk transfer coefficient for water vapor, $q_{\mathrm{sat}}(\theta_O)$ is the saturation-specific humidity at the sea-surface temperature, and $\Delta\vec{U}$ is the surface wind relative to the sea-surface current ($\Delta\vec{U} = \vec{U}_A - \vec{U}_O$). L is the latent heat of vaporisation. The sensible heat flux Q_{SE} is computed by

$$Q_{SE} = \rho_a c_{pa} C_H (\theta_A - \theta_O)|\Delta\vec{U}|, \tag{11}$$

where c_{pa} is the specific heat of air, C_H denotes the bulk transfer coefficient of heat, and θ_A is the surface air temperature. The properties of moist air such as ρ_a, c_{pa}, L, and q_{sat}, are calculated by the formulas presented in Appendix B. We advocate using a set of formulas given by Gill (1982) for computing the properties of moist air, which is thought to be more accurate than the simple and cost-effective set of formulas used for the current CORE/OMIP framework as given by Large and Yeager (2004). Because ρ_a and q_{sat} are also a function of sea-level pressure (*SLP*), we need sea-level pressure for computing fluxes.

Precipitation occurs in the liquid (rain) or solid (snow) phase. The temperature of surface freshwater fluxes in the liquid phase is assumed to equal the local sea-surface temperature:

$$Q_{P+E} = c_{po}(P + E)\theta_O, \tag{12}$$

where $c_{po} = 3.99 \times 10^3\,\mathrm{J\,kg^{-1}\,K^{-1}}$ is the specific heat of sea water. In the above-mentioned global ocean–sea-ice simulation conducted at MRI, the global ocean averaged, long-term mean $f_o Q_{P+E} + Q_R$ was approximated as $-0.4\,\mathrm{W\,m^{-2}}$ (the negative sign implies ocean cooling). In the MRI simulation, all precipitation, evaporation, and runoff were assumed to be in the liquid phase. The cooling results since evaporation dominates in low-latitudes (removing warm water from the ocean) and precipitation dominates in high-latitudes (adding cold water to the ocean). Note that this argument only holds for ocean models that treat the surface freshwater flux explicitly. For more details on the water heat flux, readers are referred to Griffies et al. (2014) (see their Appendix A.4.).

The bulk transfer coefficients, C_E and C_H, parameterise the turbulent fluxes in terms of the surface-atmospheric state. They are usually computed along with the bulk transfer coefficient of momentum C_D, from which the surface stress is calculated as follows:

$$\vec{\tau}_{AO} = \rho_a C_D |\Delta\vec{U}|\Delta\vec{U}. \tag{13}$$

Note that in a more precise analysis, part of $\vec{\tau}_{AO}$ is received by the surface ocean wave fields and the momentum is redistributed before reaching the large-scale ocean circulation fields (e.g., Mitsuyasu 1985; Scully et al. 2016). However, to our knowledge, a global mapping of such momentum redistribution has not been attempted. Among the several propositions of bulk formulas, we adopt the bulk formulas by Large and Yeager (2009) that have been used in the suite of CORE/OMIP projects, at both the air - ocean and the air - ice interfaces. Note that the use of a set of formulas given by Gill (1982) to compute properties of moist air (Appendix B), which we recommend here, slightly deviates from the set of CORE bulk formulas.

In summary, the ocean–sea-ice models are driven by seven atmospheric variables, Q_{DSW}, Q_{DLW}, P (separated into rain and snow), θ_A, q_A, *SLP*, $\vec{U}_A$, which are sourced from the forecast phase of JRA-55, and the river runoff (R), which is produced by running a global river hydrodynamic model forced by an adjusted runoff from the land-surface component of JRA-55. These variables are adjusted to minimise biases and to achieve a globally closed heat and freshwater flux in a multi-decadal time scale. Besides these external data, we need two ocean variables; the sea surface temperature (θ_O) and surface current vector ($\vec{U}_O$). In most ocean–sea-ice models, the values of these variables at the first vertical level are used as those of the sea-surface, although the first level in ocean models typically represents an average over a few meters rather than the sea-surface itself. Necessary variables are summarised in Tables 1 and 2. We provide full details of the dataset in Appendix C.

3. Adjusting the surface-atmospheric variables of JRA-55

This section describes how we have adjusted the seven surface atmospheric variables of JRA-55 that are necessary, as explained in the previous section, for computing surface fluxes. We first describe the general adjustment strategy in Sections 3.1 and 3.2, and then give more details on the adjustment processes for individual variables in Sections 3.3–3.6.

3.1. JRA-55 and its subsets

JRA-55 (Kobayashi et al., 2015; Harada et al., 2016) is the first comprehensive reanalysis covering the last half-century since the European Center for Medium-Range Weather Forecast's 45-year Reanalysis (ERA-40; Uppala et al., 2005). Moreover, the long-term reanalysis was performed by a four-dimensional variational method, which has not been attempted before. The coverage begins from 1958 and is planned to continue until approximately 2022 as part of the JMA operational climate services. The JRA-55 system is based on JMA's operational global data assimilation-forecast system as of December 2009 (JMA,

Table 1
Description of the JRA55-do dataset version 1 (the latest version is 1.3). The main variables listed here as well as supplementary data listed on Table 2 can be obtained at https://esgf-node.llnl.gov/search/input4mips/. Data files are stored in netCDF format. Each file contains the annual 3-hourly and daily time-series of a single variable on the TL319 and 0.25° × 0.25° grid, for atmospheric variables and river runoff, respectively. Time-series are constructed for each year, including leap years. The first column describes the name assigned to each variable in the netCDF file. These names are taken from Climate Model Output Rewriter (CMOR). The fifth column gives the time of the first datum in each file. The sixth column states whether the given field is an averaged property or a snapshot. Note that rain-plus-snow equals the total precipitation (P).

Variable name	field (symbol used in Section 2)	Units	Horizontal grid	First data represents	Frequency (average or snapshot)
tas	10 m air temperature (θ_A)	K	TL319 (0.5625°)	0:00 1 Jan	3-h, snapshot
huss	10 m specific humidity (q_A)	$\mathrm{kg\,kg^{-1}}$	TL319 (0.5625°)	0:00 1 Jan	3-h, snapshot
uas	10 m eastward wind ($\vec{U}_A$)	$\mathrm{m\,s^{-1}}$	TL319 (0.5625°)	0:00 1 Jan	3-h, snapshot
vas	10 m northward wind ($\vec{U}_A$)	$\mathrm{m\,s^{-1}}$	TL319 (0.5625°)	0:00 1 Jan	3-h, snapshot
psl	Sea level pressure (*SLP*)	Pa	TL319 (0.5625°)	0:00 1 Jan	3-h, snapshot
rsds	Downward shortwave (Q_{DSW})	$\mathrm{W\,m^{-2}}$	TL319 (0.5625°)	1:30 1 Jan	3-h, mean
rlds	Downward longwave (Q_{DLW})	$\mathrm{W\,m^{-2}}$	TL319 (0.5625°)	1:30 1 Jan	3-h, mean
prra	Rainfall flux (P)	$\mathrm{kg\,m^{-2}\,s^{-1}}$	TL319 (0.5625°)	1:30 1 Jan	3-h, mean
prsn	Snowfall flux (P)	$\mathrm{kg\,m^{-2}\,s^{-1}}$	TL319 (0.5625°)	1:30 1 Jan	3-h, mean
friver	Total river runoff[a] (R)	$\mathrm{kg\,m^{-2}\,s^{-1}}$	0.25° × 0.25°	1 Jan	Day, mean

[a] Data of river discharge to the ocean (Suzuki et al., 2017) and runoff from Greenland (Bamber et al., 2012) and Antarctica (Depoorter et al., 2013) are merged.

Table 2
Description of the supplementary data of JRA55-do. The first column describes the name assigned to each variable in the netCDF file. These names are taken from CMOR.

Variable name	Field (symbol used in Section 2)	Units	Horizontal grid	First data represents	Frequency (average or snapshot)
ts	brightness temperature from JRA-55 (θ_O or θ_I)	K	TL319 (0.5625°)	0:00 1 Jan	3-hour, snapshot
siconca	sea-ice distribution from JRA-55 (0 or 1) ($1 - f_o$)	%	TL319 (0.5625°)	0:00 1 Jan	3-hour, snapshot
tos	sea-surface temperature from COBESST (Ishii et al., 2005) (θ_O)	°C	1° × 1°	1 Jan	day, mean
siconc	sea-ice distribution from COBESST (Ishii et al., 2005) ($1 - f_o$)	%	1° × 1°	1 Jan	day, mean
sos	sea-surface salinity from the World Ocean Atlas 2013 v2 (Zweng et al., 2013; Boyer et al., 2015)	0.001	0.25° × 0.25°	–	month, climatology
uo	sea water X velocity from GlobCurrent (Rio et al., 2014) ($\vec{U}_O$)	$m\,s^{-1}$	TL319 (0.5625°)	–	year, climatology
vo	sea water Y velocity from GlobCurrent (Rio et al., 2014) ($\vec{U}_O$)	$m\,s^{-1}$	TL319 (0.5625°)	–	year, climatology
areacello	grid-cell area for atmospheric data	m^2	TL319 (0.5625°)	–	fixed
sftof	land-sea mask for atmospheric data (1 for sea, 0 for land)	1	TL319 (0.5625°)	–	fixed
licalvf	solid water runoff from Antarctica represented as calving flux from Depoorter et al. (2013)	$kg\,m^{-2}\,s^{-1}$	0.25° × 0.25°	–	year, climatology
areacellg	grid-cell area for river and solid water runoff data	m^2	0.25° × 0.25°	–	fixed

Table 3
List of acronyms of JRA-55 subproducts.

Acronym	Description
JRA-55	The generic name that refers to the JRA-55 project and its product
JRA-55anl	JRA-55 screen-level (surface) analysis using two-dimensional optimal interpolation
JRA-55C	JRA-55 subproduct assimilating Conventional observations only
JRA55-raw	Surface atmospheric fields derived from the forecast phase of JRA-55 (no adjustments applied)
JRA55-adj	Surface atmospheric fields after applying the adjustments on JRA55-raw described in Section 3
JRA55-do	The final product obtained after the global-balance adjustment of JRA55-adj described in Section 5

2007, 2013). The assimilation window of the base-system (6 hours) is unchanged for JRA-55. To derive the atmospheric fields for driving the ocean–sea-ice models, we obtained 3-hourly outputs from the forecast phase (the 3rd and 6th hours after initialisation) rather than the initial (analysis) state. Meteorological variables such as temperature, humidity, wind vectors, and sea level pressure were obtained from instantaneous data, while fluxes such as radiation and precipitation were determined from three-hour mean data. Here, fluxes should be averaged quantities for any budget analyses using this dataset to be done consistently.

Separately from the main atmospheric four-dimensional variational analysis, the JRA-55 system also performs a two-dimensional optimal interpolation analysis for the surface temperature and specific humidity at 2 m height, and the surface wind vector at 10 m height (Kobayashi et al., 2015). Hereafter, this analysis is called JRA-55anl. This analysis takes the forecast fields of the four-dimensional analysis of JRA-55 as the first guess. The same correlation scales as the four-dimensional analysis are used for the error of the first guess. Thus, the analysis fields of JRA-55anl are not significantly smoothed relative to the four-dimensional analysis fields of JRA-55. However, the analysis fields of JRA-55anl do not constitute the initial state for the forecast phase of the four-dimensional analysis. For developing JRA55-do, this separate surface analysis was extensively used as a reference dataset for adjusting the surface marine meteorological variables, as explained in the following sections.

A subset of JRA-55, JRA-55 Conventional (JRA-55C; Kobayashi et al., 2014), uses the JRA-55 data-assimilation system but excludes satellite observations. As a result, it assimilates only the conventional surface and upper air observations. The JRA-55C project aims to improve the inhomogeneity of long-term datasets by removing the historical changes in satellite observing systems. For this purpose, JRA-55C was branched off from JRA-55 in November of 1972, just before a vertical temperature profile radiometer (VTPR) was installed in 1973. From the JRA-55C data, we can assess the biases in the pre-satellite (pre-1973) period assuming that these biases have persisted into the recent period, where they can be quantified by referencing to satellite data.

For reference, the acronyms containing JRA-55 or JRA55 are listed in Table 3.

3.2. Adjustment strategy

3.2.1. Main adjustment

Fields derived from the forecast phase of JRA-55 (hereafter referred to as JRA55-raw) were adjusted to match their long-term means with those of reference fields. Specifically, the long-term means of the JRA55-raw fields and reference fields were calculated for an overlapping period, and compared to determine adjustment factors. The adjustment factors are spatially varying, and no smoothness constraints were applied to the factors. We used a multiplicative factor or offset depending on the nature of the variable. Offset factors were used for variables that can be positive or negative such as air temperature and wind direction. However, offset factors are awkward for strictly positive variables because the treatment of values around zero may not be uniquely determined. For example, simply applying a positive offset to precipitation will result in a situation that there is always a small amount of precipitation. An offset is also awkward for downwelling shortwave radiation which is generally zero during the night. Thus, to simplify the processing, we used multiplicative factors for strictly positive variables in principle. However, it should be noted that we may modify the variance in an unconstrained manner by using multiplicative factors to adjust the long-term mean. Actually, based on the assessments on the older versions, we used an offset to adjust wind speed, which is a strictly positive variable, in the latest version so as to retain the variance contained in the original JRA-55 wind fields (see also Appendix C.3.1). In an advanced adjustment method, we could constrain both mean and variance using both multiplicative factor and offset. However, adjusting the variance would require a large amount of work. First, the time scale of the variance to be adjusted, such as stochastic, seasonal, or interannual, would need to be chosen. Then, it would be necessary to reconstruct a time-series for both JRA55-raw and the reference dataset to constrain the variance for the chosen time scale. The choice of the time scale might be limited by the availability of the reference data. It would also be necessary to confirm that the adjustment on the variance for a particular time scale would do no harm to variability in other time scales. This approach might be taken for a future version, after consideration of results from ocean model simulations that use JRA55-do. For this study, we focussed on adjusting the

Table 4
Summary of the adjustment factors applied to the original surface fields in JRA-55 (JRA55-raw). The last column indicates whether the variable was subsequently adjusted by a spatially and temporally homogeneous factor to formally close the long-term (1988–2007) heat and freshwater flux budgets.

Variable	Reference data	Availability of reference data	Time dependency	Multiplicative or offset	Additional global adjustment
Downward shortwave	CERES[a]	Mar 2000–Feb 2015	Monthly	Multiplicative	Yes
Downward longwave	CERES[a]	Mar 2000–Feb 2015	Monthly	Multiplicative	Yes
Precipitation	CORE	1979–2009	Monthly	Multiplicative	Yes
	GPCP-v2.3[b]	1979–2015	Monthly	Multiplicative	
Air temperature	ensemble[c]	1980–2014	Monthly	Offset	No
(on sea-ice)	JRA-55anl-NPOLES[d]	1979–1998	Monthly	Offset	
Specific humidity	ensemble[c]	1980–2014	Monthly	Multiplicative	No
Wind speed	QuikSCAT[e]	Nov 1999–Oct 2009	Annual	Offset	No
	SSM/I[f]	Jan 1988–Dec 2015	Annual	Offset	
Wind direction	QuikSCAT[7]	Nov 1999–Oct 2009	Annual	Offset	No

[a] CERES EBAF-Surface_Ed2.8 (Kato et al., 2013), adjusted relative to buoy observations. See Appendix E.
[b] Global Precipitation Climatology Project version 2.3 (Adler et al., 2003).
[c] Ensemble mean of seven reanalysis products: JRA-55 screen-level analysis (JRA-55anl), ERA-interim (Dee et al., 2011), NCEP-CFSR (Saha et al., 2010), MERRA2 (Gelaro et al., 2017), NCEP-R1 (Kalnay et al. 1996; Kistler et al. 2001), NCEP-R2 (Kanamitsu et al., 2002), and 20CRv2 (Compo et al., 2011).
[d] JRA-55anl adjusted relative to International Arctic Buoy Programme (IABP) / Polar Exchange at the Sea Surface (POLES) Arctic surface air temperature data (Rigor et al., 2000) over sea-ice in the arctic region.
[e] Remote Sensing Systems QuikSCAT Ku-2011 Daily Ocean Vector Winds on 0.25 deg grid version 4 (Ricciardulli et al. 2011; Ricciardulli and Wentz 2015), gaps filled with JRA-55anl.
[f] SSM/I based wind speed product version 7 (Wentz, 2013), gaps filled with JRA-55anl.

mean state using a single factor, either multiplicative or offsetting.

Table 4 summarises the approaches for finding the adjustment factors. To ensure that we can update the JRA55-do dataset in near real-time, all variables including the radiation and precipitation are based on JRA55-raw. Unlike Large and Yeager (2009), who sourced the radiation and precipitation from independent observation-based data, we adjust the radiation and precipitation data in a reanalysis dataset (JRA55-raw). The adjustments were performed on reduced TL319 grid points where the JRA-55 fields were originally provided. The reference fields for most variables have been updated relative to those used for the CORE dataset (Large and Yeager, 2009). The rationale for this change will be presented in later subsections devoted to the adjustment method of each variable. After making the main adjustments, we zonally interpolated the fields on the reduced TL319 grid points onto the normal TL319 grid (see also Appendix A.1). We then made additional adjustments as explained in the next subsection.

The adjusted atmospheric fields are designated as JRA55-adj to distinguish them from the final product JRA55-do. JRA55-do was obtained after the global-balance adjustment of JRA55-adj (see Section 5).

Note that we did not adjust the sea level pressure because there is not good data to be used as a reference field. Therefore, when applying the dataset to (for example) storm surge modelling, the user should be aware of the possible inconsistencies between the surface pressure and the adjusted wind fields.

The atmospheric fields in JRA-55 were sometimes shifted by changes in the observation systems (Kobayashi et al., 2015). To accommodate these shifts, we divided the dataset into several phases and separately adjusted each phase. Fig. 12 of Kobayashi et al. (2015) shows the 2-day forecast scores at the geopotential height of 500 hPa. The authors stated that:

> "*The forecast scores of JRA-55 show relatively large variations that correspond to the introduction of VTPR (Vertical Temperature Profile Radiometer) in 1973, the advent of satellite observing system in the late 1970s, ATOVS (Advanced Television and infrared observation satellite Operational Vertical Sounder) in 1998, and GNSS-RO (Global Navigation Satellite System-Radio Occultation) in 2006…*"

The forecast score markedly improved in 1998, indicating improvement in the overall quality of reanalysis at that time. Discernible transitions also appeared from the late 1970s through the early 1980s, especially in the Southern Hemisphere. However, we note that partitioning at the late 1970s will leave the period of 1973–1978 very difficult to correct/adjust owing to the shortness of the period and the limited availability of observations. On the other hand, the year 1973 marks the inclusion of VTPR and the separation of JRA-55C from JRA-55.

Fig. 1 compares the time series of the downward shortwave radiation and precipitation in the JRA-55, JRA-55C, and CORE datasets. From 1973, the shortwave radiation was clearly lower in JRA-55 than JRA-55C. After 1998, the precipitation was clearly increased, which was not seen in the CORE dataset, and the shortwave radiation further lowered, in JRA-55 relative to JRA-55C. In JRA-55, AMSU-A (included in Aug 1998) corrected the warm bias in the upper troposphere over the ocean, whereas AMSU-B (included in Oct 2000) corrected the dry bias in the upper and middle troposphere over the ocean (see Figs. 9 and 10 of Kobayashi et al. (2015)). Both corrections increased the overall precipitation over the ocean and possibly influenced the shortwave radiation. The precipitation increase occurred mainly in the tropical regions (Kobayashi et al., 2015). It should also be noted that from May 1997, JRA-55 included the scatterometer winds (ERS from May 1997 to Jan 2001, QuikSCAT from Jul 1999 to Nov 2009, and ASCAT from Jan 2008). Thus, the 1997–98 period is also a suitable transition point for wind-field adjustment. We also note that in Fig. 1 the long-term mean global ocean averaged downward shortwave radiation and precipitation were biased high relative to those of the CORE dataset, which warrants adjustment on JRA-55 fluxes.

Based on these assessments, we divided the dataset period of JRA-55 into three phases 1958–1972 (phase-I); 1973–1997 (phase-II); and 1998–present (phase-III). We then applied different adjustment factors in each phase.

During Phase-I (1958–1972), only the conventional observations were available. Because reference fields for adjusting the reanalysis fields could not be constructed from these insufficient data, we utilised JRA-55C since it only uses conventional observations. Assuming that the biases in the pre-satellite (pre-1973) period have persisted into the recent period in JRA-55C, we assessed the general biases for Phase-I by using the JRA-55C data in recent years, when satellite data are available to construct reference fields. A regime shift in the JRA-55C data occurred around 1997 in the Equatorial Indian Ocean. Specifically, the intensification of westerly winds in the Maritime Continent region and over the Equatorial Indian Ocean, and the increase of divergence in the tropical region of the African Continent occurred after 1997 (results not shown). Such regime shifts were not found in observations or other reanalysis products, and were considered to be an erroneous response

of the atmosphere–land-surface system in JRA-55C (details of which have not been clarified yet). Consequently, the general biases in the 1958–1972 period were evaluated using pre-1997 JRA-55C data. For the assessment of biases, an appropriate period was selected for each variable from 1973–1996 based on the availability of the reference data. See later sections for details. When evaluating the biases in phases II and III, we excluded the large El Niño years (1997 and 1998) from the climatology computation.

The adjustment factors changed from 01 Oct to 30 Nov in 1972 (between phases I and II) and from 01 Jan 1997 to 31 Dec 1998 (between phases II and III). The adjustment factors in the transition periods were linearly interpolated (in time) between the factors of the two adjacent phases.

3.2.2. Additional adjustments

After the main adjustment, the systematic biases introduced by native settings of JRA-55 were corrected by the following secondary adjustments, with motivation and details presented later in this section.

- The temperature and specific humidity were smoothed around the marginal sea-ice zones.
- The extremely low air temperature around Antarctica was cut-off by introducing a floor function (see Section 3.3.4 for details).
- During the pre-satellite period (1958–1978), the monthly anomaly in CORE relative to JRA55-adj was added to the temperature and specific humidity in high-latitude regions.
- The precipitation over the Mediterranean Sea was reduced during the pre-satellite period (1958–1978).

The first, second, and third corrections compensate for the lack of partial sea-ice cover in the grid cells of the atmospheric model used by JRA-55. The third correction is because NCEP-R1, on which the air temperature and specific humidity of the CORE dataset are based, shows plausible sea-ice distributions in comparison with JRA-55 in the pre-satellite period as shown later. The fourth correction is to reduce the excessive precipitation around the European Continent during the 1960s and 1970s due to processing errors on some radiosonde data used in JRA-55.

3.2.3. Closing the budgets

The adjusted atmospheric dataset (JRA55-adj) was tested to see whether it could satisfy well-recognised constraints (as discussed below) on the global surface-heat and freshwater flux budgets when a realistic surface condition was applied (Section 5). When calculating the global ocean surface flux budget (excluding the sea-ice region), we applied COBESST (Ishii et al., 2005) as the lower boundary condition (sea-surface temperature and sea-ice distribution). Appendix D briefly introduces COBESST. The latitude-dependent albedo and the bulk formulae (including the saturation of the transfer coefficients in the high-wind regime) were taken from Large and Yeager (2009). The air properties were computed as described in Appendix B.

COBESST is analysed on a $1^\circ \times 1^\circ$ grid and its SST structure is smooth. Although a high-resolution SST product can give more detailed and presumably more accurate structure of fluxes, a low-resolution product (COBESST) has been selected for this study because it is anticipated that the majority of ocean-climate models that participate in CMIP6-OMIP will adopt a nominal 1-degree horizontal resolution. A model integration for about 300 years is required for the physical OMIP. In the biogeochemical OMIP, many tracers are added to the model and much longer integrations will be required for the spin-up. Fulfilling these requirements with a mesoscale eddy permitting model is too computationally challenging for many modelling centres. The SST structure of low-resolution products is what a nominal 1-degree ocean-climate model ideally reproduces. Thus, as a forcing dataset to be used in the framework of OMIP, JRA55-do was evaluated and adjusted in terms of the global ocean averaged surface flux budget by using a low-resolution SST product (COBESST). A use of higher resolution SST products should be considered in the future evaluation and development efforts as the computational resources to perform the OMIP experiments with mesoscale eddy permitting models become available for the majority of modelling centres.

As a constraint on the global surface-heat and freshwater flux budgets, we continue to adopt the constraint used by Large and Yeager (2009) that the long-term mean globally averaged heat flux and globally integrated freshwater flux into the ocean–sea-ice system are both nearly zero or slightly positive ($\sim 0 - 1\,\mathrm{W\,m^{-2}}$ for heat and $\sim 1 \times 10^7\,\mathrm{kg\,s^{-1}}$ for freshwater fluxes). Levitus et al. (2012) estimated that the global ocean heat uptake was $0.39\mathrm{W m^{-2}}$ for 1955–2010 and Loeb et al. (2012) gave $0.50 \pm 0.43\,\mathrm{W\,m^{-2}}$ for 2001–2010. These figures are about two orders of magnitude smaller than the major components of the surface heat budget, such as shortwave radiation, longwave radiation, latent heat, and sensible heat fluxes ($O(10) - O(10^2)\mathrm{W\,m^{-2}}$). Church et al. (2011) estimated that the global ocean mass change was $0.98\mathrm{mm\,y^{-1}}$ for 1972–2008, largely contributed by the melting of glaciers and ice caps. This corresponds to a global ocean-integrated mass flux of $1.1 \times 10^7\,\mathrm{kg\,s^{-1}}$, which is, again, about two orders of magnitude smaller than the major components of the surface freshwater budget, such as evaporation, precipitation, and river runoff ($O(10^9) - O(10^{10})\,\mathrm{kg\,s^{-1}}$). (Here, global oceanic area is taken as $3.654 \times 10^{14}\,\mathrm{m^2}$.)

It is desirable that the global flux budgets are nearly closed, and comparable to the above estimates on a multi-decadal time scale, after the main and additional adjustments on local atmospheric variables and fluxes explained in the previous subsections have been applied. Unfortunately, this closure is not necessarily the case as will be shown in Section 5. An absence of closure implies that biases still remain in all flux components, and that they may also vary regionally. To assess and correct those regional biases, a sufficient amount of local observational data would be necessary. Because such data are unavailable, we do not attempt further local adjustment but instead attempt to exactly close the global surface flux budget. Specifically, we applied a globally uniform, time-invariant adjustment factor on downwelling radiations and precipitation.

The adjustment factor for downwelling radiations was determined by requiring exact closure ($\sim 0\mathrm{W m^{-2}}$) on a global ocean heat budget for a multi-decadal time-period (1988–2007) in the satellite era. The adjustment factor is then applied for the entire dataset period. Details will be explained in Section 5. The precipitation (P) was similarly readjusted. After adjustment, the global freshwater input to the ocean–sea-ice system formally balances with the evaporation (E), river runoff (R) and sublimation over the sea-ice (S), i.e., $\mathcal{E} + \mathcal{S} + \mathcal{P} + \mathcal{R} \sim 0$ during the same multi-decadal time-period as used for the heat flux. Here, the use of $\mathcal{E}$ instead of E implies an integration over a global ocean as well as an averaging over a multi-decadal time scale. In JRA55-do, the runoff is imported from other sources. Provided that the adjustment is minor, any river runoff dataset that is optionally added to JRA55-do will be adjusted to match its long-term (1988–2007) mean with that of the first version (1.26 Sv, where $1\,\mathrm{Sv} = 10^6\,\mathrm{m^3\,s^{-1}}$; see Section 4).

The final adjusted fields comprise the JRA55-do dataset. Note that the long-term closure adopted here will still allow for the study of interannual variability in the ocean–sea-ice system. However, it may preclude investigation of long-term trends, although a trend may be imposed by a user by slightly modifying the globally uniform factors applied to the downward fluxes. On the other hand, the exact closure may be suited for simulations run for multiple cycles of the nearly 60-year forcing in the OMIP experiments (Griffies et al., 2016), because a long-term trend will not be imposed *a priori* on the simulations.

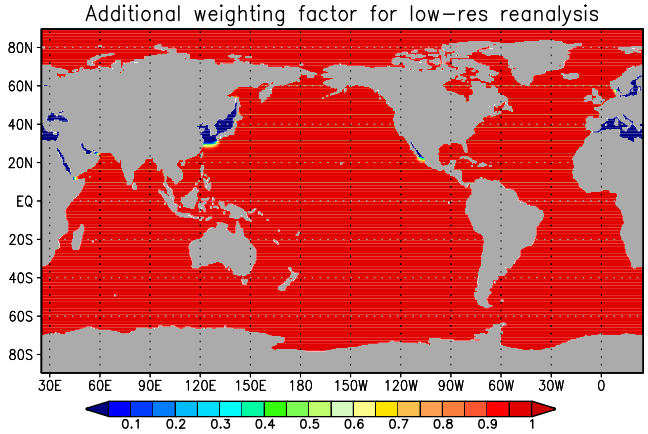

Fig. 2. Horizontal distribution of additional weights applied to low-resolution reanalyses (NCAR-R1, NCAR-R2, 20CRv2) for computing an ensemble mean of seven reanalysis products.

3.3. Temperature and specific humidity

3.3.1. Reference dataset

A reliable long-term dataset for adjusting the surface air temperature and specific humidity with consistently high data quality could not be found. Consequently, we computed the reference values for these variables from reanalysis data using an ensemble-mean approach. For this purpose, we selected seven atmospheric reanalysis products: NCEP-R1, NCEP-R2, 20CRv2, ERA-interim, MERRA2, NCEP-CFSR, and JRA-55anl. Data were first mapped onto the reduced TL319 grid of JRA-55 before the ensemble mean was computed. When computing the ensemble mean, we weighted the modern, high-resolution reanalysis products (ERA-interim, MERRA2, NCEP-CFSR, and JRA-55anl) higher than the old, low-resolution reanalysis products (NCEP-R1, NCEP-R2, and 20CRv2). The weighting factors for the modern and older products were 1.0 and 0.5, respectively. At each grid point, the contributions from the outliers (the minimum (1st) and the maximum (7th) members) were reduced to half the default weights. This approach is designed to avoid isolated large or small adjustment factors that may appear around buoys (e.g., TAO arrays in the Equatorial Pacific Ocean) when considering individual reanalysis products, as reported by Josey et al. (2014). Furthermore, the contributions from the old, low-resolution reanalysis products are excluded from the ensemble mean in semi-enclosed seas and narrow bays by applying an additional weight shown in Fig. 2. The additional weight is first set to zero for the Japan, Yellow, East China, Mediterranean, Baltic, Black, Caspian, and Red Seas, Persian Gulf, and California Bay, and unity in other regions. Then, 50 passes of a 5-point smoothing filter is applied to moderate the transition from zero to unity. Because the atmospheric fields over the ocean in those regions are represented by only a few grid points in the low-resolution products, we decided that they do not have sufficient accuracy to be used as a reference for adjusting higher resolution reanalysis products.

Surface air temperature over sea-ice can differ widely between the different reanalysis products (e.g., Lindsay et al., 2014), and so the ensemble mean air temperature is a dubious reference for data above sea-ice. Therefore, data over ice-covered regions is referenced to the JRA-55anl data. Because JRA-55anl uses the JRA-55 forecast as a first guess, we can expect modest differences between them (that is, adjustment factors will be small relative to other possible reference datasets). Before JRA-55anl is applied as a reference over sea-ice, the surface air temperatures in the Arctic region of JRA-55anl were adjusted with respect to the International Arctic Buoy Programme (IABP) / Polar Exchange at the Sea Surface (POLES) (IABP-NPOLES; Rigor et al., 2000). Specifically, the monthly climatological difference between JRA-55anl and IABP/NPOLES for the period 1979–1998 (which is the period covered by IABP/NPOLES), were used to adjust JRA-55anl for the entire dataset period (see also footnotes of Table 5). The general effect of the adjustment was to lower the air temperature of JRA-55anl in the Arctic Ocean. In the Southern Hemisphere, JRA-55anl was used as a reference field over sea-ice without modification.

Table 5
Summary of the computation of adjustment factors applied to air temperature and specific humidity in the three phases.

Variable		Phase-I (1958–72)	Phase-II (1973–97)	Phase-III (1998–present)
2 m air temperature over ocean	Reference	ensemble	ensemble	ensemble
	Raw data	JRA-55C	JRA-55	JRA-55
	Period	1980–1996	1980–1996	1999–2014
2 m air temperature over sea-ice	Reference	JRA-55anl-NPOLES[a]	JRA-55anl-NPOLES[a]	JRA-55anl-NPOLES[a]
	Raw data	JRA-55C	JRA-55	JRA-55
	Period	1980–1996	1980–1996	1999–2014
2 m specific humidity	Reference	ensemble	ensemble	ensemble
	Raw data	JRA-55C[b]	JRA-55[b]	JRA-55[b]
	Period	1980–1996	1980–1996	1999–2014

[a] JRA-55anl, whose air temperature over sea-ice in the Arctic region is adjusted relative to IABP-NPOLES. Climatological monthly offsetting factors are determined based on the comparison during the 1979–1998 period and applied for the entire period.

[b] To keep the relative humidity of the original field unchanged, the original specific humidity has been modified along with air temperature adjustment.

3.3.2. Adjustment of air temperature

Table 5 summarises the adjustment method. The JRA-55 surface air temperature was adjusted by the linear interpolation in time of monthly offsetting factors obtained by comparing the monthly climatology of JRA-55 with the reference data (the ensemble mean over the sea water and JRA-55anl adjusted relative to IABP-NPOLES over the sea-ice; see above). The base time periods used for computing climatologies were 1980–1996 (JRA-55C), 1980–1996, and 1999–2014, respectively, for the three phases. Fig. 3 shows the annual means of the offsetting factors applied in the three phases. The offsetting factors for the three phases are qualitatively similar, although there are some discrepancies among them in the Indian Ocean, the northern North Pacific, and around Antarctica. They are generally positive over open water and negative over sea-ice, implying that the surface air temperature of JRA-55 has a cold bias over open water and a warm bias over sea-ice relative to the reference datasets.

3.3.3. Adjustment of specific humidity

During the temperature adjustment, the relative humidity of the original field is unchanged, so the specific humidity should be modified accordingly. Given a relative humidity (γ) and a saturation-specific humidity (q_{s1}) for the adjusted temperature, the specific humidity (q_1) after the temperature adjustment is given by

$$q_1 = \frac{q_{s1}\gamma}{1 - q_{s1}(1-\gamma)}. \tag{14}$$

The computation of the air properties is detailed in Appendix B.

Table 5 summarises the adjustment method. In each phase, the multiplicative factor for the specific humidity is determined by comparing the monthly climatology obtained from the ensemble mean with the recalculated specific humidity. For computing the ensemble mean, the same regional weighting was used as for surface air temperature. The climatology obtained from the ensemble mean was used to adjust the specific humidity over sea-ice since the specific humidity over sea-

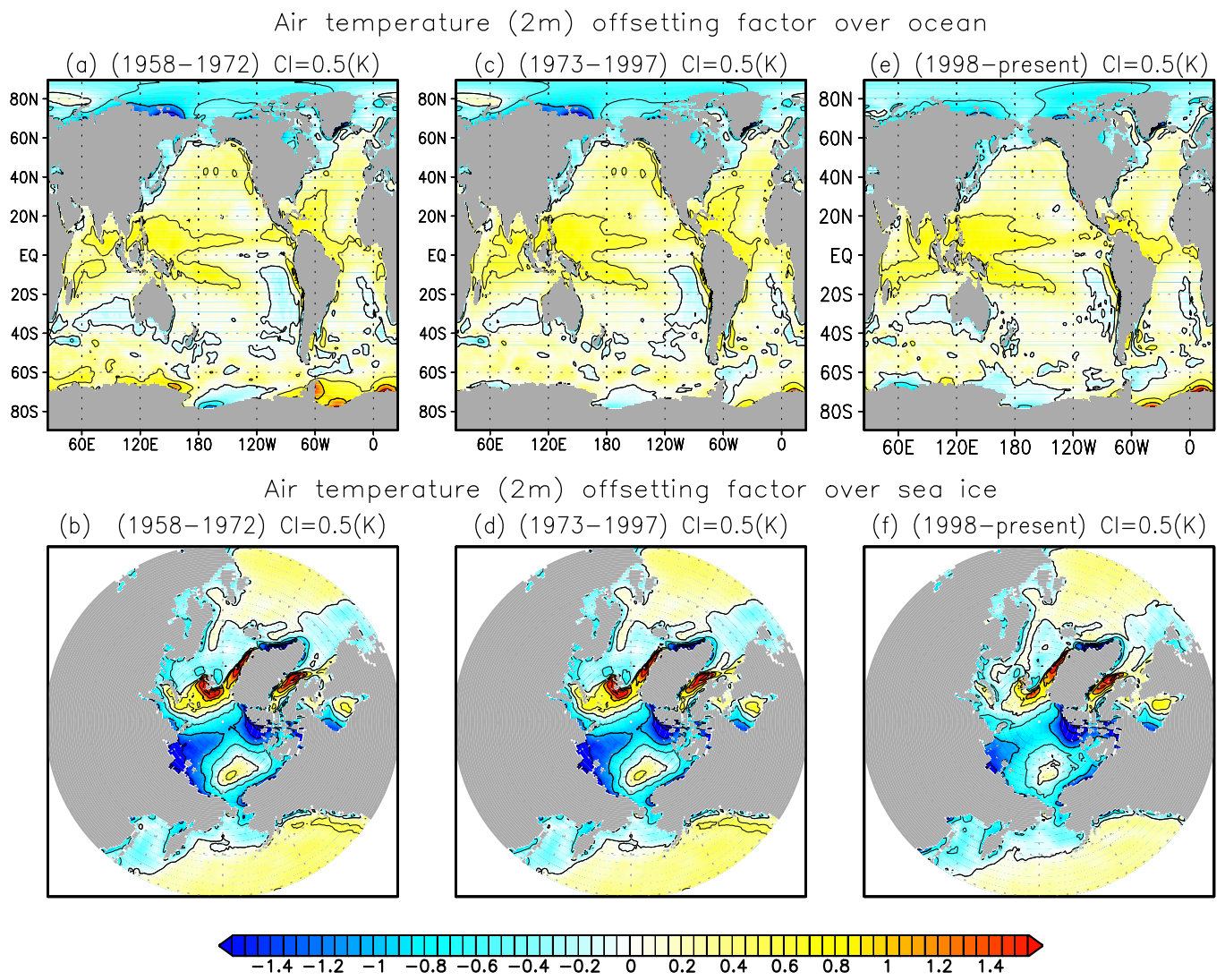

Fig. 3. (*Upper panels*) Global and (*lower panels*) northern high-latitude distributions of the annual mean offsetting factors for the surface air temperature in JRA-55 (Units in K). (a, b) phase-I (1958–72), (c, d) phase-II (1973–1997), and (e, f) phase-III (1998–present). The base time periods used for computing climatologies are 1980–1996 (JRA-55C), 1980–1996, and 1999–2014, respectively, for the three phases.

ice did not differ widely between reanalysis products (they were very low). The same base time periods as air temperature were used for computing climatologies. Fig. 4 compares the multiplicative factors for the three phases. Again, the factors are qualitatively similar for the different phases. In general, the adjustment reduces the specific humidity, implying a moist bias in the JRA-55 data. A moist bias was also reported by Kobayashi et al. (2015). The reduction is especially strong (~ 10%) in the high precipitation region in the Tropics and the stronger reduction is required for phase II than other phases.

3.3.4. Additional adjustments

To correct errors introduced by various aspects of the JRA-55 configuration (detailed below), we further adjusted the air temperature and specific humidity as follows. We explain these adjustments in the order of their implementation. Note that because the temperature and specific humidity of the CORE dataset, which are given at 10 m height, are used as the reference fields for the additional adjustments explained below, the height of the temperature and specific humidity data was shifted from 2 m to 10 m prior to the additional adjustments, as described in Appendix A.2. Also, the data on the reduced TL319 grid were interpolated onto the normal TL319 grid, as explained in Appendix A.1. The 10-m values were computed using the sea-surface temperature from COBESST, the ice-surface temperature from the brightness temperature of JRA-55, the adjusted equivalent neutral 10-m wind field explained in Section 3.4, and the bulk formula of Large and Yeager (2009) with properties of moist air calculated by the formulas given in Appendix B.

Smooth transition of temperature and specific humidity around the marginal sea-ice zones. Because the atmospheric model of JRA-55 does not allow partial sea-ice cover, the air temperature can change abruptly in the marginal sea-ice zones. Therefore, to improve the representation of warmer air over partial sea-ice cover, the air temperature over the marginal sea-ice zones was smoothed by applying 20 passes of a 9-point filter. Fig. 5a shows a schematic of the 9-point filter. In this operation, the temperature was left unchanged in regions of open water as well as in regions of almost total sea-ice cover (where the daily area fraction of sea-ice exceeds 0.99) using the daily sea-ice distribution from COBESST. The number of passes (20) was determined rather

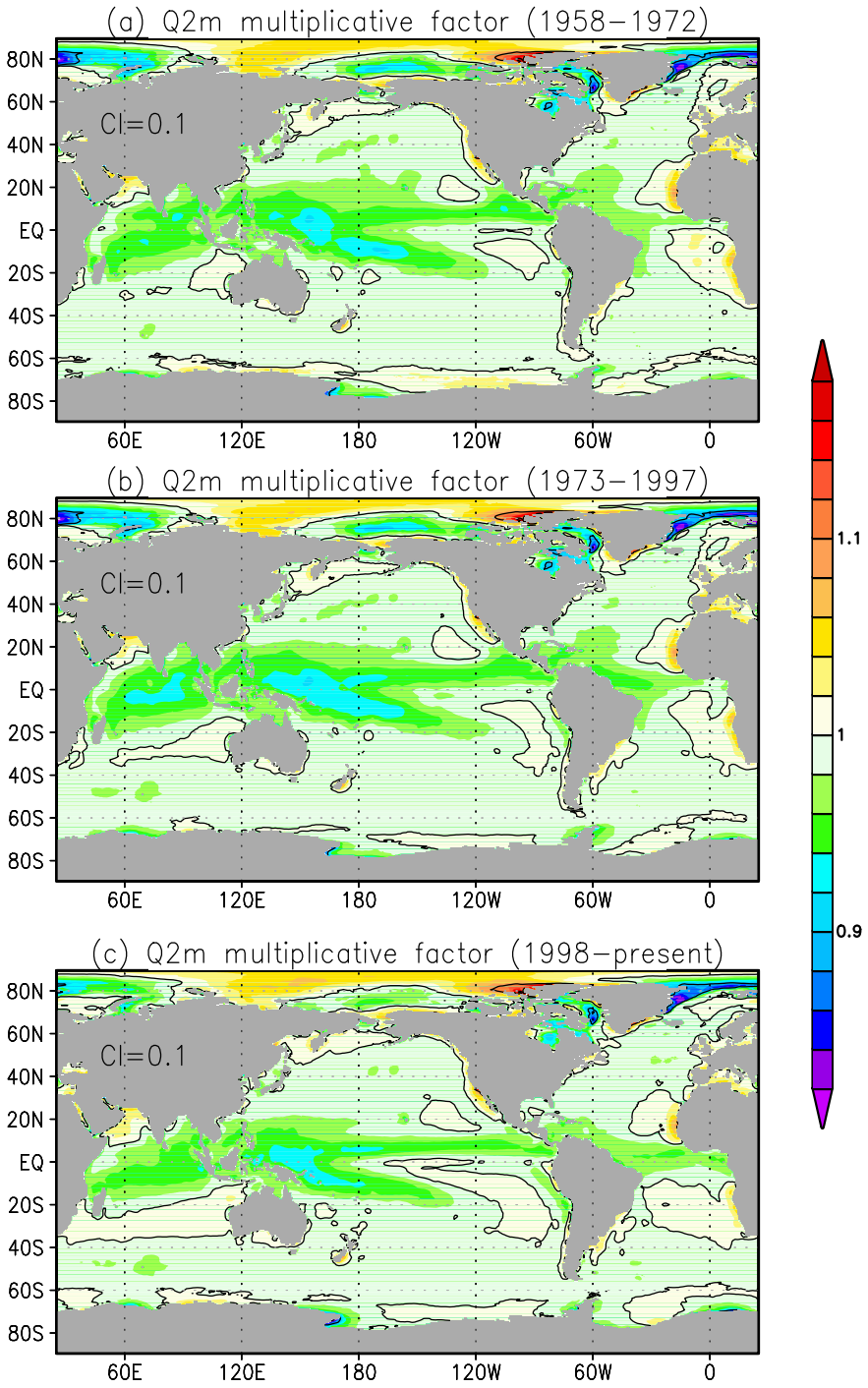

Fig. 4. Global distributions of the annual mean multiplicative factors for the specific humidity. Before applying these factors, the specific humidity was adjusted to the modified air temperature to keep the original relative humidity. (a) phase-I (1958–72), (b) phase-II (1973–97), and (c) phase-III (1998–present). The base time periods used for computing climatologies are 1980–1996 (JRA-55C), 1980–1996, and 1999–2014, respectively, for the three phases.

subjectively. The response function shown in Fig. 5b shows that small scale features (less than 500 km) are removed, implying that the air temperatures over open water and almost total sea-ice cover are linearly connected by this adjustment if the width of the marginal sea-ice zone is less than 500 km. As in the main adjustment, the specific humidity was modified along with the temperature. Fig. 6 shows the changes in air temperature in the winter of each hemisphere which result from this additional adjustment. The filter smoothed the step-like discontinuity of air temperature at the boundary between open water and sea-ice by raising temperature on the sea-ice side. Thus, only positive differences appear in the marginal sea-ice zones.

Cut-off of extremely low air temperature around Antarctica. The air temperature around Antarctica was adjusted as described by Large and Yeager (2004; 2009) for the CORE datasets. In the CORE datasets, the extremely low temperatures were cut off by applying an

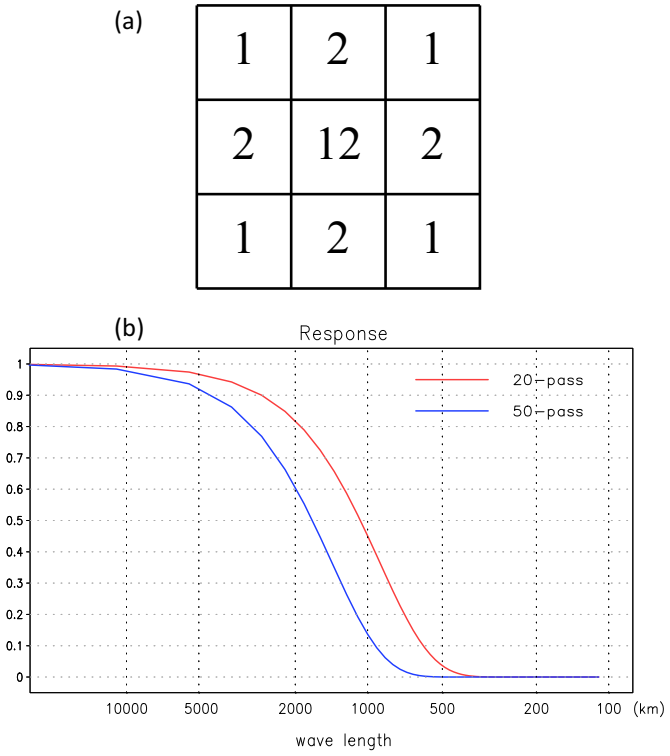

Fig. 5. (a) Relative weights for the participating grid points of the 9-point filter used in the smoothing operations. (b) Response of the filter functions for a meridionally homogeneous distribution case. (red) 20 passes of a 9-point filter. (blue) 50 passes of a 9-point filter. (For interpretation of the references to colour in this figure legend, the reader is referred to the web version of this article.)

annual cycle of the minimum temperature based on weather station and drifting buoy (Bryan, Personal Communication, 2002). For JRA55-do, we used the same formula for the annual cycle of the minimum temperature. Specifically, $T_{\min}(\phi, t)$ is defined as a function of latitude (ϕ) south of 60°S obtained by fitting sinusoidal curves to the observed monthly minimum temperature:

$$T_{\min}(\phi, t) = (b_0 + b_1\phi) + c_0(t)(a_0 + a_1\phi), \tag{15}$$

with $a_0 = -21.841\,(℃)$, $a_1 = -0.477\,(℃\,\text{degree}^{-1})$, $b_0 = 61.846\,(℃)$, $b_1 = 1.107\,(℃\,\text{degree}^{-1})$, and

$$c_0(t) = \cos(2\pi t/t_{1\text{year}} - \psi_0), \text{where} \psi_0 = 0.298(\text{radian}) \sim 17\text{January}, \tag{16}$$

where t represents the time since the beginning of a year, whose total time is $t_{1\text{year}}$. At 70°S, the maximum and minimum of $T_{\min}$ is − 4. 095°C and − 27. 193°C, respectively. To smooth the transition, the cut-off was extended northward toward 50°S using the time-dependent minima at 60°S ($T_{\min}(-60°, t)$). To summarise,

$$T(\lambda, \phi, t) = \max(T(\lambda, \phi, t), T_{\min}(\phi, t)), \quad \text{for } \phi \le -60°, \tag{17}$$

$$T(\lambda, \phi, t) = \max(T(\lambda, \phi, t), T_{\min}(-60°, t)), \quad \text{for } -60° < \phi < -50°, \tag{18}$$

where λ denotes longitude. Again, the temperature and specific humidity were modified together. Fig. 7 shows the resulting changes to air temperature and specific humidity during winter in the Southern Hemisphere. The air temperature is warmed by 5–10 Kelvin in the marginal sea-ice zone. The specific humidity is raised accordingly.

Adding the monthly anomaly of CORE to the temperature and specific humidity of the high-latitude regions during the pre-satellite period (1958–1978). The sea-ice distribution of JRA-55 is based on COBESST. In the pre-satellite period (1958–1978), the sea-ice distribution of COBESST in the Southern Hemisphere is largely based on climatology, so the inter-annual variabilities of the air temperature and specific humidity in the high-latitude Southern Hemisphere are unreliable. In the Northern Hemisphere, the sea-ice distribution of COBESST is based on Walsh and Chapman (2001) in the pre-satellite period, but the sea-ice extent of COBESST tends to be higher than the original data in the marginal sea-ice zones. Identifying the reason for this is beyond the scope of this paper - we simply consider how to remedy the discrepancy. In NCEP-R1, which is used as the basis for air temperature and specific humidity in the CORE dataset, sea-ice does not show such extensive distributions. Furthermore, NCEP-R1 uses various sea-ice analyses in addition to Walsh and Chapman (2001) prior to 1978 when available (Kalnay et al., 1996). In Fig. 8a, regions of extensive sea-ice distributions in the Labrador Sea in JRA-55 for the

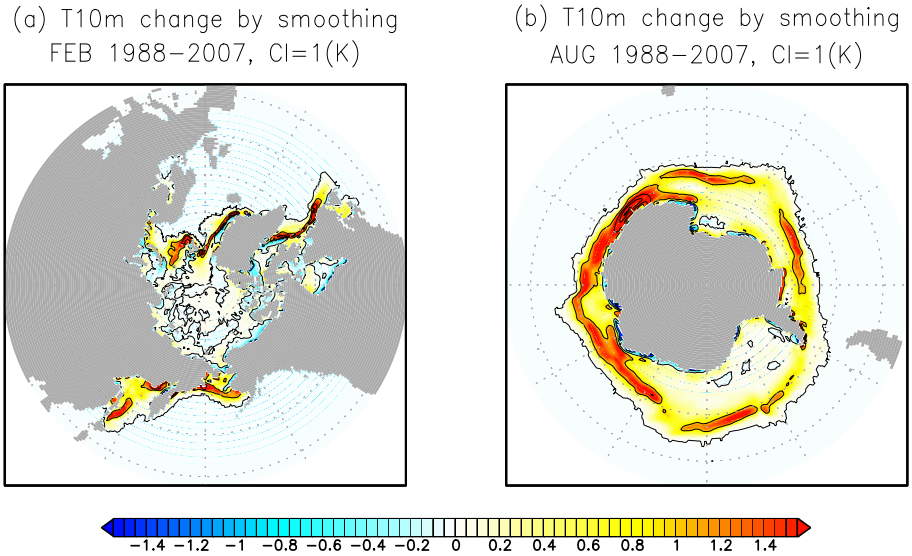

Fig. 6. Changes in 10-m air temperature (K) after additional adjustment (smoothing) in the marginal sea-ice zones. (a) February mean (1958–78) in the Northern Hemisphere. (b) August mean (1958–78) in the Southern Hemisphere.

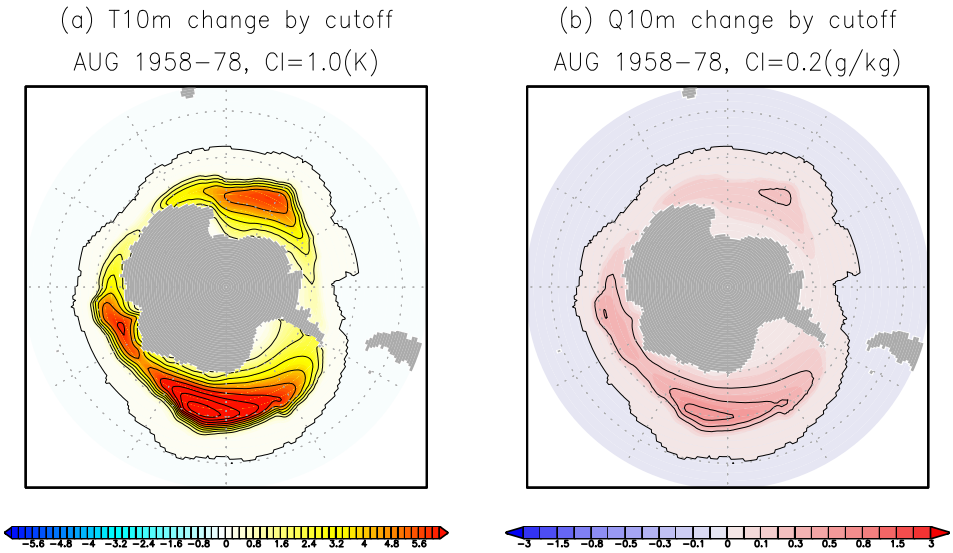

Fig. 7. Changes in (a) 10-m air temperature (K) and (b) specific humidity (g kg^{-1}) in August after applying an additional adjustment (low temperature cut-off) around Antarctica.

pre-satellite period (1958–1978) are marked as "X" and "Y", relative to the less extensive sea ice in NCEP-R1 for the same period (Fig. 8b). The latter exhibits better agreement with the Labrador Sea sea-ice fraction in both JRA-55 and NCEP-R1 for the satellite period (Fig. 8c and d), suggesting that the JRA-55 sea-ice fraction in the pre-satellite period is probably too high. As a result, the air temperature and specific humidity of JRA-55 tend to be suspiciously low in the marginal sea-ice zones, specifically in the Labrador Sea, in the pre-satellite period, which can result in unrealistically strong deep water formation in ocean models. Thus, at latitudes poleward of 40°N or 50°S, we added the time series of the difference of the temperature and specific humidity between the adjusted JRA-55 and CORE (CORE minus the adjusted JRA-55) to the adjusted JRA-55 fields for 1958–1978. The time-series was constructed by the linear interpolation in time of the monthly differences. The monthly differences were smoothed with 50 passes of a horizontal 9-point filter over the ice-free ocean, whose response function is shown in Fig. 5b. The smoothing removed the high wave number (wave length less than 1000 km) ripples in the air temperature field of CORE, which are traceable to NCEP-R1 (see also Appendix G.1). Fig. 9 shows the resulting changes in air temperature in the winter of each hemisphere. The air temperature is warmed in the Labrador Sea whereas it is cooled in the Arctic Ocean and around Antarctica. This operation was not applied to the western North Pacific region (40° − 65°N and 125° − 160°E), because the difference was large (warming) in the southern part of the Okhotsk Sea, which was due to a low sea-ice extent in the Okhotsk Sea used by NCEP-R1 in the pre-satellite period. This is marked as "Z" in Fig. 8b. In this region, the sea-ice distribution in the pre-satellite period of JRA-55 shows a better match with that in the satellite period than NCEP-R1.

3.4. Wind vector

3.4.1. Reference dataset

The main reference dataset for the surface wind vectors is the Remote Sensing Systems QuikSCAT Ku-2011 Daily Ocean Vector Wind on 0.25 ° grid Version 4 (Ricciardulli et al. 2011; Ricciardulli and Wentz 2015; hereafter referred to as QuikSCAT). We first computed the time series of the monthly scalar wind speeds, and the zonal and meridional components of the wind vectors, from daily data on the original 0.25° grid. At each grid point, the monthly data are used if available on more than one-third of the total number of days in that month. The time-series data were then mapped onto the reduced TL319 grid of JRA-55. The data gaps are caused by the shifting satellite orbits, rain contaminations, and the presence of sea-ice. In grid cells where the monthly data were not available, JRA-55anl wind data was used. This treatment should smooth the transition of the adjustment factors in the marginal sea-ice zones. From the derived monthly dataset, we generated time-series of the annual mean and its climatology on the reduced TL319 grid.

QuikSCAT wind is available from Aug 1999 to Oct 2009, sufficiently long for referencing phase-III. This is an improvement relative to the CORE dataset for which only 5 years of reference data was available for adjustment. In phases I and II, the wind speed was adjusted using an SSM/I-based wind speed product (Wentz, 2013). Because this product extends from 1988 to the present, the SSM/I wind speeds over the entire period were adjusted relative to the QuikSCAT wind speed during the Nov 1999 to Oct 2009 period. The adjusted speed then provided the reference for adjusting the JRA-55 wind speed. Because the wind vector components are not available from SSM/I, the adjustment factor for the wind direction used for phase-III were applied to phases I and II.

Because QuikSCAT and SSM/I measure equivalent neutral wind at 10-m height, the adjustment procedures are performed in terms of equivalent neutral wind. Accordingly, before filling the gaps in the satellite data, we converted the JRA-55anl wind to the equivalent neutral wind using the meteorological variables from JRA-55anl. Similarly, the JRA55-raw actual winds were converted to equivalent neutral winds before computing the adjustment factor using the surface air temperature and specific humidity at 2 m after the main adjustment explained in Sections 3.3.2 and 3.3.3. But as ocean–sea-ice models assume input of actual 10 m winds, the final step is to convert the adjusted JRA-55 equivalent neutral winds back to actual winds. This was done using the adjusted surface meteorological variables. In these conversions, we used the sea-surface temperature from COBESST, the ice-surface temperature from the brightness temperature of JRA-55, and the bulk formula of Large and Yeager (2009) with properties of moist air calculated by the formulas given in Appendix B.

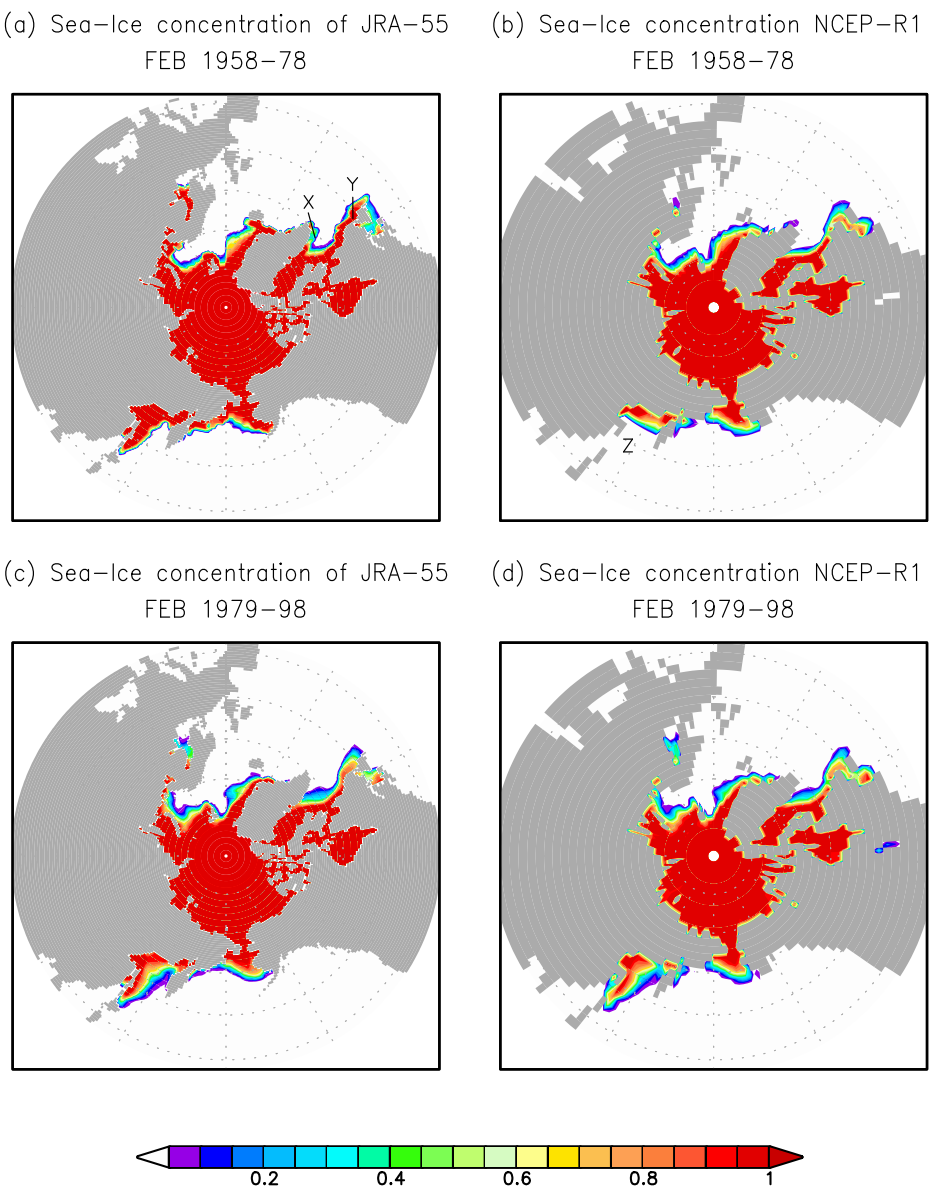

Fig. 8. February mean sea-ice concentration (area fraction) in the Northern Hemisphere before and after satellite in JRA-55 and NCEP-R1. Before-satellite (1958–78) mean of (a) JRA-55 and (b) NCEP-R1. After-satellite (1979–98) mean of (c) JRA-55 and (d) NCEP-R1. Problematic distributions in the pre-satellite era are indicated by "X" and "Y" (in the Labrador Sea) for JRA-55 (a) and "Z" (in the Okhotsk Sea) for NCEP-R1 (b).

3.4.2. Adjustment

Table 6 summarises the adjustment method for the wind vectors. The adjustment method is a slight modification of that described in Large and Yeager (2009) (see also Appendix C.3.1). The magnitude and direction of the wind vector were adjusted by an offsetting factor $\Delta W(\lambda, \phi)$ and a counter-clockwise rotating factor $\chi(\lambda, \phi)$, respectively, where λ and ϕ respectively denote longitude and latitude. These adjustment factors are constant in time. Specifically, the wind vector of JRA55-raw $(u_{\mathrm{JRA55}}, v_{\mathrm{JRA55}})$ at (λ, ϕ) was adjusted as follows:

$$\begin{pmatrix} u_{\mathrm{adj}} \\ v_{\mathrm{adj}} \end{pmatrix} = \frac{W_{\mathrm{JRA55}} + c\Delta W}{W_{\mathrm{JRA55}}} \begin{pmatrix} \cos\chi & -\sin\chi \\ \sin\chi & \cos\chi \end{pmatrix} \begin{pmatrix} u_{\mathrm{JRA55}} \\ v_{\mathrm{JRA55}} \end{pmatrix}, \tag{19}$$

where,

$$W_{\mathrm{JRA55}} = \max\left(\sqrt{u_{\mathrm{JRA55}}^2 + v_{\mathrm{JRA55}}^2},\ 0.3\,\mathrm{m\,s^{-1}}\right) \tag{20}$$

and

$$c = \tanh(d), \quad d = \frac{\max(W_{\mathrm{JRA55}} - 0.3\,(\mathrm{m\,s^{-1}}),\ 0)}{|\Delta W|}. \tag{21}$$

In (19), the offsetting factor for the wind speed (ΔW) was computed by subtracting the long-term average of JRA55-raw wind speed ($\overline{W}_{\mathrm{JRA55}}$) from that of the reference wind speed ($\overline{W}_{\mathrm{ref}}$):

$$\Delta W = \overline{W}_{\mathrm{ref}} - \overline{W}_{\mathrm{JRA55}}. \tag{22}$$

In (20), a $0.3\,\mathrm{m\,s^{-1}}$ floor on the equivalent neutral wind speed of JRA55-raw was introduced to avoid the zero division in (19). The factor c defined by (21) tapers the adjustment to ensure that wind speed is not modified for the minimum wind speed ($W_{\mathrm{JRA55}} = 0.3\,\mathrm{m\,s^{-1}}$): Adjustment is not applied ($c = 0$) for the minimum wind speed and gets closer to the full adjustment ($c = 1$) as the wind gets higher.

For wind direction, Large and Yeager (2009) computed the rotating

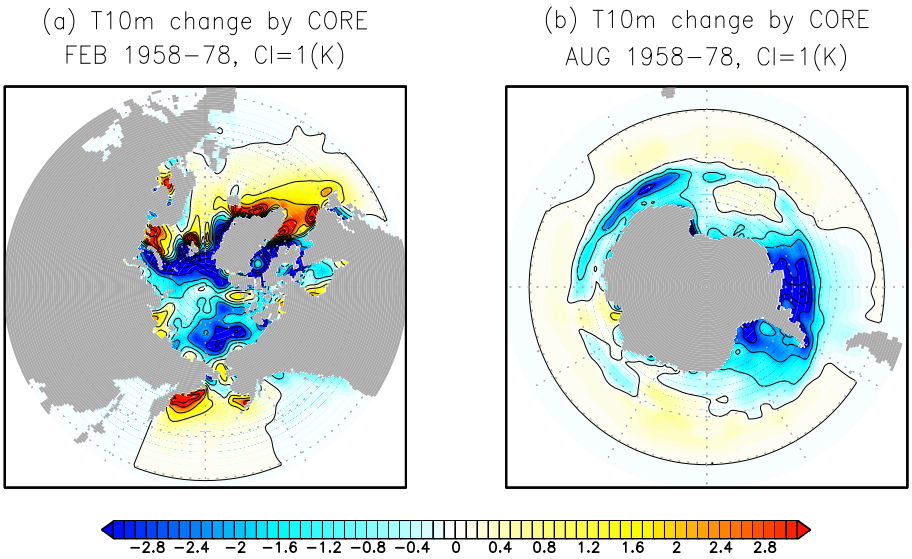

Fig. 9. Changes in 10-m air temperature (K) after additional adjustment (adding the CORE anomaly) at high latitudes. (a) February mean (1958–78) in the Northern Hemisphere. (b) August mean (1958–78) in the Southern Hemisphere.

Table 6
Summary of the computation of adjustment factors applied to wind vectors in the three phases.

Variable		Phase-I (1958–72)	Phase-II (1973–97)	Phase-III (1998–present)
10 m wind speed	Reference	SSM/I[a]	SSM/I[a]	QuikSCAT
	Raw data	JRA-55C[b]	JRA-55[b]	JRA-55[b]
	Period	1988–1996	1988–1996	Nov 1999–Oct 2009
10 m wind direction	Reference	same as phase-III	same as phase-III	QuikSCAT
	Raw data			JRA-55[b]
	Period			Nov 1999–Oct 2009

[a] Remote Sensing Systems SSM/I wind adjusted relative to QuikSCAT in Nov 1999–Oct 2009

[b] Grid noises found in the lee of mountains for the JRA-55 and JRA-55C wind fields are removed using a zonal 1-2-1 filter before determining adjustment factors.

factor as the angle difference between the long-term means of the reference and the NCEP / NCAR reanalysis. Because the angle differences could be very large (~ ± 180°) in low-wind regions, especially around the transitions between easterly and westerly, Large and Yeager (2009) introduced a tapering as a function of the magnitude of the vector average wind. For JRA55-do, we apply an analysis method used in the works of Kundu and Allen (1976) and Yoshikawa et al. (2007) who analysed low-frequency current fluctuations near the Oregon Coast and the relation between the surface wind vector and the vertical profile of the oceanic Ekman current, respectively. Specifically, we computed the rotating factor (χ) not from the angle differences, but using a Complex Empirical Orthogonal Function (CEOF) analysis. The CEOF can estimate the rotating factor in low-wind regions without requiring special treatment. First, we prepared time-series of the monthly mean wind vectors from the reference data and JRA55-raw during the Nov 1999–Oct 2009 period. A wind vector is expressed as a complex variable ($w = u + iv$). We then construct a complex matrix W, whose two columns contain the 10-year time-series of the monthly reference data and JRA55-raw. Next we computed the 2×2 covariance matrix $R = W^*W$, where W^* is the Hermitian transpose of W. The eigenvectors of R are CEOF modes of the time-series. If JRA55-raw largely reproduces the reference data, the first mode with a positive eigenvalue is the co-varying (correlated) mode. From the co-varying mode, we obtained the rotating factor for JRA55-raw as the angle between the components of the corresponding complex eigenvector. Preliminary analysis showed that the magnitude of the rotating factor tended to be large (> 45°) if the total energy accounted for by the first mode was small. Thus, a reduction factor (ξ) as a function of the total energy accounted for by the first mode, γ_1 ($= \frac{\lambda_1}{\lambda_1 + \lambda_2}$, where λ_1 and λ_2 are the eigen values of the 1st and 2nd mode, respectively), was introduced to taper the rotating factor:

$$\xi = \frac{1}{2}[1 + \tanh\{2(\gamma_1 - 0.9)\}]. \quad (23)$$

The transition of ξ occurs approximately from $\gamma_1 = 0.95$ ($\xi \sim 1$) to $\gamma_1 = 0.85$ ($\xi \sim 0$).

Fig. 10 shows the offsetting factor for the wind speed in the three phases. In all phases, the wind speed in the intertropical convergence zones is enhanced and that in the middle and high latitudes is reduced. The offsetting factor is generally smaller in phase-III than other phases because scatterometer winds were assimilated for the period corresponding to phase-III in JRA55-raw.

Fig. 11a shows the rotating factor for the wind direction over the entire period. Mid-latitude westerly winds are rotated equatorward in both hemispheres. Trade winds in the intertropical convergence zones are made more divergent. The first CEOF modes explain more than 95% of the total energy in most regions, specifically around the transitions between easterly and westerly (~ 30°N/S). Exceptions are found in several coastal regions (Fig. 11b). The eastern tropical North Pacific off the coast of Central America is one of those regions where the wind direction is strongly affected by orography. Simulation results should be interpreted with some care in those regions. Users interested in detailed exploration of the regions of problematic wind direction could modify the rotation scripts (which are freely available; see Appendix C), choosing perhaps to eliminate the rotation correction in these regions.

Fig. 12 compares the equivalent neutral wind speeds at 10-m height, zonally averaged over the ocean. The wind speeds are generally stronger in CORE than in QuikSCAT and JRA55-do, because the actual winds in CORE are directly adjusted relative to the equivalent neutral

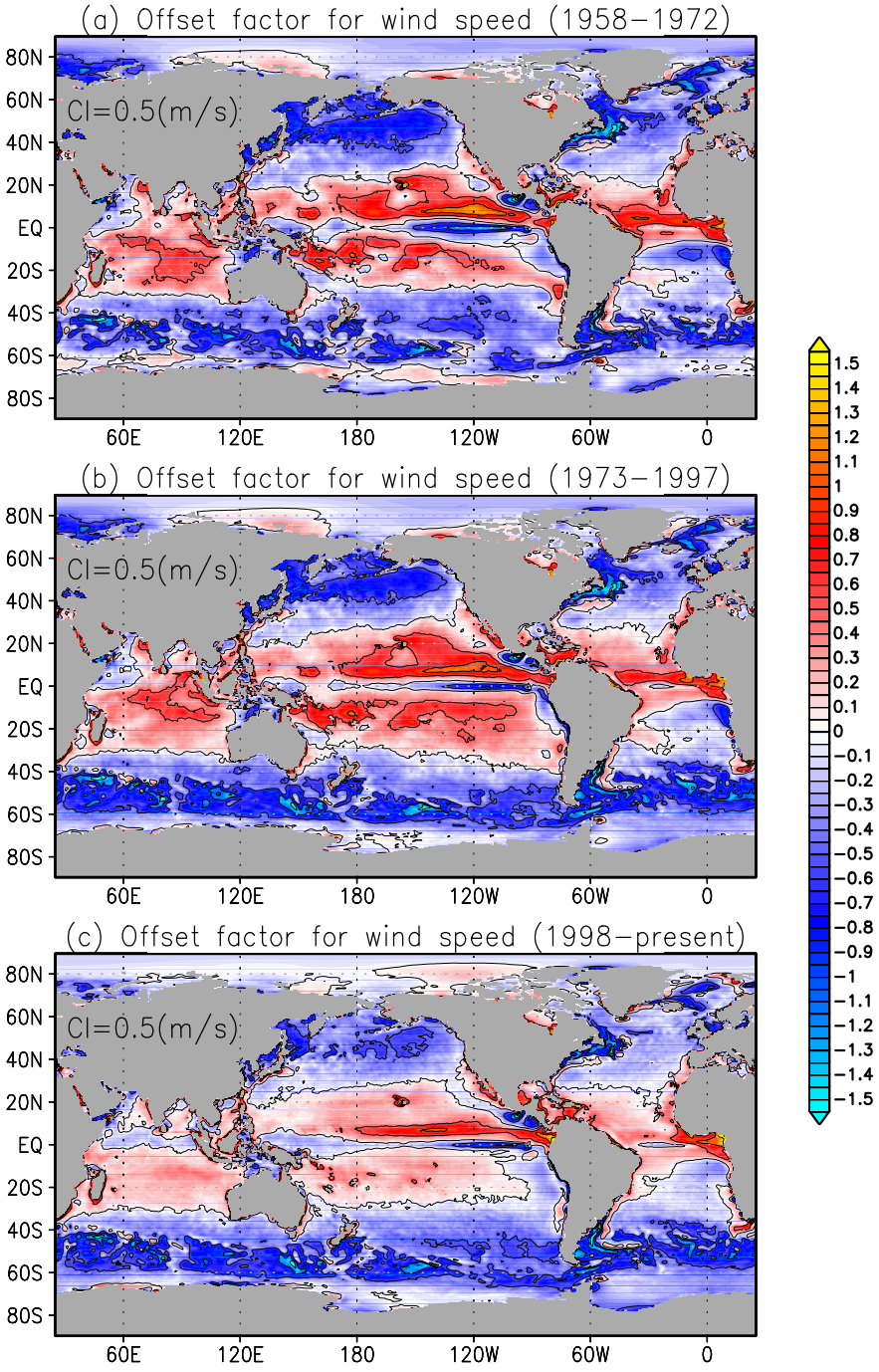

Fig. 10. Global distributions of the offsetting factor (ΔW, in $\mathrm{m\,s^{-1}}$) for wind speed in (a) phase-I (1958–1972), (b) phase-II (1973–1998), and (c) (1998–present).

winds in QuikSCAT. Indeed, when zonally averaged, the actual wind speed of CORE compares well with the equivalent neutral wind speed of QuikSCAT (results not shown). For further discussions on the comparisons across wind products, readers are referred to Taboada et al. (2018).

3.4.3. Comments on the adjustment of wind vector relative to satellite products

Because the microwave scatterometer (QuikSCAT) and radiometer (SSM/I) primarily infer the wind stress from surface wave fields, they essentially detect the surface wind speeds relative to the oceanic current at the sea-surface ($|\Delta\vec{U}|$ in Eq. (13)). Because the direction and speed of the surface wind usually influences the surface Ekman current, adjusting the wind speed by the above method slightly weakens and rotates the true wind vector. Moreover, the quasi-steady surface current can reach $1\,\mathrm{m\,s^{-1}}$ in the western boundary current and in the equatorial regions, and the surface current may reach several tens of $\mathrm{cm\,s^{-1}}$ within mesoscale eddies. In these cases, the difference between the absolute and relative wind vectors is non-negligible. Users of the present dataset should be aware of this limitation and its possible impact on their

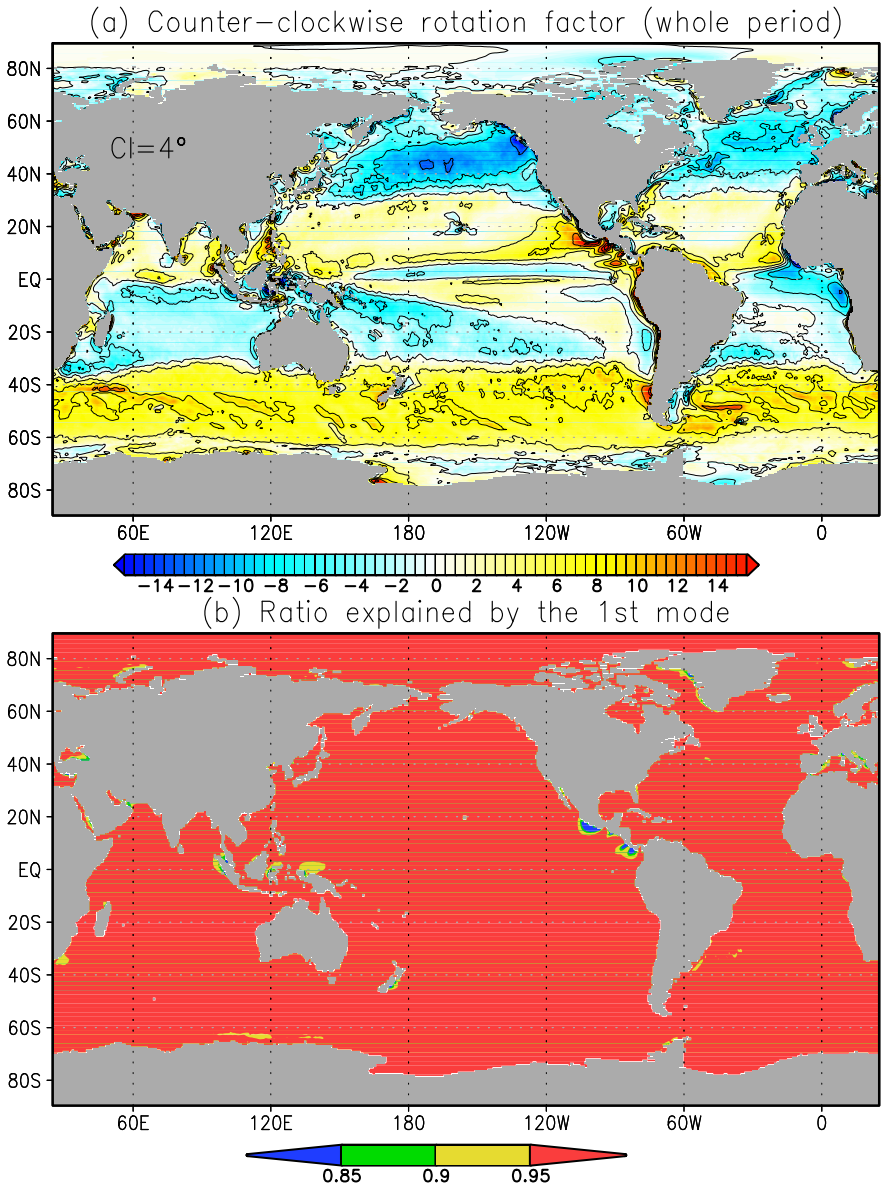

Fig. 11. Global distributions of (a) the rotating factor (χ, in degrees) for wind direction, with the positive sign denoting counter-clockwise rotation. (b) The ratio of the total energy explained by the first CEOF mode on which the rotating factor shown in (a) is based. The rotating factor with a low ratio is tapered with a formula given by Eq. (23).

simulated fields (e.g., Abel et al., 2017). In future work, the absolute wind vector ($\vec{U}_A$) could be estimated from the surface current ($\vec{U}_O$) derived in an oceanic reanalysis or state estimation (e.g., Rio et al., 2014). For this version, we provide a climatological mean surface current ($\vec{U}_{O_{\mathrm{clim}}}$) computed from the dataset of Rio et al. (2014). The climatology is based on the period used to construct the reference wind field from QuikSCAT (Nov1999–Oct2009). This climatological surface current could be added to the time series of the wind vector of this dataset to approximate the time-series of the absolute wind vector.

3.5. Shortwave and longwave radiation

3.5.1. Reference dataset

We used the CERES-EBAF-Surface_Ed2.8 data (Kato et al., 2013) as the reference dataset for the downward radiative fluxes. CERES-EBAF-Surface_Ed2.8 consists of surface irradiance fluxes as well as other variables derived from the Clouds and Earth's Radiant Energy System (CERES) satellite measurements of Top of Atmosphere (TOA) radiation (Loeb et al., 2012). EBAF (Energy balanced and Filled) refers to adjustments made to CERES data within its uncertainty to make it consistent with the estimated global average heat storage in the ocean of $0.50\mathrm{Wm}^{-2}$ (Loeb et al., 2012). The estimates of surface fluxes, derived from radiative transfer theory using data on clouds, atmosphere, surface and aerosol properties, are constrained to give TOA radiances that match CERES-EBAF in turn (Kato et al., 2013). CERES-EBAF-Surface_Ed2.8 (hereafter referred to as CERES) is considered a state-of-the-science product replacing the earlier ISCCP-FD dataset (Zhang et al., 2004) used in CORE. As the latest dataset of its kind, CERES has been widely used as a reference in verification studies. CERES data now cover 15 years, sufficiently long for comparisons with other data.

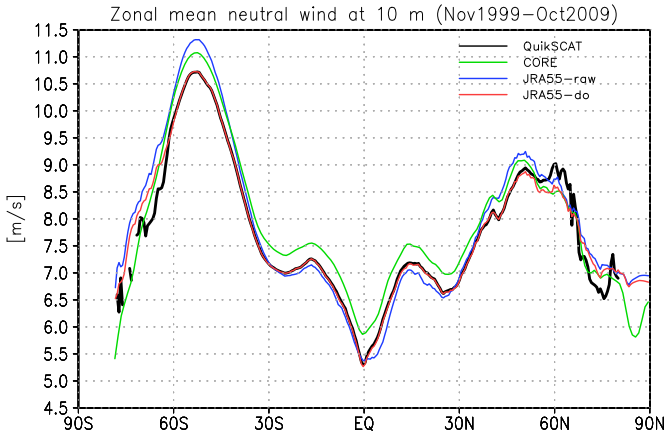

Fig. 12. Equivalent neutral 10-m wind speeds ($m\,s^{-1}$) zonally averaged over the ocean during the Nov 1999–Oct 2009 period; (green) CORE, (blue) JRA55-raw, (red) JRA55-do, and (black) QuikSCAT. The deviation of QuikSCAT from other datasets in high latitude regions is due to the absence of data over sea-ice and should not be compared with other datasets there. (For interpretation of the references to colour in this figure legend, the reader is referred to the web version of this article.)

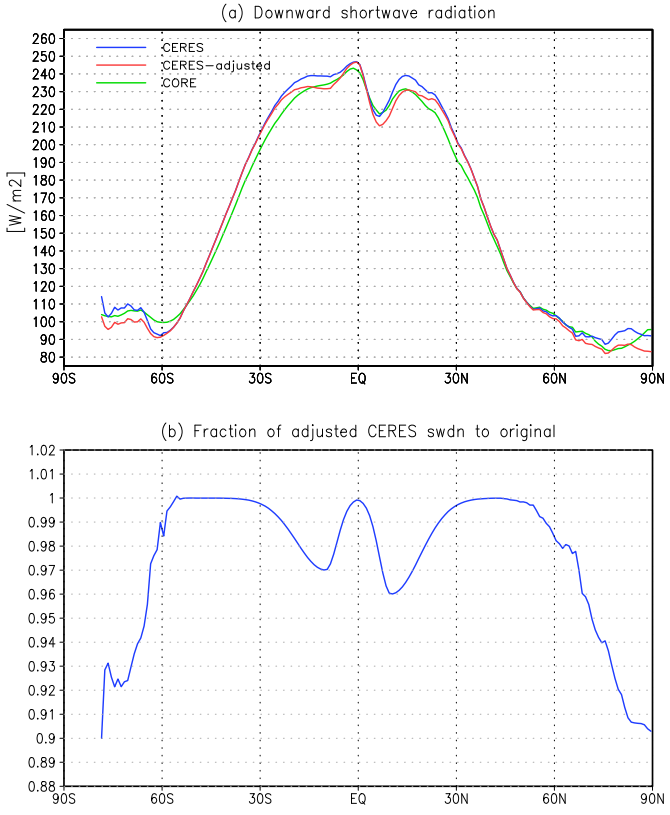

Fig. 13. (a) The downward shortwave radiation ($W\,m^{-2}$) zonally averaged over the ocean for 15-years (Mar 2000 through Feb 2015) derived from (blue) raw CERES and (red) adjusted CERES. For comparison, the data of CORE (green) are also depicted, but are averaged over the Jan 1984–Dec 2007 period. (b) The ratio of the adjusted CERES to the raw CERES shown in (a). This approximately represents the adjustment factor applied to the raw CERES as explained in Appendix E. (For interpretation of the references to colour in this figure legend, the reader is referred to the web version of this article.)

Table 7
Summary of the computation of adjustment factors applied to downward shortwave and longwave radiations in the three phases.

Variable		Phase-I (1958–72)	Phase-II (1973–97)	Phase-III (1998–present)
Downward shortwave radiation	Reference	JRA55-adj	Same as phase-III	CERES-EBAF adjusted
	Raw data	JRA-55C		JRA-55
	Period	1979–1996		Mar 2000–Feb 2015
Downward longwave radiation	Reference	JRA55-adj	Same as phase-III	CERES-EBAF
	Raw data	JRA-55C		JRA-55
	Period	1979–1996		Mar 2000–Feb 2015

Following Large and Yeager (2004; 2009), who produced the CORE data using ISCCP-FD radiation, we compared the CERES data with buoy observations and evaluated the necessity of adjusting them before their application to the reference fields. Accordingly, the shortwave radiation was reduced at low latitudes and over sea-ice by up to 4% and 10%, respectively (Fig. 13). However, the longwave radiation was left unadjusted. See Appendix E for details on the adjustments applied to CERES.

3.5.2. Adjustment

Table 7 summarises the adjustment procedure. The monthly multiplicative factors were identical in phases II and III, and were based on the 15-year (Mar 2000–Feb 2015) monthly climatologies of the adjusted CERES and JRA55-raw. The reference field in phase-I was the adjusted JRA-55 (JRA55-adj) downward radiation acquired from 1979 to 1996. The monthly climatologies of JRA55-adj and JRA-55C were compared over this period, and the adjustment factors over the 1958–72 period were then determined. Fig. 14 shows a comparison of the annual mean multiplicative factors in the two periods. Generally, the shortwave radiation is enhanced at low latitudes and reduced at high latitudes. The exception at low latitudes is the eastern part of subtropical oceanic basins, where the shortwave radiation is above the reference value and is reduced by the adjustment. The biases in the downwelling shortwave radiation are generally related to precipitation as will be shown in the next subsection. Notably, about a 30% reduction is required for shortwave radiation in the Southern Ocean, which implies insufficient clouds there in JRA-55. This is consistent with the analysis on the top of atmosphere presented by Kobayashi et al. (2015) (see Figs. 19 and 20 of Kobayashi et al. (2015)). The longwave radiation is adjusted in the opposite sense of the shortwave radiation, reflecting the compensatory nature of shortwave and longwave radiations in the radiative transfer models. When the climatological value in a grid point was below $5 Wm^{-2}$, as occurred for shortwave radiation in the polar night region, the multiplicative factor for that month was set to unity.

Fig. 15 compares the zonally averaged downward shortwave and longwave radiations over the ocean. Overall, the large bias found in JRA55-raw was successfully corrected in JRA55-do. The JRA55-do and CORE datasets are comparable.

3.6. Precipitation

3.6.1. Reference dataset

The precipitation adjustment was referenced to the CORE dataset. The precipitation field of the CORE dataset is comprised of several data sources. The global ocean is separated into several latitude bands and an appropriate dataset is chosen for each. From the south, the Global Precipitation Climatology Project (GPCP; Huffman et al., 1997) for

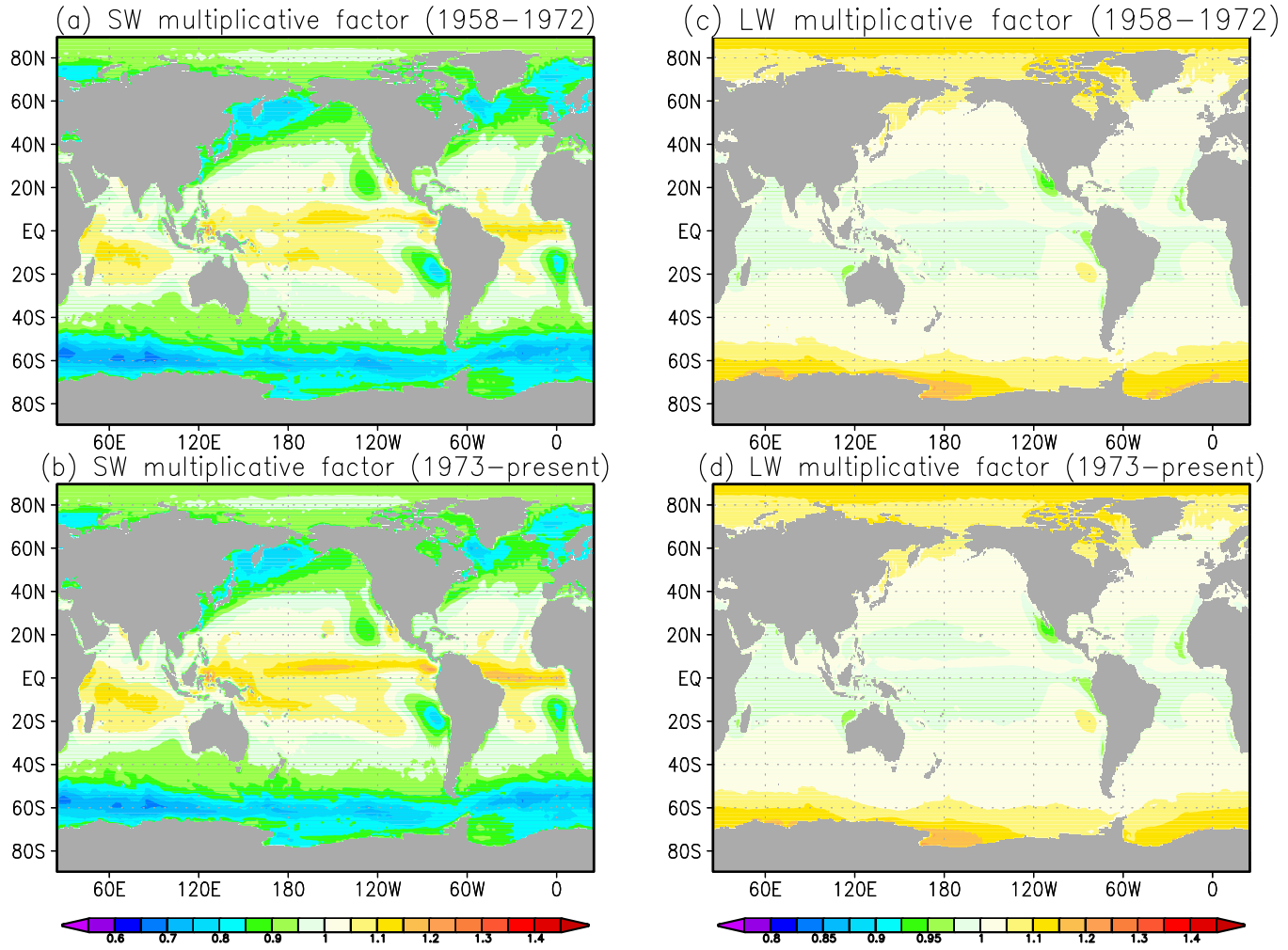

Fig. 14. Global distributions of the multiplicative factor applied to the downward (a, b) shortwave and (c, d) longwave radiation fluxes of JRA-55. (a, c) phase-I (1958–72), and (b, d) phase-II and phase-III (1973–present).

poleward of 65°S, CPC Merged Analysis of Precipitation (CMAP; Xie and Arkin, 1996) for 65°S– 30°S, GPCP for 30°S– 30°N, CMAP for 30°N– 70°N, and a combined Serreze and Hurst (2000) and Yang (1999) climatology for the Arctic poleward of 70°N. The data with interannual variability is only available after 1979.

In the earlier version of the dataset, the global ocean averaged precipitation showed a rapid increase during the most recent decade, which was not found in the GPCP-v2.3 dataset (Adler et al., 2003) (see also Appendix C.3.2). This is thought to be caused by the introduction of GNSS-RO (Global Navigation Satellite System-Radio Occultation) in 2006 as well as the increase in the number of radiance observations from satellite water vapor channels. Because it is not desired that the enhanced precipitation remains in the updated data in the future, phase-III is further divided at 2006 and different adjustment factors are computed for the first and second halves (phase-IIIa and phase-IIIb, respectively). We used the CORE dataset for the first half. In the second half, we used a product based on the GPCP-v2.3 dataset because the CORE dataset is only available until 2009. Because GPCP-v2.3 extends from 1979 to the present, the GPVP-v2.3 precipitation over the entire period were first adjusted relative to the CORE dataset during the 1979 to 2009 period. Thus, the adjusted precipitation provides the reference for adjusting the JRA-55 precipitation for phase-IIIb.

3.6.2. Adjustment

Table 8 summarises the adjustment method. The monthly multiplicative factors $f(\lambda, \phi, t)$ with thresholds ($1/3 \le f \le 3$) were determined from the monthly climatologies of JRA55-raw and the adjusted GPCP-v2.3 in phase-IIIb during the 2006–2015 period, JRA55-raw and CORE during the 1999–2006 period in phase-IIIa, and the 1979–1996 period in phase-II. The adjustment factor in phase-I was determined by comparing the monthly climatology between JRA-55C and CORE from 1979 to 1996. The purpose of thresholds (f) was to avoid excessive correction, such as extreme rainfall events ($f = 3$) and the overall removal of moderate rainfall events ($f = 1/3$). The choice of the specific factors of 1/3 and 3 is subjective. Fig. 16 compares the multiplicative factors for the four phases. The factors are qualitatively similar. Precipitation must be reduced in the intertropical convergence zones and enhanced toward the west of the continents at low latitudes. Fig. 16 also implies that the areas affected by the thresholds on the multiplicative factors are very small, justifying the present choice.

Fig. 17 compares the zonally averaged precipitation over the ocean. Precipitation in the intertropical convergence zones is exaggerated in JRA55-raw, but is comparable with the CORE data in JRA55-do. The reason for the excessive precipitation in JRA55-raw was discussed by Kobayashi et al. (2015). According to the authors, large moistening increments occur in the region near the intertropical convergence zones

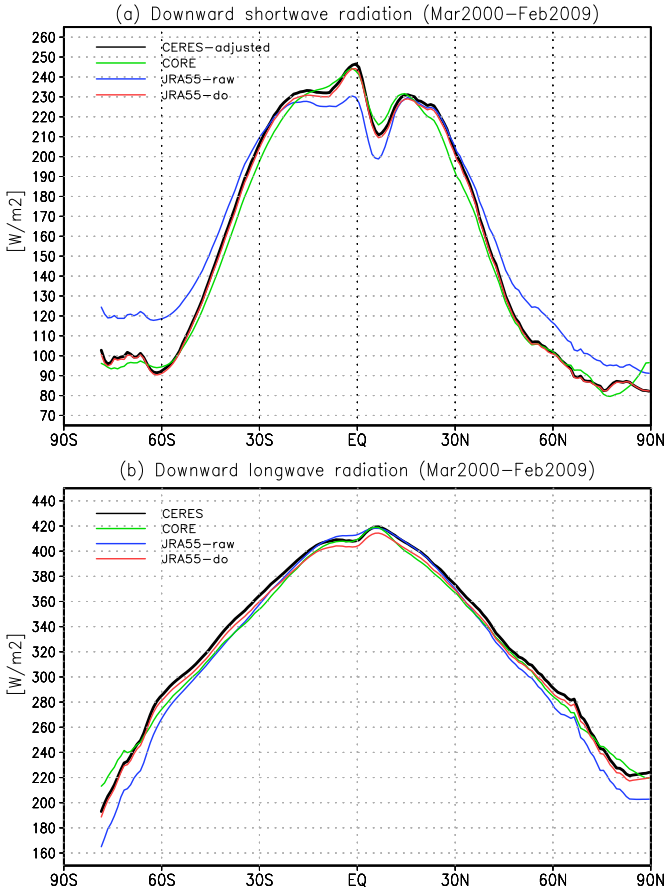

Fig. 15. (a) Downward shortwave and (b) downward longwave radiation at the surface (W m^{-2}) zonally averaged over the ocean; (green) CORE, (blue) JRA55-raw, (red) JRA55-do. Note that in JRA55-do, the JRA55-adj data are multiplied by 0.98863 (see Section 5). (For interpretation of the references to colour in this figure legend, the reader is referred to the web version of this article.)

in order to correct the dry bias in the upper and middle troposphere tending to appear in the first guess. This results in the large precipitation seen near the intertropical convergence zones in JRA-55.

3.6.3. Additional adjustment in the Mediterranean

After the first adjustment, the precipitation remained exaggerated in the Mediterranean during the 1958–1978 period (Fig. 18). This is due to processing errors on some of the radiosonde data used in JRA-55 in 1960s to 1970s. The impact of this error on oceanic precipitation was limited except for the Mediterranean. This excessive precipitation, which might affect transport at the Strait of Gibraltar, was corrected by estimating the annual precipitation over the Mediterranean from 1958 to 1978. The estimation is described below.

The precipitation on the land around the Mediterranean was first calculated using Global Precipitation Climatology Center (GPCC; Schneider et al., 2011) data from 1958 to the present. Additionally, the precipitation over the Mediterranean was calculated from CORE for the 1979–2009 period (when the inter-annual variability of precipitation was available in this dataset). To estimate the annual mean precipitation in the Mediterranean from the precipitation over the land, we computed the ratio of the long-term (1979–2009) mean ocean (CORE) precipitation to the land (GPCC) precipitation, and applied it to the time series of the annual mean land precipitation from GPCC. The estimated annual mean correlates well with the ocean precipitation from CORE (c.f. the black and green lines in Fig. 18). Thus, the adjusted JRA-55 precipitation on the Mediterranean was calibrated by the estimated annual ocean precipitation over the 1958–1978 period.

The annual mean precipitation integrated over the Mediterranean in the adjusted JRA-55 was compared with the yearly precipitation estimated from GPCC. The ratio of the two values defines the calibration factor for the given year. The annual calibration factors were linearly interpolated in time and applied to the instantaneous Mediterranean precipitation values in the adjusted JRA-55. The result (JRA55-do) is depicted as the red line in Fig. 18.

4. Runoff

The main part of the river runoff (freshwater discharge at river mouths) was taken from a dataset presented in Suzuki et al. (2017). In this dataset, the river discharge to the ocean was calculated by the global river-routing model CaMa-Flood (Yamazaki et al. 2011; Yamazaki et al. 2013). The input runoff from the JRA-55 land-surface model is then routed to oceans along the river network map, which is fitted to the land-surface model. The longitudinal and latitudinal resolution of the model is 0.25°.

The input runoff from the land-surface component of JRA-55 contains biases that were corrected by the multiplicative factors as explained by Suzuki et al. (2017). In this correction, the input runoff was adjusted so that CaMa-Flood gives the river discharge into the ocean that fits with that reported by Dai et al. (2009). The river discharge data of Dai et al. (2009) were extended to 2015 by a linear regression using the annual total precipitation of GPCP-v2.3 (Adler et al., 2003) on the drainage basins. The multiplicative factor applied to the input runoff is estimated as the ratio of the river discharge by Dai et al. (2009) to the total input runoff from the land-surface component of JRA-55 in each drainage basin. Before this estimation, a low-pass filter (a 5-year Lanczos window) was applied to both input runoff and river discharge. The factors were fixed before 1962 and after 2011 at the values for 1963 and 2010, respectively. The choice of 1963 is to exclude the first 3 years (1958–1960) from the computation of the adjustment factor. During 1958–1960, precipitation over land showed significant variability that resulted in the large variation of the river discharge (Fig. 19). The choice of 2010 is because after 2010 no distinctive time-dependent

Table 8
Summary of the computation of adjustment factors applied to precipitation in the four phases.

Variable		Phase-I (1958–1972)	Phase-II (1973–1997)	Phase-IIIa (1998–2006)[a]	Phase-IIIb (2006–present)[a]
Precipitation	Reference	CORE	CORE	CORE	GPCP-v2.3[b]
	Raw data	JRA-55C	JRA-55	JRA-55	JRA-55
	Period	1979–1996	1979–1996	1999–2006	2006–2015

[a] Transition of the adjustment factors between phases IIIa and IIIb occurs during 2006.
[b] GPCP-v2.3 adjusted relative to CORE in 1979–2009.

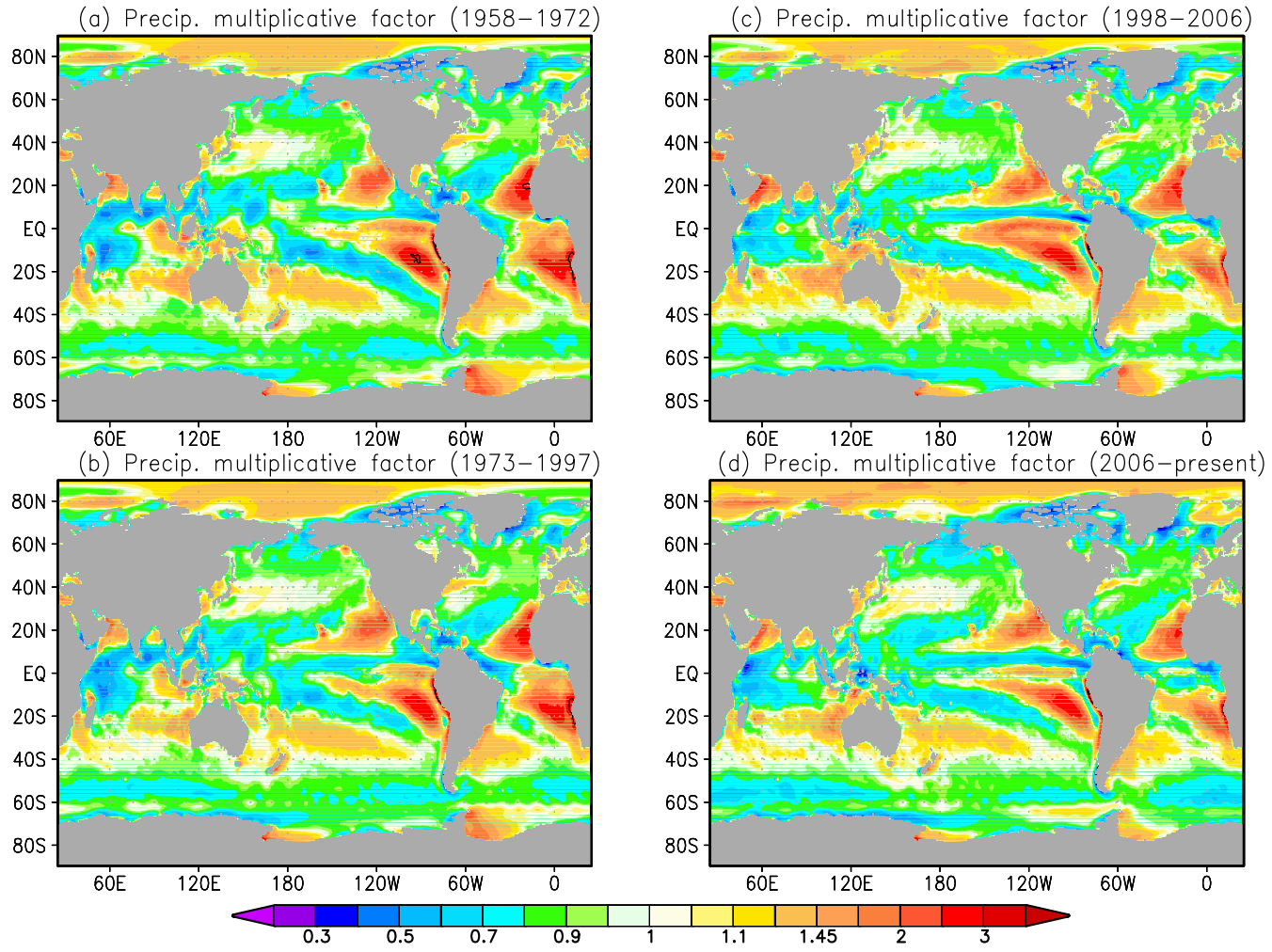

Fig. 16. Global distributions of the annual mean multiplicative factor (f) for precipitation, applied in (a) phase-I, (b) phase-II, (c) phase-IIIa and (d) phase-IIIb. Contours are depicted for 0.34 and 2.9 to infer the regions where the factors are affected by the applied thresholds ($1/3 \leq f \leq 3.0$).

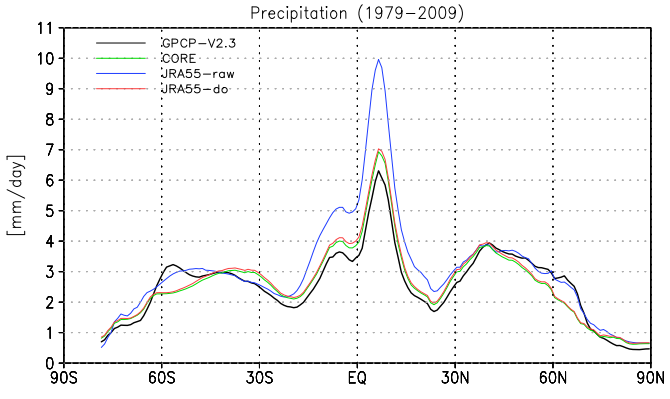

Fig. 17. Zonally averaged precipitation over the ocean (mm day^{-1}) during the 1979–2009 period; (green) CORE, (blue) JRA55-raw, (red) JRA55-do. Note that in JRA55-do, the JRA55-adj data are multiplied by 1.02118 (see Section 5). (For interpretation of the references to colour in this figure legend, the reader is referred to the web version of this article.)

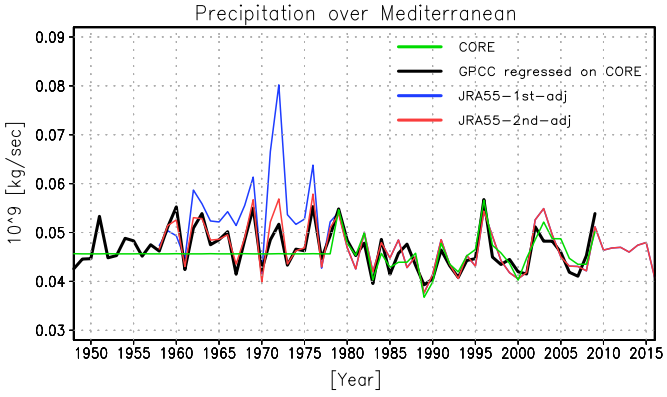

Fig. 18. Time-series of the annual mean area-integrated precipitation over the Mediterranean ($\times 10^9$ kg s^{-1}). CORE inter-annual forcing version 2 (green), adjusted JRA-55 (blue), additionally adjusted JRA-55 (red), and an estimate from GPCC precipitation on the coast around the Mediterranean as described in the text (black). (For interpretation of the references to colour in this figure legend, the reader is referred to the web version of this article.)

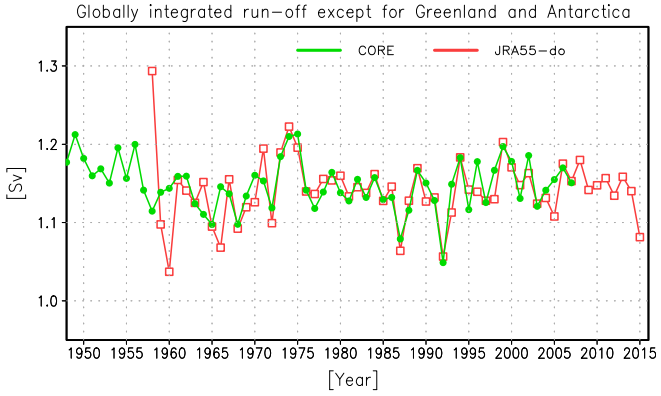

Fig. 19. Time-series of the annual mean global ocean-integrated river runoff in (green) CORE and (red) JRA55-do excluding the runoffs from Greenland and Antarctica. Units in $10^9\,kg\,s^{-1}$. (For interpretation of the references to colour in this figure legend, the reader is referred to the web version of this article.)

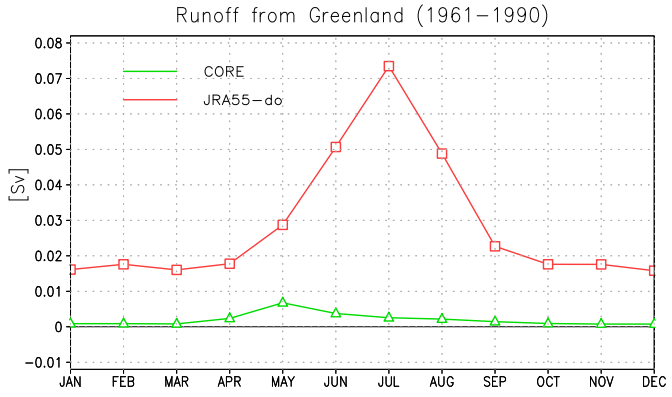

Fig. 20. Monthly climatology of runoff from Greenland in (green) CORE and (red) JRA55-do. Units in $10^9\,kg\,s^{-1}$. (For interpretation of the references to colour in this figure legend, the reader is referred to the web version of this article.)

biases were seen in JRA-55 and the assimilation method of JRA-55 was frozen. To moderate the correction, the multiplicative factor was confined to 0.2–5.0. These procedures were applied to 38 major continental rivers with large river discharge, and to seven rivers with a large drainage-basin area (see Suzuki et al. (2017) for the list of these rivers). These rivers were selected because they are well resolved by the model with the 0.25° × 0.25° spatial resolution. The river discharge from the remaining small rivers was separated into 12 divided ocean basins (the western and eastern part of the three major (Atlantic, Pacific, and Indian) Oceans, the Arctic Ocean, the Mediterranean, Black, Baltic, and Red Seas, and the Hudson Bay). In the above adjustment procedure, the total input runoff into the small rivers was adjusted to match the sum of the river discharges from the divided basins (excluding the discharges of the 45 major rivers). The depths and widths of the 38 major continental rivers in CaMa-Flood were tuned ad-hoc to fit the climatology of the seasonal cycle with that of Dai et al. (2009).

Fig. 19 compares the time series of the annual mean, global ocean-integrated river discharges into the oceans in the CORE dataset (Dai et al., 2009) and the CaMa-Flood simulation of Suzuki et al. (2017). The simulated annual mean river discharges vary similarly to the discharges from the major continental rivers reported by Dai et al. (2009), partly because the long-term input was adjusted to Dai et al.'s (2009) data by the time-dependent multiplicative factor. The excessive river discharge in 1958 of JRA55-do occurred because the high runoff from the land-surface component of JRA-55 of that year could not be appropriately corrected by the present adjustment method that uses the multiplicative factor for 1963 during the period 1958–1962.

The river model used by Suzuki et al. (2017) is suitable only for liquid water. Thus, in basins with significant runoff in the solid phase, such as Greenland and Antarctica, we used climatologies of existing datasets (namely, the climatologies of Bamber et al. (2012) for Greenland and Depoorter et al. (2013) for Antarctica). We provide them as the total (i.e., liquid plus solid) river runoff in the main dataset. The separate components are also provided, if available (Appendix C). We used a monthly climatology of Greenland runoff for JRA55-do, because the interannually varying dataset is available only until 2010. This will be modified when an update to Bamber et al. (2012), which extends the seasonally-varying time-series to 2016 and will be imminently available

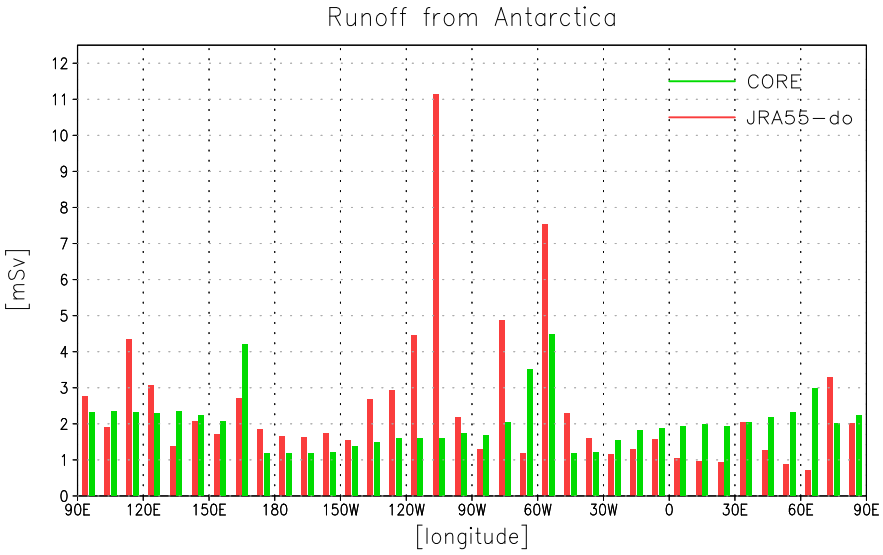

Fig. 21. Runoff from Antarctica divided into longitudinal bins at 10° intervals; (green) CORE and (red) JRA55-do. Units in $10^6\,kg\,s^{-1}$. In CORE, the runoff is uniformly distributed on the coastal grid cells. Therefore, the non-uniform distribution of the 10° bins reflects the different numbers of coastal grid cells contained in each bin. (For interpretation of the references to colour in this figure legend, the reader is referred to the web version of this article.)

(Bamber et al., 2018) (Appendix C). The climatology is based on the period 1961–1990, after which the total river runoff started to increase rapidly (Bamber et al., 2012). During the 1961–1990 period, the annual mean total river runoff from Greenland is 0.0278 Sv in JRA55-do and 0.002 Sv in CORE. That is, the total river runoff from Greenland is an order of magnitude higher in JRA55-do than that in CORE. Fig. 20 compares the monthly climatology of the total river runoff from Greenland in the two datasets. The seasonal variability of the total river runoff also differs between JRA55-do and CORE. Bamber et al. (2012) utilises a high-resolution regional climate model, validated with in-situ observations, alongside observations of solid ice discharge. However, there was no gauges along the coastal Greenland in the runoff dataset of Dai et al. (2009) on which CORE is based. Consequently, JRA55-do is considered to be more realistic than CORE for Greenland.

For Antarctica, the annual mean runoff of the liquid and solid phases was represented by ice shelf basal melt and calving flux respectively, as provided by Depoorter et al. (2013). Prior to this study, it was believed that iceberg calving was, by far, the dominant *runoff* mechanism but it is now evident that ice shelf bottom melting is of equal magnitude and importance. Depoorter et al. (2013) provides a "snapshot" of the fluxes for the year 2009. For parts of West Antarctica, both bottom melting and calving have increased over at least the last 15 years (Paolo et al., 2015). In East Antarctica, however, the fluxes have been relatively stable during the satellite era and the 2009 value is a reasonable estimate of the long-term value. For West Antarctica, this is a less valid assumption, even though the difference is only on the order of 9 mSv (Paolo et al., 2015). In Depoorter et al. (2013), the average annual mean of the liquid-plus-solid runoff from Antarctica is 0.0876 Sv, versus 0.073 Sv in CORE. In contrast to CORE, JRA55-do provides a spatially variable Antarctic runoff, based on observations. In Fig. 21, the runoff from Antarctica is divided into longitudinal bins at 10° intervals. Note that the non-uniform distribution of the 10° bins in CORE reflects the different numbers of coastal grid cells contained in each bin. The runoff is generally higher in JRA55-do than in CORE, except the region (30°W– 70°E), including the eastern part of the Weddell Sea (0° – 30°E), and the region (130° – 170°E), including the eastern part of the Eastern Indian Ocean Sector, where it is higher in CORE.

For the 1998–2007 period, the global ocean-integrated annual mean runoff in JRA55-do totals 1.2566 Sv, approximately 0.03 Sv larger than in CORE (1.2229 Sv). The difference is mainly sourced from the different runoffs of Greenland and Antarctica in the two datasets. The

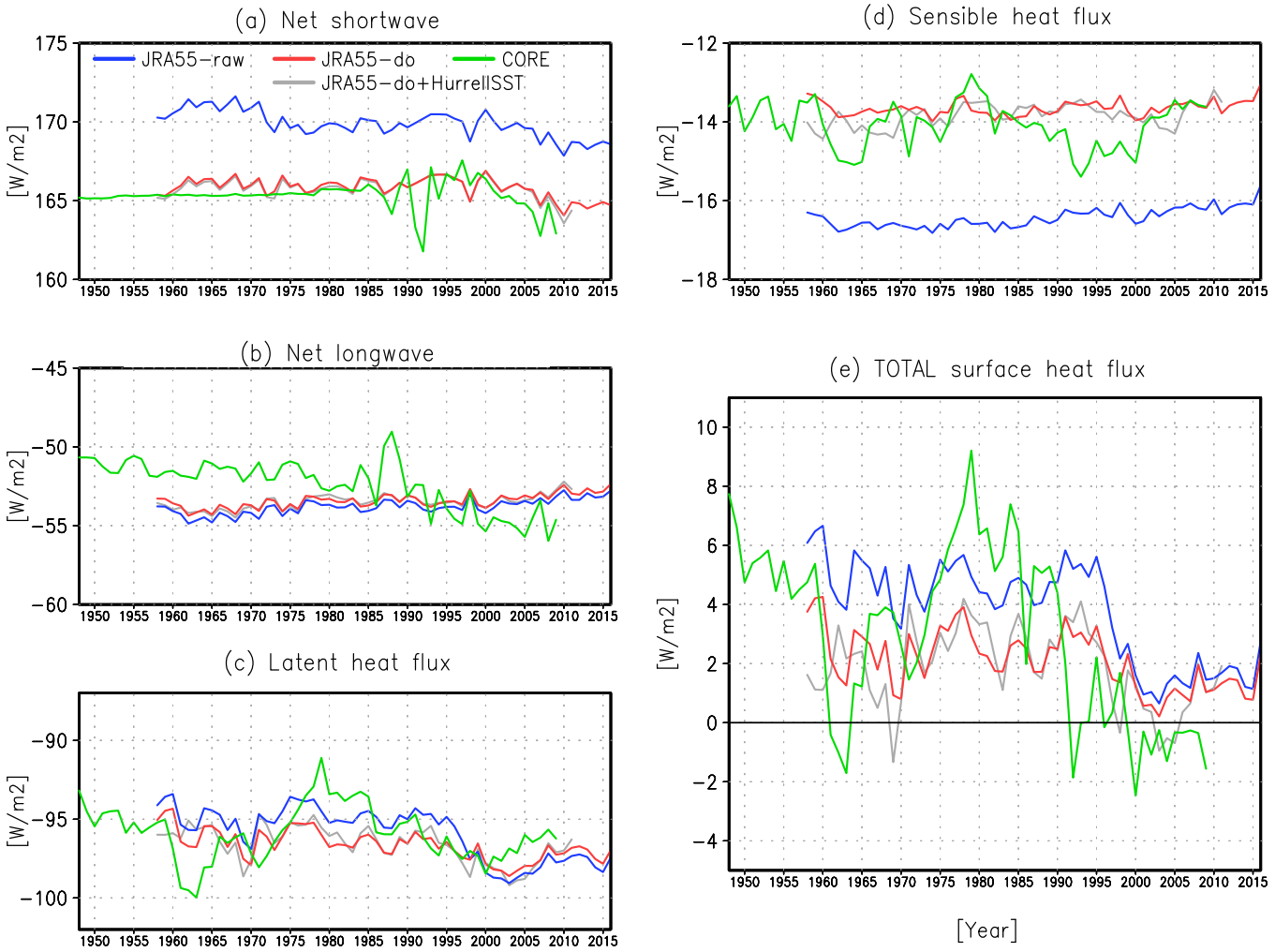

Fig. 22. Time-series of the annual mean global ocean averaged total heat flux, and its separate components (W m^{-2}). Compared are the results from three datasets; CORE inter-annual forcing version 2 (green), JRA55-raw (blue), and JRA55-do (red). The lower boundary condition is taken from COBESST (Ishii et al., 2005). Albedo and bulk formula are taken from Large and Yeager (2009), and the formulae for the air properties are from Gill (1982) (see Appendix B). For JRA55-do, the SST dataset by Hurrell et al. (2008) which was used to evaluate the CORE dataset by Large and Yeager (2009) is applied and plotted with grey lines. (For interpretation of the references to colour in this figure legend, the reader is referred to the web version of this article.)

original intent was that any new river runoff dataset incorporated into this project would be adjusted to match its long-term mean (1988–2007) with that of CORE (1.22 Sv). However, we have now decided to refer to new datasets to the total runoff of the present dataset (1.26 Sv). Taking the oceanic area as $3.654 \times 10^{14}\,\mathrm{m}^2$, this runoff is equivalent to a global ocean averaged freshwater flux of $3.44 \times 10^{-6}\mathrm{kg\,m^{-2}s^{-1}}$.

5. Final adjustment for achieving global balance

After making the main and additional adjustments described in the previous sections, we computed the heat and freshwater fluxes using COBESST (Ishii et al., 2005), the albedo and bulk formulas of Large and Yeager (2009), and a set of formulas to compute properties of moist air presented in Appendix B. The fluxes for evaluating the global ocean heat and freshwater balances were calculated on the $1^\circ \times 1^\circ$ grid of COBESST. As explained in Section 3.2.3, we impose exact closure on long-term mean global ocean averaged heat and freshwater fluxes in the satellite era. To achieve this, we adjusted the downward fluxes (i.e., the shortwave and longwave radiation and precipitation fluxes) by globally and temporally constant factors. These factors are applied for the entire dataset period.

After the main and additional adjustments, the long-term mean, global ocean averaged surface heat flux (2) retains some residuals (*res*):

$$Q_{SW} + Q_{DLW} + Q_{ULW} + Q_{LA} + Q_{SE} + Q_{P+E+R} + Q_{IO} = res, \tag{24}$$

where Q_X denotes the global ocean average for Q_X. In (24),

$$Q_{SW} \equiv \frac{\int_{ocean} \langle f_o Q_{DSW}(1-\alpha)\rangle dS}{\int_{ocean} dS} \tag{25}$$

is the long-term mean global ocean averaged net shortwave radiation flux determined by the downwelling shortwave radiation flux Q_{DSW} and albedo α, where $\langle\cdot\rangle$ means a long-term average, whose period will be determined shortly. Similarly, Q_{DLW} and Q_{ULW} are the downward and upward longwave radiation fluxes respectively, Q_{LA} is the latent heat flux, and Q_{SE} is the sensible heat flux. $Q_{P+E+R} \equiv \int_{ocean} \langle f_o Q_{P+E} + Q_R\rangle dS / \int_{ocean} dS \sim -0.4\mathrm{W\,m^{-2}}$ is the heat flux due to the incoming and outgoing freshwater fluxes of precipitation, evaporation, and runoff (all assumed to have the local sea-surface temperature), and $Q_{IO} \equiv \int_{ocean} \langle (1-f_o) Q_{IO}\rangle dS / \int_{ocean} dS \sim -1.4\mathrm{W\,m^{-2}}$ is the heat flux due to the sea-ice thermodynamics, all of which are taken from a previous interannual CORE simulation conducted at MRI. These figures are tentative and should be revised when an observational estimate or an ensemble mean of multi-model outputs becomes available.

The heat budget is closed by applying a common factor (a) to the downwelling shortwave and longwave radiative fluxes:

$$a(Q_{SW} + Q_{DLW}) + Q_{ULW} + Q_{LA} + Q_{SE} + Q_{P+E+R} + Q_{IO} = 0. \tag{26}$$

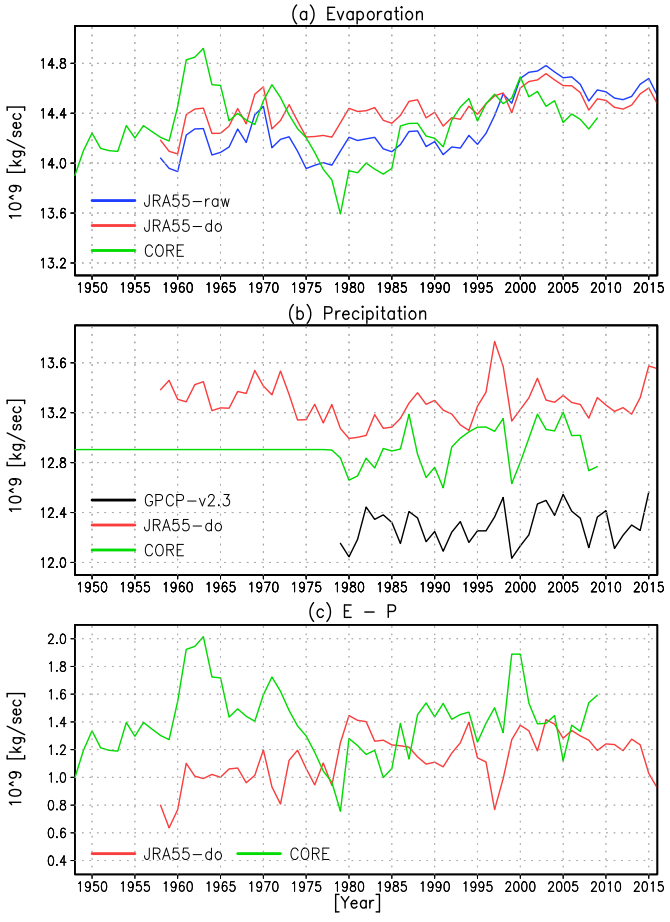

Fig. 23. Time-series of the annual mean global ocean-integrated (a) evaporation and (b) precipitation flux ($\times 10^9\,\mathrm{kg\,s^{-1}}$). Results are derived from three datasets; CORE inter-annual forcing version 2 (green), JRA55-raw (blue), and JRA55-do (red). The black line in (b) is the precipitation of GPGP v2.3. (c) Same as the upper panels, but for evaporation minus precipitation. Bulk formula and air-properties formulas are taken from Large and Yeager (2009) and Gill (1982), respectively. In JRA55-raw, the precipitation and the evaporation minus precipitation time-series were omitted because the precipitation was too high and out of range. (For interpretation of the references to colour in this figure legend, the reader is referred to the web version of this article.)

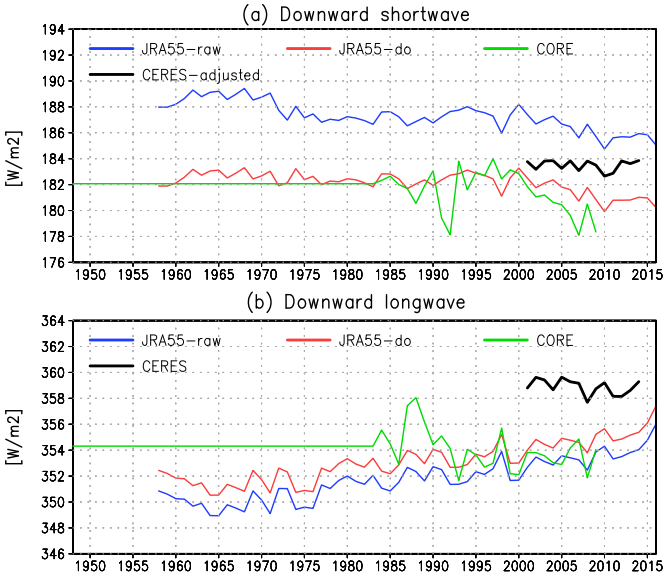

Fig. 24. Time-series of annual mean global ocean averaged (a) downward shortwave radiation and (b) downward longwave radiation ($\mathrm{W\,m^{-2}}$). Data are derived from (green) CORE, (blue) JRA55-raw, and (red) JRA55-do. Reference data (black lines) are the adjusted and unadjusted CERES-EBAF-Surface-Ed2.8 in (a) and (b), respectively. (For interpretation of the references to colour in this figure legend, the reader is referred to the web version of this article.)

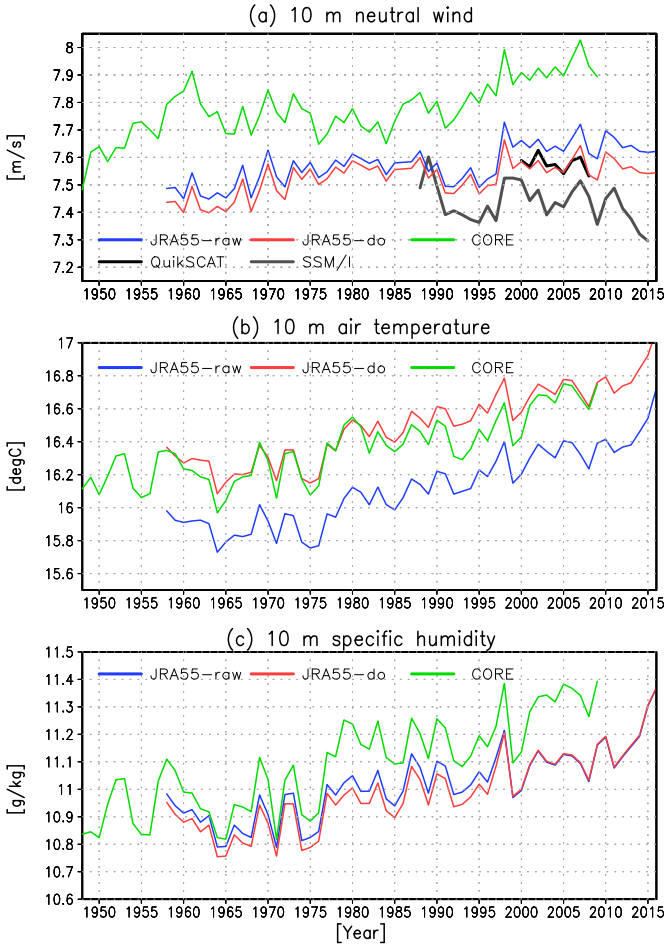

Fig. 25. Time-series of annual mean global ocean averaged surface data; (a) equivalent neutral wind speed ($m\,s^{-1}$), (b) air temperature (°C), (c) specific humidity at 10 m height ($g\,kg^{-1}$). Data are derived from (green) CORE, (blue) JRA55-raw, and (red) JRA55-do. Reference data in (a) are QuikSCAT (black line) and SSM/I wind speed (grey line). (For interpretation of the references to colour in this figure legend, the reader is referred to the web version of this article.)

Combining Eqs. (26) and (24), the factor a is calculated as

$$a = \frac{Q_{SW} + Q_{DLW} - res}{Q_{SW} + Q_{DLW}}. \tag{27}$$

The period to impose exact closure of the global ocean averaged surface fluxes is determined using an assessment of their time-series. Note that we will use common closure periods for heat and freshwater fluxes. Looking at the total heat flux of JRA55-do in advance, Fig. 22e implies that a minor "regime shift" remains in the total heat flux in the late 1990s even after the main and additional adjustments. This is largely caused by the shift in the latent heat flux or evaporation as seen in Figs. 22c and 23a. Details are discussed in the next section. To constrain a long-term budget, it is desirable to choose an interval that includes equal periods both before and after the regime shift. Therefore, we decided to take the period of 1988–2007, which covers the last and first 10 years of the adjustment phases II (1973–1997) and III (1998–present), respectively. The choice of 10 years is because there was an increasing trend of precipitation in the latter part of phase III that was presumably caused by the introduction of GNSS-RO into JRA-55 in 2006, as well as the increase in the number of radiance observations from satellite water vapor channels. Though the trend was mitigated by further dividing the adjustment phase III in the latest version, we still refrained from including this period for the computation of the exact closure. The residual heat flux (*res*) was $5.8 Wm^{-2}$ during the 1988–2007 period. For this period, Q_{SW} and Q_{DLW} were 167.9 Wm^{-2} and 345.7 Wm^{-2} respectively, giving $a = 0.98863$ (an approximate reduction of 1.1%).

To close the budget of the long-term mean global ocean averaged freshwater flux, we multiply the precipitation $\mathcal{P}$ by a factor b:

$$b\mathcal{P} + \mathcal{E} + \mathcal{R} + \mathcal{S} = 0, \tag{28}$$

where $\mathcal{S}$ is the long-term mean global ocean averaged sublimation over sea-ice ($\mathcal{S} \equiv \int_{ocean} \langle (1 - f_o) S \rangle dS / \int_{ocean} dS \sim -1.3 \times 10^{-7}\,kg\,m^{-2}\,s^{-1}$). Here, $\mathcal{S}$ is determined in a simulation forced by a preliminary version of the JRA55-do dataset and should be revised when an observational estimate or an ensemble mean of multi-model outputs becomes available. $\mathcal{E}$ and $\mathcal{R}$ represent the long-term mean global ocean averaged evaporation and runoff, respectively. The factor b is calculated as

$$b = -\frac{\mathcal{E} + \mathcal{R} + \mathcal{S}}{\mathcal{P}}. \tag{29}$$

Given the evaporation $\mathcal{E} = -3.971 \times 10^{-5}\,kg\,m^{-2}\,s^{-1}$, precipitation $\mathcal{P} = 3.565 \times 10^{-5}\,kg\,m^{-2}\,s^{-1}$, and river runoff $\mathcal{R} = 3.44 \times 10^{-6}\,kg\,m^{-2}\,s^{-1}$ over the 1988–2007 period, b was computed as 1.02118 (denoting an approximate enhancement of 2.1%).

6. Evaluation

This section compares the atmospheric fields and surface fluxes derived from the JRA55-do, CORE, and JRA55-raw datasets, and aims to motivate the replacement of CORE by JRA55-do in the OMIP framework. For this purpose, we focus on the large-scale features and global balances of the surface fluxes. We first interpolated the atmospheric fields on the 1° × 1° grid of COBESST, then calculated the heat and freshwater fluxes as described in the previous section. Note that COBESST is commonly used as the lower boundary condition for all of the three datasets in order to compare only the set of atmospheric variables. The wind speed and surface wind stress cannot be suitably computed using this approach because any temporal or spatial interpolation of the wind vector slightly weakens both variables, complicating the comparison with observations. Therefore, the equivalent neutral wind speeds and surface wind stresses in JRA55-do and JRA55-raw were computed on their original normal TL319 grid points, using their surface-atmospheric variables and JRA-55 brightness temperature, which is based on COBESST.

As a reference, a detailed comparison of surface meteorological variables with buoy observations is given in Appendix F. JRA55-do showed reduced RMS misfits and increased correlations in comparison with JRA55-raw and CORE. An atlas of annual mean surface fluxes of JRA55-do and their comparison with the CORE dataset is given in Appendix G. Several notable features have also been described there.

6.1. Time-series of the global mean

The downward shortwave and longwave radiations (Fig. 24), precipitation (Fig. 23b), and the surface marine meteorological variables (air temperature, specific humidity, and wind speed; Fig. 25) for the three sets of surface-atmospheric data were averaged over the global ocean (over 60°S–60°N for wind speed) and are depicted as time-series.

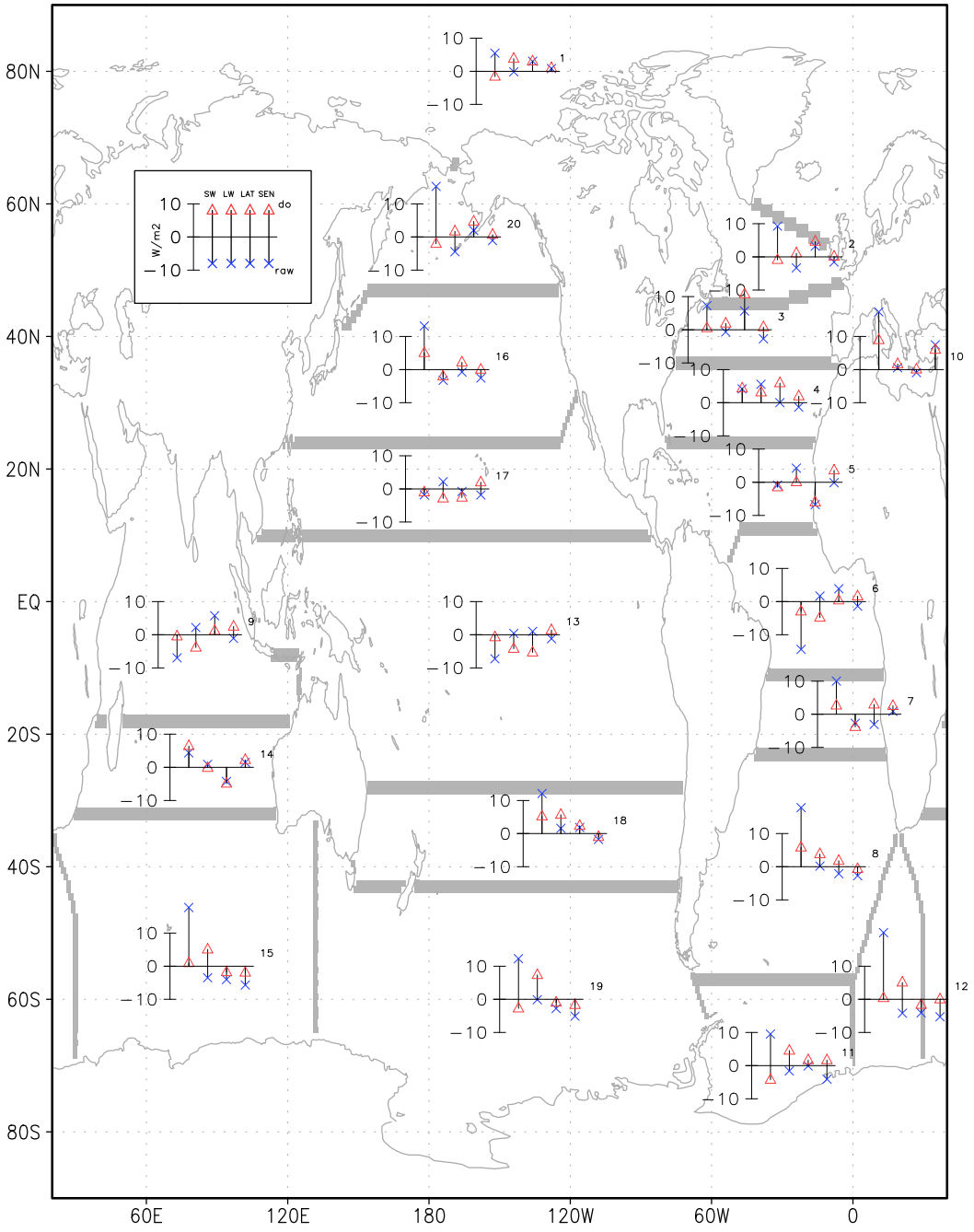

Fig. 26. Regional comparison of the mean (1988–2007) heat flux components (from the left, net shortwave radiation, net longwave radiation, latent heat, and sensible heat fluxes). Blue crosses and red triangles depict the differences of JRA55-raw and JRA55-do, respectively, from the CORE inter-annual forcing version 2. Positive fluxes are directed into the ocean. The units are W m^{-2}. (For interpretation of the references to colour in this figure legend, the reader is referred to the web version of this article.)

The time-dependent adjustment applied to JRA55-raw caused no apparent spurious behaviour in the time series of global means in JRA55-do, but it did correct the abrupt reduction of shortwave radiation in the 1973 data of JRA55-raw (Fig. 24a). After 2000, the radiation fields of JRA55-raw and JRA55-do well reproduced the inter-annual or year-to-year variability of adjusted CERES shortwave and unadjusted CERES longwave radiation (Fig. 24), although there is an offset between JRA55-do radiation and CERES due to the global-balance adjustment explained in Section 5. The increased precipitation in JRA55-raw during the late 1990s (Fig. 1b) is suppressed in JRA55-do (Fig. 23b). However, the inter-annual precipitation variability in JRA55-do somewhat deviates from that in GPCP. The abrupt increase of the surface winds around the late 1990s in JRA55-raw is alleviated in JRA55-do (Fig. 25a). The inter-annual variation of air temperature and

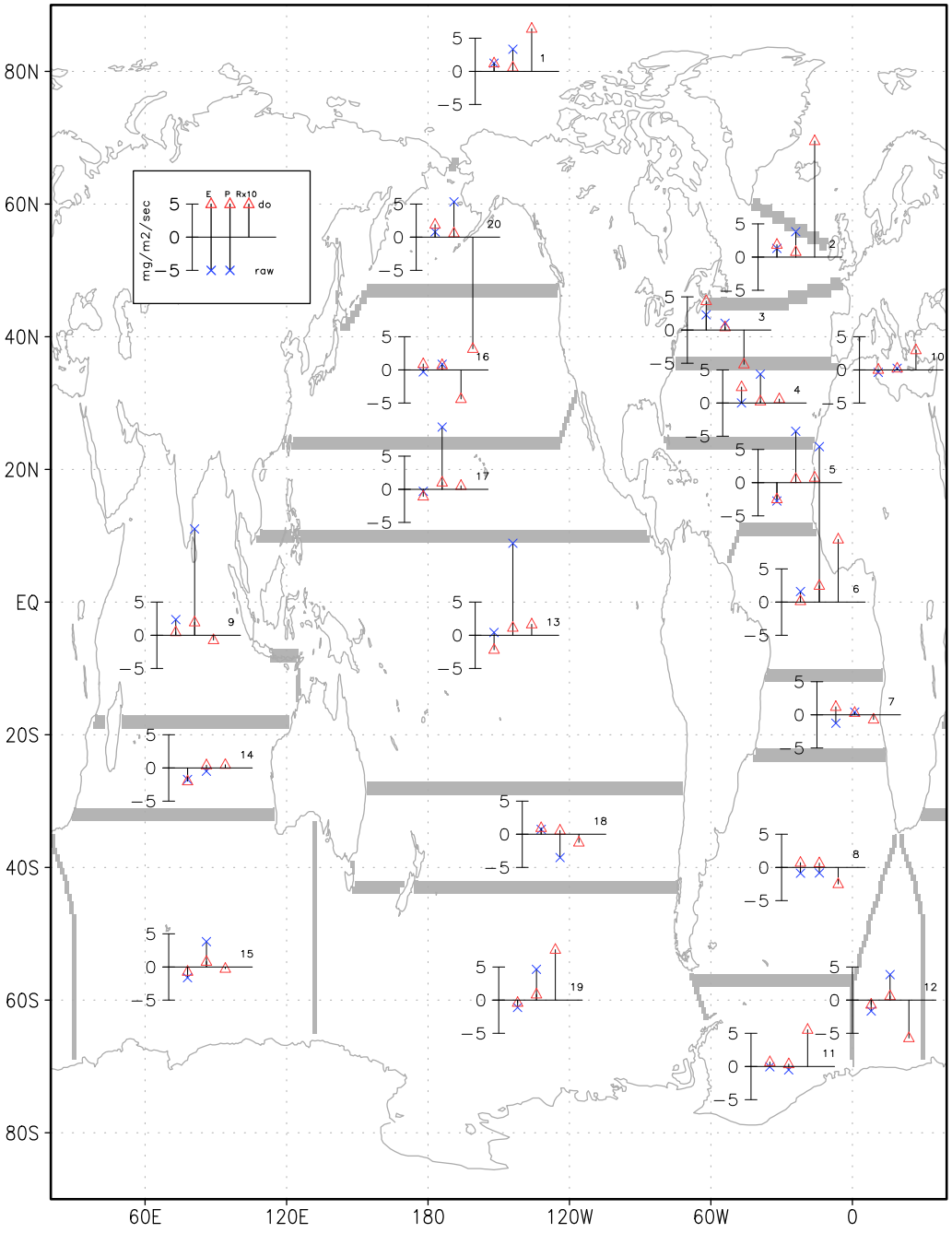

Fig. 27. Same as Fig. 26 but for the mean (1988–2007) freshwater flux components (evaporation, precipitation, and runoff). Positive fluxes are directed into the ocean. The units are mg m^{-2} s^{-1}. Note that the runoff values are multiplied by ten.

specific humidity largely follows that of CORE (Fig. 25b and c), although the specific humidity is lower in JRA55-do than in CORE, implying that the majority of reanalysis products have lower relative humidity than CORE.

6.2. Global heat and freshwater flux

Figs. 22 and 23 plot the time series of the annual mean global ocean averaged heat fluxes and the annual mean global ocean-integrated freshwater fluxes, respectively. In general, the heat flux components of JRA55-do better resemble the CORE components than those of JRA55-raw. Specifically, the total heat flux in JRA55-raw was considerably decreased (by ~ 5 Wm^{-2}) during the late 1990s. At that time, the increased wind speed and the suppression of the increasing specific humidity trend (Fig. 25a and c) artificially enhanced the evaporation. This effect was mitigated in JRA55-do. Specifically, the overall wind speed increase from the 1990s to the 2000s is much less in JRA55-do, which would reduce the evaporation change; meanwhile, the humidity

Table 9
Global mean air - sea fluxes over the 1988–2007 and 1958–2009 period. The units of the (mean) heat fluxes and the (integrated) freshwater fluxes are $W\,m^{-2}$ and $10^9\,kg\,s^{-1}$ (~ Sverdrups), respectively. Positive fluxes are directed into the ocean. Fluxes computed for four combinations of atmospheric and sea-surface temperature (SST) and sea-ice concentration (SIC) datasets are presented. The first three columns present fluxes based on the CORE, JRA55-raw, and JRA55-do datasets with COBESST (Ishii et al., 2005) as the lower boundary condition. The last column presents fluxes based on the JRA55-do dataset with the dataset by Hurrell et al. (2008) as the lower boundary condition. The period 1988–2007 is used to impose the complete closure. The period 1958–2009 is the full overlapping period of CORE and JRA-55.

Atmospheric dataset	CORE		JRA55-raw		JRA55-do		JRA55-do	
SST and SIC dataset	COBESST		COBESST		COBESST		Hurrell-SST	
Averaging period	88–07	58–09	88–07	58–09	88–07	58–09	88–07	58–09
Net shortwave	165.3	165.4	169.9	170.1	166.0	166.0	166.0	165.9
Net longwave	−53.7	−52.6	−53.7	−53.9	−53.4	−53.5	−53.4	−53.5
Latent heat flux	−96.6	−96.1	−96.7	−95.6	−97.2	−96.6	−97.4	−96.6
Sensible heat flux	−14.4	−14.1	−16.3	−16.5	−13.6	−13.7	−13.8	−13.9
Residual heat flux[a]	0.6	2.5	3.1	4.1	1.8	2.2	1.4	1.9
Evaporation	−14.4	−14.3	−14.4	−14.3	−14.5	−14.4	−14.5	−14.4
Precipitation	13.0	12.9	15.5	15.2	13.3	13.3	13.3	13.3
Residual freshwater flux[b]	−1.5	−1.4	1.0	1.0	−1.2	−1.1	−1.2	−1.1

[a] Sum of net shortwave, net longwave, latent heat flux, and sensible heat flux. This should balance with heat flux due to sea-ice thermodynamics ~ $-1.4\,W\,m^{-2}$ and the difference in water temperature of precipitation, evaporation, and runoff ~ $-0.4\,W\,m^{-2}$, both are taken from a global model simulation of MRI.

[b] Sum of evaporation and precipitation. This should balance with river discharge (~ $1.26 \times 10^9\,kg\,s^{-1}$ from this dataset) and sublimation over sea-ice (~ $-0.05 \times 10^9\,kg\,s^{-1}$ from a global model simulation of MRI).

Table 10
Regional climatological air - sea heat fluxes ($W\,m^{-2}$) and freshwater fluxes ($mg\,m^{-2}\,s^{-1}$) over a 20-year period (1988–2007). Upper (no parentheses) and lower (in parentheses) values derive from the JRA55-do and CORE datasets, respectively. Positive fluxes are directed into the ocean. The regions are shown in Figs. 26 and 27.

region	f_oQ_{AO}	f_oQ_{SW}	f_oQ_{LW}	f_oQ_{LA}	f_oQ_{SE}	f_oF_{AO}	f_oE	P	R
1	−31	40	−25	−26	−20	16	−11	16	11
	(−37)	(42)	(−29)	(−30)	(−21)	(13)	(−12)	(15)	(10)
2	−25	86	−39	−47	−25	22	−19	31	10
	(−30)	(87)	(−40)	(−52)	(−25)	(18)	(−21)	(30)	(8)
3	−28	150	−58	−99	−22	4	−40	42	2
	(−42)	(150)	(−60)	(−110)	(−22)	(0)	(−45)	(42)	(3)
4	−4	197	−68	−120	−13	−20	−49	29	0
	(−19)	(193)	(−71)	(−126)	(−15)	(−23)	(−52)	(29)	(0)
5	4	216	−63	−139	−9	−23	−57	26	8
	(8)	(217)	(−63)	(−133)	(−13)	(−21)	(−55)	(25)	(8)
6	33	214	−56	−117	−8	19	−48	42	25
	(39)	(217)	(−52)	(−117)	(−10)	(15)	(−48)	(39)	(24)
7	24	213	−59	−120	−10	−40	−49	8	1
	(19)	(211)	(−55)	(−123)	(−13)	(−42)	(−50)	(8)	(1)
8	15	154	−54	−73	−12	5	−30	33	2
	(5)	(148)	(−58)	(−75)	(−11)	(4)	(−30)	32	(2)
9	8	217	−63	−137	−9	−4	−56	49	4
	(9)	(218)	(−59)	(−139)	(−12)	(−6)	(−57)	(47)	(4)
10	−8	190	−80	−103	−15	−19	−42	17	6
	(−25)	(181)	(−81)	(−104)	(−21)	(−20)	(−41)	(17)	(5)
11	−2	44	−19	−14	−13	17	−6	20	3
	(−5)	(48)	(−24)	(−16)	(−15)	(15)	(−6)	(19)	(2)
12	0	85	−33	−38	−14	11	−15	26	1
	(−4)	(85)	(−38)	(−37)	(−14)	(12)	(−15)	(25)	(1)
13	17	214	−59	−128	−10	0	−52	50	2
	(26)	(215)	(−55)	(−122)	(−12)	(0)	(−50)	(49)	(1)
14	−17	211	−67	−145	−16	−38	−59	21	1
	(−21)	(204)	(−67)	(−140)	(−18)	(−36)	(−57)	(20)	(1)
15	0	119	−44	−61	−15	6	−25	30	1
	(−3)	(118)	(−49)	(−59)	(−13)	(6)	(−24)	(29)	(1)
16	−15	160	−57	−100	−19	4	−41	42	3
	(−20)	(155)	(−55)	(−102)	(−19)	(3)	(−41)	(42)	(3)
17	−1	209	−60	−139	−11	−15	−57	41	1
	(4)	(210)	(−57)	(−136)	(−13)	(−15)	(−56)	(40)	(1)
18	2	170	−59	−93	−15	2	−38	39	0
	(−10)	(164)	(−65)	(−95)	(−14)	(0)	(−39)	39	(0)
19	−5	92	−38	−43	−16	12	−17	27	2
	(−7)	(95)	(−46)	(−42)	(−14)	(11)	(−17)	(27)	(1)
20	−10	95	−45	−39	−22	21	−15	32	4
	(−15)	(97)	(−46)	(−43)	(−22)	(20)	(−17)	(32)	(6)

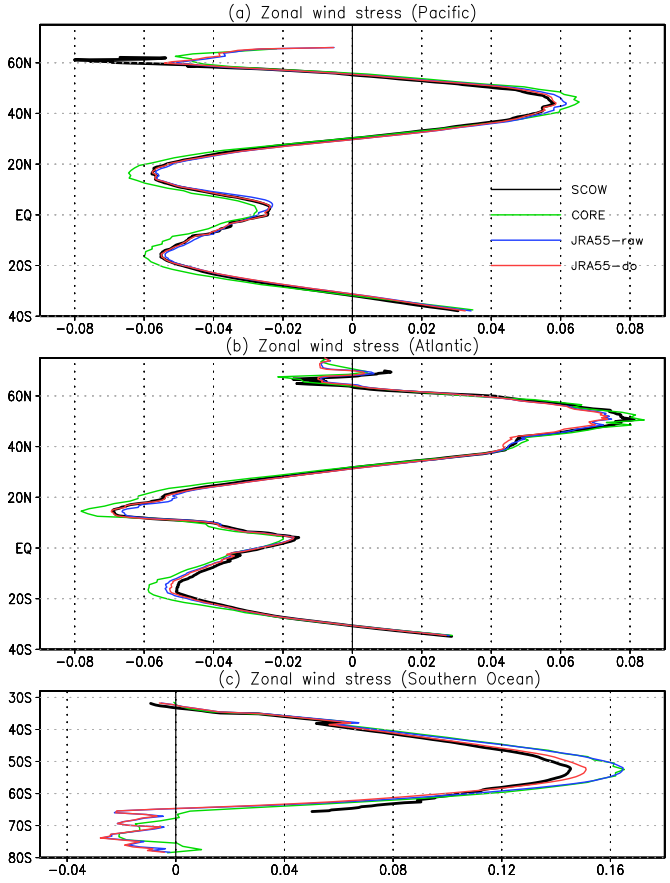

Fig. 28. Comparison of mean (Nov 1999–Oct 2009) basin-wide averaged zonal wind-stress ($N\,m^{-2}$) in (red) JRA55-do, (blue) JRA55-raw, and (green) CORE. The black lines plot the Scatterometer Oceanic Wind Stress (SCOW) data of Risien and Chelton (2008). SCOW is the climatology based on September 1999–October 2009 of QuikSCAT. (For interpretation of the references to colour in this figure legend, the reader is referred to the web version of this article.)

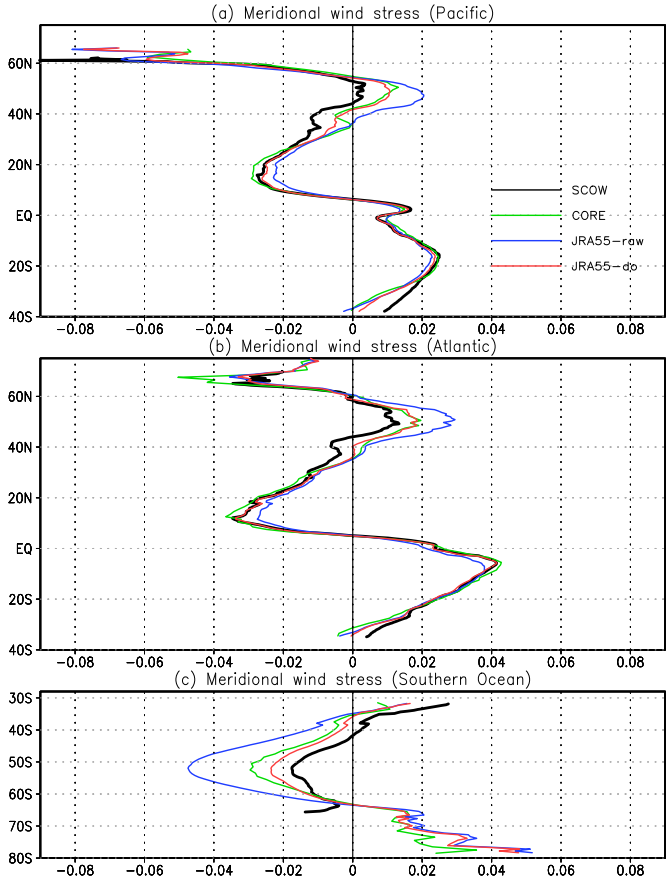

Fig. 29. Same as Fig. 28 but for the meridional wind-stress.

increase between these periods is slightly larger in JRA55-do than in JRA55-raw, which would also act to reduce the evaporation and latent heat flux change.

There are some notable differences between the JRA55-do and CORE analyses. The time series of longwave radiation and sensible heat fluxes are steadier in JRA55-raw and JRA55-do than in CORE. The large decadal variations in latent and sensible heat fluxes seen in CORE during the 1970s and 1980s are not seen in JRA55-do. The lower boundary condition is COBESST in JRA-55, but another SST dataset is used in the NCEP/NCAR reanalysis and the ISCCP-FD longwave radiation calculation. In general, the surface air temperature is strongly influenced by the SST used as the lower boundary condition. Therefore, we may expect less variability in the difference between surface air temperature and SST in JRA-55 than CORE in the present flux computation, which commonly uses COBESST as the lower boundary condition. Our assessment on the JRA-55 downward longwave radiation at the sea-surface implies that the interannual variation of the downward longwave radiation correlated well with that of the surface air temperature, which is influenced by the SST (i.e., COBESST). Therefore, we may generally expect less variability in the difference between upward and downward longwave radiation fluxes in JRA-55 than in CORE if COBESST is used as the lower boundary condition. However, the use of another SST dataset (Hurrell et al., 2008) as the lower boundary condition only slightly enhanced variability (grey lines in Fig. 22). This would imply that the surface air temperature of JRA-55 follows more closely the variation of the SST than that of CORE. A detailed analysis on the boundary layer scheme of the atmospheric model used by JRA-55 would be required to resolve this issue, which is beyond the scope of this paper. It should also be noted that the effects of the Pinatubo volcanic eruption in 1991 represented as the decline of the downward shortwave radiation flux in CORE are missing from the radiative fluxes of JRA-55 (Fig. 24a). However, the simulated fields forced by JRA55-do might be cooled by the reduced air temperature assimilated into JRA-55 in the 1991–92 period (see Fig. 25b).

The long-term (1988–2007) averages of the three datasets are summarised in Table 9. In JRA55-do, the net fluxes of shortwave radiation ($166.0\mathrm{Wm}^{-2}$), longwave radiation ($-53.4\mathrm{Wm}^{-2}$), latent heat ($-97.2\mathrm{Wm}^{-2}$), and sensible heat ($-13.6\mathrm{Wm}^{-2}$) sum to $1.8\mathrm{Wm}^{-2}$, which exactly compensates the sum of Q_{P+E+R} and Q_{IO} ($-1.8\mathrm{Wm}^{-2}$), implying that the closure in Section 5 worked as intended. The long-term (1988–2007) average of the difference between evaporation ($14.51 \times 10^9\,\mathrm{kg\,s}^{-1}$) and precipitation ($13.30 \times 10^9\,\mathrm{kg\,s}^{-1}$) is $1.21 \times 10^9\,\mathrm{kg\,s}^{-1}$, which can account for the difference between the river runoff ($1.26 \times 10^9\,\mathrm{kg\,s}^{-1}$) and sublimation ($0.05 \times 10^9\,\mathrm{kg\,s}^{-1}$).

Table 9 also lists the averages of heat and fresh water flux components for the overlapping period (1958–2009) of CORE and JRA-55. The differences for JRA55-do between 1958–2009 and 1988–2007 are less than $1\mathrm{W\,m}^{-2}$ for heat fluxes and $0.1 \times 10^9\,\mathrm{kg\,s}^{-1}$ for fresh water fluxes. These differences are less than or equal to those between datasets (JRA55-do and CORE). As a result, it can be concluded that the constraints imposed on the surface heat and freshwater flux, specifically that the long-term mean globally averaged heat flux and globally integrated freshwater flux into the ocean–sea-ice system are both nearly zero or slightly positive, approximately hold for the entire dataset period for JRA55-do within the accuracy range of the major components of surface heat ($\sim 0 - 1\,\mathrm{W\,m}^{-2}$) and freshwater ($\sim 0 - 1 \times 10^8\,\mathrm{kg\,s}^{-1}$) flux budgets.

6.3. Regional comparison of flux components

Following Large and Yeager (2009), we divided the oceanic domain into almost identical regions. The components of the heat and freshwater fluxes are regionally compared for the period 1988–2007 in Figs. 26 and 27, respectively, and their values in JRA55-do and CORE are presented in Table 10. In general, the heat flux components differ by less than $\pm\,5\,\mathrm{W\,m}^{-2}$ and the freshwater flux components are consistent within a few $\mathrm{mgm}^{-2}\mathrm{s}^{-1}$. JRA55-do is more consistent with CORE than JRA55-raw, specifically in the low-latitude downwelling shortwave radiation and precipitation. This implies that the adjustments are successful overall. It should be noted that JRA55-do tends to put more freshwater into the northern North Atlantic (Regions 2 and 3) than CORE. This is contributed by the smaller evaporation and the larger runoff from Greenland in JRA55-do. Impact of this feature on the North Atlantic meridional overturning in simulations should be investigated in future works.

Figs. 28 and 29 compare the basin-wide zonal means of the wind stress components in JRA55-do, JRA55-raw, and CORE. In general, the wind stress of JRA55-do best matches the Scatterometer Oceanic Wind Stress product (SCOW) provided by Risien and Chelton (2008). The exception is the slightly weak eastward wind stress in the latitude band of the mid-latitude westerly wind of the North Atlantic (Fig. 28b). This weakening presumably arises from the low-resolution SST (COBESST), which is adopted as the lower boundary condition in the wind-stress computation of JRA55-do. At mid-latitudes, the atmospheric stability and bulk transfer coefficients are strongly sensitive to the location and strength of the oceanic fronts and eddies. The strength of the SST fronts measured by the SST gradient is stronger in the North Atlantic than that of the North Pacific. This makes the resolution issue more critical for the North Atlantic (see also Fig. 36). Additionally, the horizontal

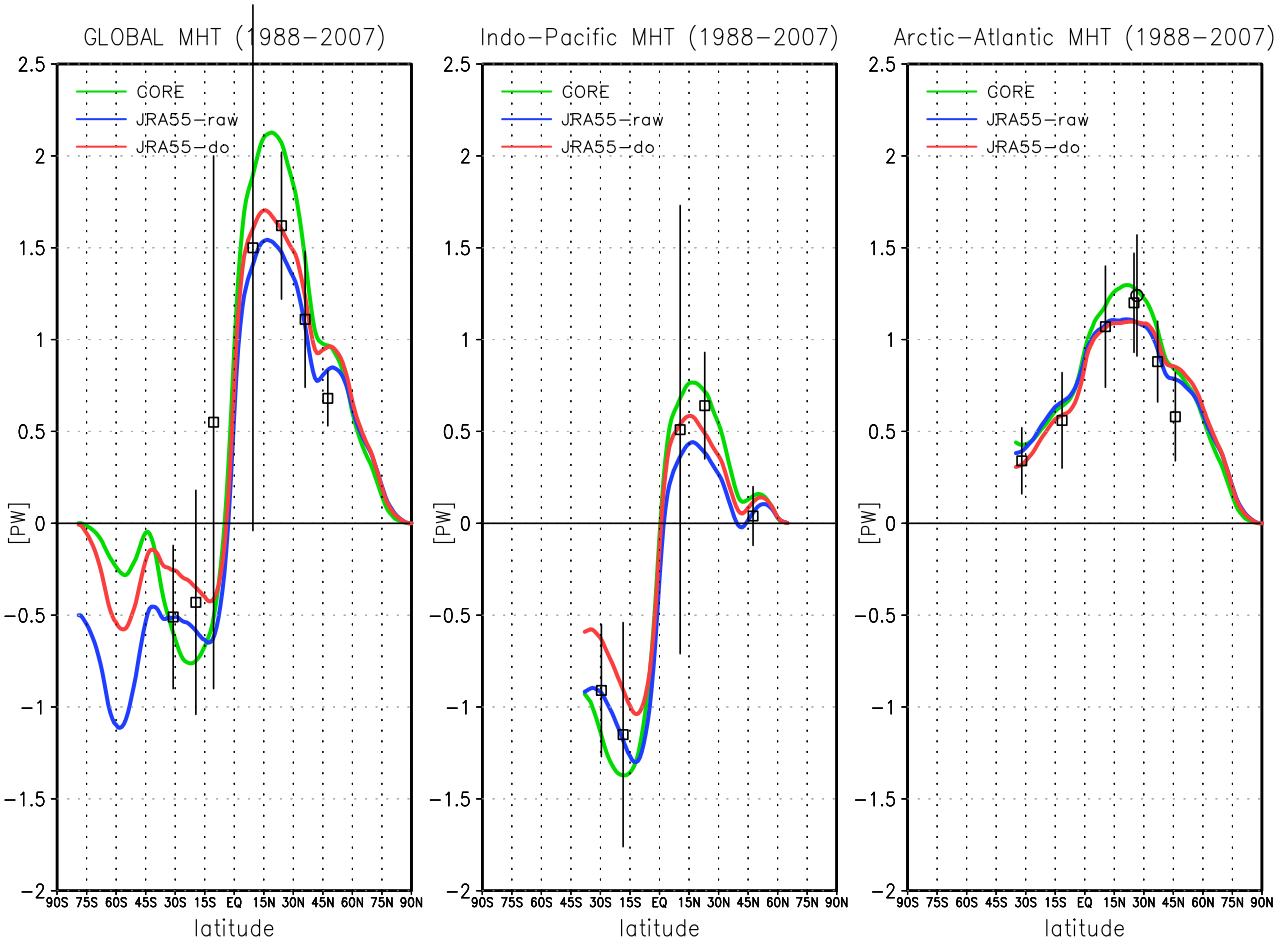

Fig. 30. Implied meridional heat transports (PW = 10^{15}Wm^{-2}) derived from CORE inter-annual forcing version 2 (green), JRA55-raw (blue), and JRA55-do (red). The rectangular plots are estimated from the observations and assimilations compiled by Macdonald and Baringer (2013). The open circle at 26.5°N in the Atlantic is an updated estimation from RAPID transport array reported by McDonagh et al. (2015). (For interpretation of the references to colour in this figure legend, the reader is referred to the web version of this article.)

interpolation of the QuikSCAT wind vector onto the TL319 grid of JRA-55 in the suite of the adjustment operations may lead to the reduction of JRA55-do wind stresses. Regarding the meridional wind stress, JRA55-do shows improvement relative to both JRA55-raw and CORE, but there still remains differences from SCOW.

6.4. Implied meridional heat and freshwater transports

The implied oceanic meridional heat transport is typically calculated as follows:

$$\mathcal{MHT}(\phi) = \int_{\pi/2}^{\phi} \left(\int_0^{2\pi} \delta(\lambda, \phi) Q(\lambda, \phi) r \cos\phi d\lambda \right) r d\phi', \tag{30}$$

where $\delta(\lambda, \phi)$ is a digital mask that includes only the target basin, Q is defined by (2) and is positive into the ocean, r is the radius of the Earth, and λ and ϕ are the longitude and latitude respectively, expressed in radians. The implied meridional freshwater transport in the ocean–sea-ice system is calculated as follows:

$$\mathcal{MFT}(\phi) = \int_{\pi/2}^{\phi} \left(\int_0^{2\pi} \delta(\lambda, \phi) F_{ocean+ice}(\lambda, \phi) r \cos\phi d\lambda \right) r d\phi', \tag{31}$$

where $F_{ocean+ice}$ is defined by (4).

The transports in CORE and JRA55-do were computed by slightly different methods. In CORE, the implied meridional heat transport was computed with zero ice-ocean flux Q_{IO} and zero material transport by the freshwater fluxes Q_{P+E} and Q_R. We instead applied the corrections described by Large and Yeager (2009). Following their computation of the meridional heat transport (Fig. 10a of Large and Yeager (2009)), the global heat flux imbalance of 0.6 W m^{-2} in CORE (Table 9) was assumed to be uniformly distributed except in the Atlantic Ocean. The exclusion of the Atlantic Ocean was based on the assumption that there was no bias and oceanic heat storage in the Atlantic basin, which gave the most consistent results with the estimated oceanic heat transports for the CORE datasets as explained by Large and Yeager (2009). Thus, we subtracted $0.8\text{Wm}^{-2}(\sim 0.6\text{Wm}^{-2} \times A_{\text{GlobalOcean}}/[A_{\text{GlobalOcean}} - A_{\text{AtlanticOcean}}]$, where A represents horizontal area) from the total heat flux Q in (30) in all oceanic regions except the Atlantic Ocean. To compute the meridional heat transport in JRA55-do, we added the 2D distributions of both the ice - ocean heat flux ($(1 - f_o)Q_{IO}$) and the heat flux due to precipitation, evaporation, and runoff (assumed to have the local SST) ($f_o Q_{P+E} + Q_R$) to the total heat flux. The values are taken from a previous interannual CORE simulation conducted at MRI.

When computing the implied meridional freshwater transport in

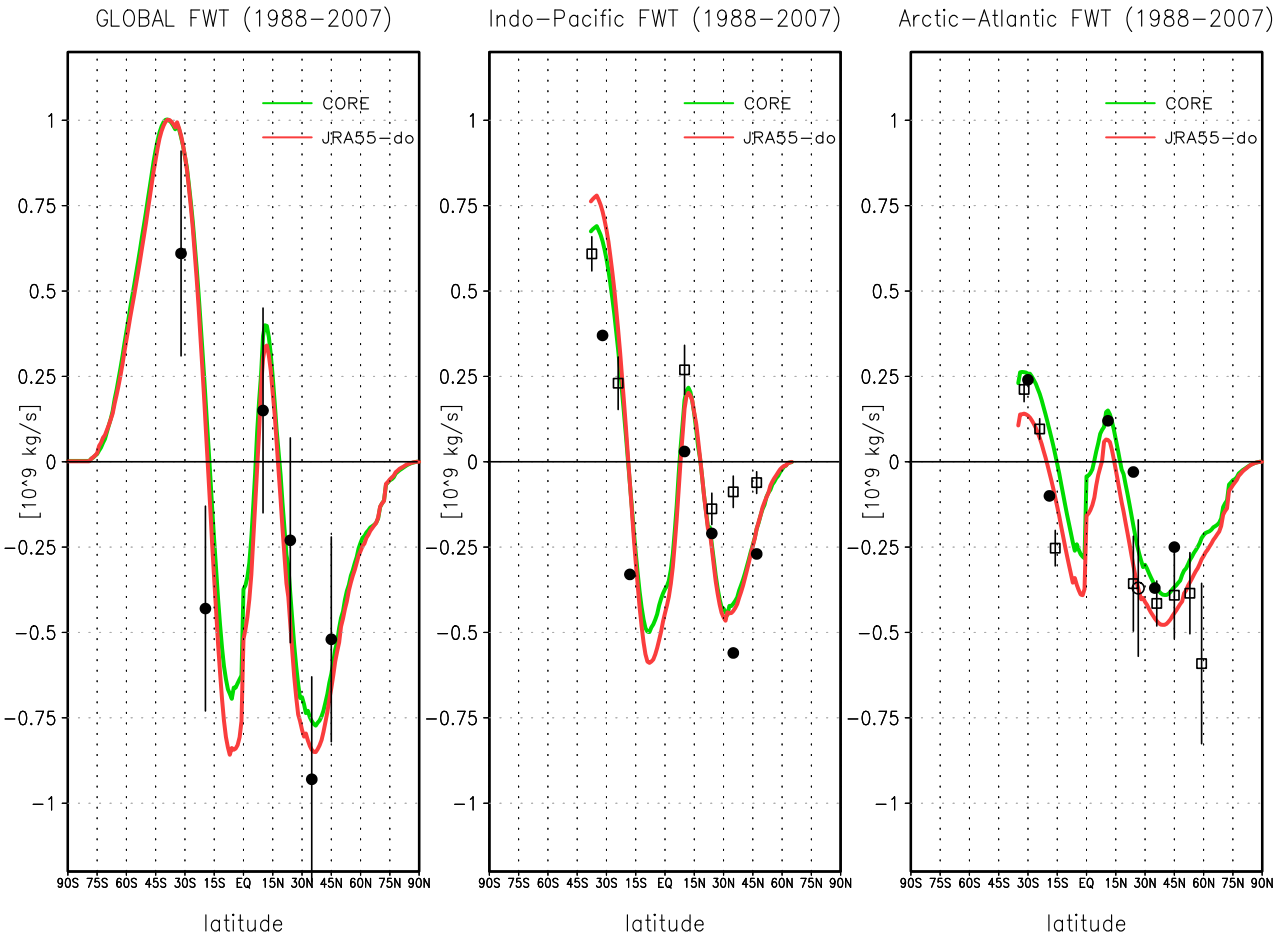

Fig. 31. Implied meridional freshwater transports ($\times 10^9\,\mathrm{kg\,s^{-1}}$) derived from CORE inter-annual forcing version 2 (green) and JRA55-do (red). JRA55-raw was omitted because the precipitation was too high and out of range. Direct estimates based on hydrographic observations compiled by Talley (2008) (rectangles) and Wijffels (2001) (closed circles) are also depicted. Talley (2008) reported only basin-wise estimations with error bars. The error bars ($\pm\ 0.30 \times 10^9\,\mathrm{kg\,s^{-1}}$) added to Wijffels' (2001) estimates of the global freshwater transport are based on a scaling analysis. The open circle at 26.5°N in the Atlantic is an updated estimation from RAPID transport array reported by McDonagh et al. (2015). (For interpretation of the references to colour in this figure legend, the reader is referred to the web version of this article.)

JRA55-do, we considered the 2D distribution of the sublimation over sea-ice ($(1 - f_o)S$) in the total freshwater flux. The values were obtained by simulating with a preliminary version of the JRA55-do dataset, which is also used to compute the precipitation adjustment factor for achieving global balance in Section 5. The CORE computation of the implied meridional freshwater transport ignored the sublimation effects. Instead, the global imbalance of the CORE dataset ($\mathcal{P} + \mathcal{E} + \mathcal{R} = -6.4 \times 10^{-7}\,\mathrm{kg\,m^{-2}\,s^{-1}}$, where $\mathcal{P} = 3.547 \times 10^{-5}\,\mathrm{kg\,m^{-2}\,s^{-1}}$, $\mathcal{E} = -3.946 \times 10^{-5}\,\mathrm{kg\,m^{-2}\,s^{-1}}$, and $\mathcal{R} = 3.35 \times 10^{-6}\,\mathrm{kg\,m^{-2}\,s^{-1}}$, taking the oceanic area as $3.654 \times 10^{14}\,\mathrm{m^2}$) is compensated uniformly over the oceans (including the Atlantic Ocean).

The $\mathcal{MHT}$ and $\mathcal{MFT}$ are depicted in Figs. 30 and 31, respectively. The meridional heat and freshwater transports are comparable in CORE and JRA55-do, and largely fit within the error bars of the observational estimates (Macdonald and Baringer 2013; Wijffels 2001; Talley 2008; McDonagh et al. 2015). A notable difference is the peaks of poleward heat transport appearing at low latitudes. These peaks are smaller in JRA55-do than in CORE, because the net heat loss in JRA55-do is reduced in the mid-latitudes of the northern hemisphere and enhanced (denoting lower heat gain) in the tropics, relative to CORE (Fig. 32). In JRA55-do, less latent heat is lost to the atmosphere in the mid- to high-latitude North Atlantic Ocean, while more latent heat and net longwave fluxes are lost to the atmosphere in the tropical Indian and Pacific oceans (for confirmation, see the regional comparison in Fig. 26 and also Appendix G).

7. Summary and conclusions

In this paper, we revisited the scientific and engineering foundations required to produce surface forcing datasets for driving coupled ocean–sea-ice models, and in so doing we produced the JRA55-do dataset of use within the CORE/OMIP framework. When generating the JRA55-do forcing dataset, we followed the methods of Large and Yeager (2009) and advanced several aspects of their methods by utilising newly available datasets and considering feedback from the ocean modelling community.

In the CORE dataset provided by Large and Yeager (2009), the surface-atmospheric variables (e.g., air temperature and specific humidity, wind vectors, and sea level pressure) are based on the NCEP/NCAR reanalysis (Kalnay et al. 1996; Kistler et al. 2001), whereas the downward fluxes affected by clouds (e.g., radiative fluxes and precipitation) are based on other sources such as satellite data and direct observations. Our new JRA55-do dataset is based on a recent long-term (more than 50 years) reanalysis projects, the JRA-55 project, which

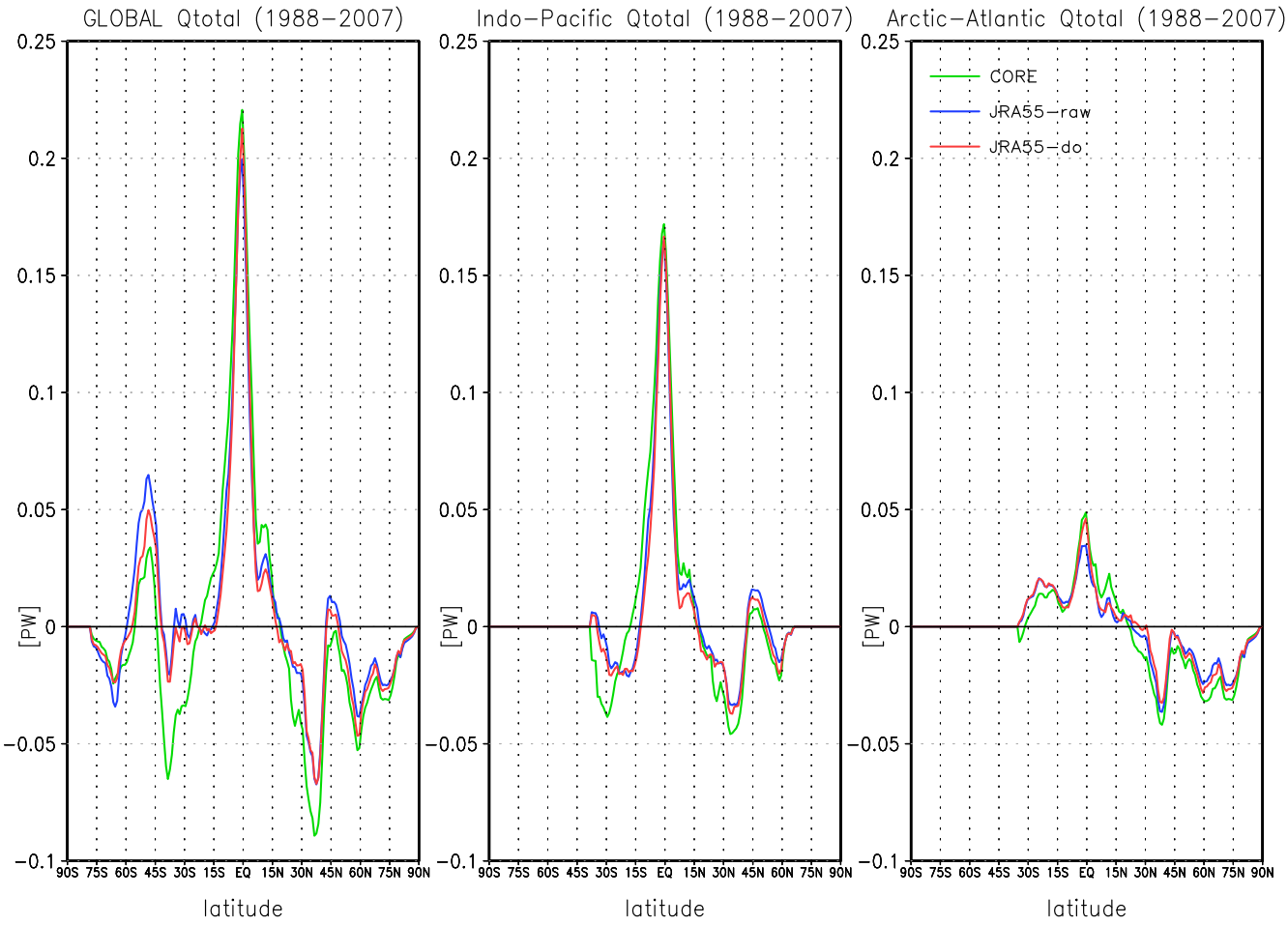

Fig. 32. Basin-wide integrated total surface heat fluxes (PW = 10^{15} W m^{-2}) derived from CORE inter-annual forcing version 2 (green), JRA55-raw (blue), and JRA55-do (red). (For interpretation of the references to colour in this figure legend, the reader is referred to the web version of this article.)

uses an atmospheric model with refined horizontal resolution (~ 55 km) and state-of-the-art data-assimilation techniques such as 4D-Var (Kobayashi et al., 2015). The atmospheric variables are based on the forecast phase of JRA-55 and the temporal interval (3 h) can marginally resolve the diurnal cycle, further advancing JRA55-do over the CORE dataset.

Besides applying the JRA-55 reanalysis product, we made several updates to the data production process. We retained QuikSCAT as the reference dataset for the wind-field adjustment and used the full ten years available. We also used the SSM/I wind speed product to cover the pre-QuikSCAT period 1988–1998. The air temperature and specific humidity were adjusted using the ensemble means of 7 atmospheric products. This averaging suppresses the appearance of isolated adjustment factors caused by the impact of locally over-constrained analysis fields on the reference data (Josey et al., 2014). Such effects could appear around isolated field observations such as tropical arrays and other station data (even on land). By the ensemble mean approach, we also mitigated the impact of the locally confined systematic biases in the individual products.

For cloud-affected fluxes, such as the downward radiative fluxes and precipitation, we use the reanalysis outputs and adjust them relative to the reference fields, thus facilitating data updates in near real-time. Moreover, the synoptic variabilities of the surface-atmospheric variables are more self-contained and mutually consistent than the earlier dataset. We also possess the inter-annual variations in the pre-satellite era (before the 1980s), which are absent in the CORE dataset. As references, we adopt CERES-EBAF-Surface_Ed2.8 for the shortwave and longwave radiation fluxes, and CORE for the precipitation. The CERES shortwave radiation data were slightly reduced in the tropics as well as over sea-ice before being applied as the reference field.

A state-of-the-art atmospheric reanalysis product still necessitates the introduction of adjustment factors. Specifically, changes in the observing system and the input data density and quality cause transitions in the quality of the assimilation product, which manifest as abrupt shifts in the JRA-55 data quality. To remove these shifts requires time-dependent adjustments. Fortunately, these adjustments can be calculated with some fidelity, because the JRA-55C dataset was acquired by the same data-assimilation system as JRA-55 but contains only the conventional surface and upper air observations (i.e., contains no satellite observations). Therefore, the biases in the pre-satellite period can be estimated from JRA-55C data in recent years. Although the inter-annual variability of the adjusted fields raises concern, the adjustment factors used in the pre-satellite and satellite periods are qualitatively similar. Furthermore, the time-dependent adjustments introduce no artificial transitions in the time series of the global means (Figs. 24 and 25). These findings guarantee consistency in the quality of large-scale climatological features over the entire dataset period.

To complete the dataset, we imported independent river runoff datasets. The river runoff is determined by a river-routing model (CaMa-Flood) forced by input runoff from the land-surface component of JRA-55 (Suzuki et al., 2017). The input is adjusted to ensure similar long-term variabilities in JRA55-do and the CORE dataset based on Dai et al. (2009). The river runoffs from Greenland and Antarctica,

which involve ice-sheets, are taken from Bamber et al. (2012) and Depoorter et al. (2013), respectively. The dataset details are summarised in Appendix C. We plan to regularly update the JRA55-do dataset thus facilitating real-time numerical experiments.

Other global surface datasets with similar features are based either on satellite data (HOAPS; Andersson et al. 2010 and J-OFURO; Tomita et al. 2010) or the synthesis of several sources (OAflux; Yu and Weller 2007). It is important to understand that the purposes and merits of these datasets differ from those of the datasets customised for driving ocean–sea-ice models. The former datasets tend to provide realistic fluxes, yet omit regions of large uncertainty or non-availability of observations. The area covered by sea-ice is a typical example of such regions. This treatment is unsuitable for driving global ocean–sea-ice models. When compiling a dataset for ocean–sea-ice models, an atmospheric reanalysis (which omits no region) is a suitable starting point. However, by adopting this approach we inevitably compromise the data accuracy which in turn requires careful assessments and corrections.

The JRA-55 project uses a relatively low-resolution SST dataset (COBESST) as the lower boundary condition. This approach causes concerns that the JRA-55 based products are not appropriate for forcing mesoscale eddy permitting models. A number of groups are currently investigating the topic of how to force ocean models in a mesoscale resolving regime and it is not obvious that we should use atmospheric reanalysis fields based on a high-resolution SST product. One issue concerns the potential for double-counting or mismatching of fluxes if the reanalysis product already contains the response to observed ocean eddies (such as the response of wind speed or air temperature), but in a different location to the ocean model. Another point of concern is that if a high-resolution ocean model feeds SST and surface ocean currents into the bulk fluxes (as is usual), then the air-sea fluxes will show detailed structure, e.g. in western boundary currents. For these reasons, there is some justification for using a smooth SST product until we better understand how to use high-resolution products for ocean models.

After adjusting local atmospheric variables and fluxes, the global flux budgets based on a specified SST (the COBESST product) were positively biased on a multi-decadal time scale. This result implies that biases still remain in all flux components and they can vary regionally. In a forced ocean–sea-ice model, a balanced heat budget can be achieved by developing globally high SSTs, allowing additional surface heat losses through upward longwave, sensible, and latent heat fluxes, to compensate for the excessive downwelling radiation fluxes (e.g., Brodeau et al., 2010). An enhanced evaporation will affect the freshwater balance, but there is no feedback process to restore a balance. Thus a global adjustment on freshwater fluxes is always warranted in a global ocean–sea-ice model simulation if the freshwater fluxes are treated explicitly. (This is not necessary if the freshwater fluxes are converted to the corresponding virtual salt fluxes.) To minimise these false adjustments in forced ocean–sea-ice models, the global flux budgets based on a realistic SST should preferably be balanced. In the present study, we took a relatively simple approach to close a long-term (1988–2007) surface flux budget by applying a globally and temporally constant multiplicative factor on downwelling radiations and precipitation. The factors are applied for the entire dataset period. These adjustment factors can be revised if major regional biases in any variables of the present version are identified.

After assessing the large-scale features and global balances of the fluxes, we confirmed that JRA55-do is a valid alternative to the CORE dataset for driving global ocean–sea-ice models. We hypothesise that the technical advances incorporated into JRA55-do will improve many aspects of ocean modelling studies. However, the production processes will be continually reviewed and revised based on experience from the wide suite of anticipated studies. Specifically, the downward fluxes affected by clouds (radiation and precipitation fluxes) were derived from a reanalysis product. The validity of this choice should be carefully checked and reviewed in future studies. Also, the adjustment methods of all variables require large improvements near the coast (e.g., Taboada et al., 2018). The horizontal resolution of JRA-55 (~ 55 km) is still insufficient for capturing the meteorological features affected by orography in the coastal regions, and the reference datasets in the present adjustment methods (except for the scatterometer wind products) are even less well-resolved.

Our group is planning to write several papers related to the present study. For the simulation paper, a number of international groups will conduct long-term inter-annual simulations forced by both CORE and JRA55-do, and compare their mean states and variabilities. The normal or repeat-year forcing paper will propose typical years that represent the present climate, and display the results of model integrations forced by repeated use of each of those years. Additionally, we expect various studies will arise from the CMIP6/OMIP process (Griffies et al., 2016), which makes use of both the CORE and JRA55-do forcing.

The JRA55-do dataset is registered with “input datasets for Model Intercomparison Project (input4MIPs)” and can be obtained from the input4MIPs website.[1] The program codes used to generate the JRA55-do dataset can be obtained from a repository on Github[2].

Acknowledgements

The CERES EBAF-Surface product (CERES EBAF-Surface_Ed2.8) data were obtained from the NASA Langley Research Center CERES ordering tool at http://ceres.larc.nasa.gov/. International Arctic Buoy Programme (IABP) / Polar Exchange at the Sea Surface (POLES) Arctic surface air temperature data are available and downloaded from http://research.jisao.washington.edu/data_sets/iabppoles/. QuikSCAT and SSM/I wind products are produced by Remote Sensing Systems and were obtained from http://www.remss.com/. GlobCurrent products were obtained from http://globcurrent.ifremer.fr/. GPCP Precipitation data are provided by the NOAA/OAR/ESRL PSD, Boulder, Colorado, USA, from their Web site at http://www.esrl.noaa.gov/psd/.

Feedback and generous supports provided by Patrik Hyder at UK Met Office, Kazutoshi Oonogi, Masahiro Hosaka, and Masayoshi Ishii at MRI, Tracy Ippolito at FSU, and participants of *CLIVAR Ocean Model Development Panel (OMDP) Mini Workshop on Forcing ocean–Sea-ice Models*, which was held in January 2015 in Grenoble, France, *Extended CLIVAR-OMDP panel meeting on forcing ocean-ice climate models*, which was held in January 2016 in Yokohama, Japan, and CLIVAR OMDP panel meetings, which were held in September 2016 in Qingdao, China and in October 2017 in Exeter, UK, and the continuous support from the members of CLIVAR-OMDP as well as the many other modelling groups that have tested versions of JRA55-do, are gratefully acknowledged. The use of a CEOF analysis for the wind direction adjustment was suggested by Yutaka Yoshikawa at Kyoto University.

This study was supported by JSPS KAKENHI Grant Number 15H03726. NCAR contribution to this study was supported by the NOAA Climate Program Office Climate Variability and Predictability Program. NCAR is sponsored by the US National Science Foundation. The PCMDI/LLNL contribution to this study was performed under the auspices of the U.S. Department of Energy by Lawrence Livermore National Laboratory under Contract DE-AC52-07NA27344. We also acknowledge support from the U.S. Department of Energy, Office of Science, Climate and Environmental Sciences Division, Regional and Global Modeling and Analysis Program.

The present effort to produce the JRA55-do dataset is a project separated from the JRA-55 project conducted by Japan Meteorological Agency. Feedback should be directed to the authors of this paper, not to the contact of the JRA-55 project.

[1] https://esgf-node.llnl.gov/search/input4mips/. Search with a keyword “OMIP”. One must be a registered user to download data.

[2] https://github.com/HiroyukiTsujino/JRA55-do/

Appendix A. Processing raw JRA-55 data

A1. Mapping from reduced to normal latitude - longitude (TL319) grid

The basic atmospheric model of JRA-55 uses a reduced TL319 grid, on which the raw JRA-55 data are provided. The number of longitudinal grid points is reduced at latitudes poleward of 41.5°, and the first datum of each latitude band is placed at 0° longitude.

After the first (main) adjustment stage, the adjusted data are zonally regridded at the common interval of 0.5625° for all latitude bands by the following rules:

- If the target grid point is between two oceanic grid points, its value is found by linear interpolation.
- If the target grid point is between an ocean and a land grid point, it is treated as an ocean grid if it locates at the mid-point or closer to the ocean grid. Its value is then computed as the weighted average of the values of the ocean grid points among six candidate points. The candidate points are the three pairs of the two points flanking the target longitude or residing on the two adjacent latitudinal circles. The weighting factor is the inverse of the distance from the target point.
- If the target grid point is determined as a land point, its value is found by linear interpolation.

A2. Shifting the temperature and specific humidity of JRA-55 from 2 m to 10 m

JRA-55 provides the surface air temperature and specific humidity at 2 m above the surface. As in the CORE dataset, the temperature and specific humidity in the final dataset are provided at 10 m above the surface, where the wind vectors are measured. In JRA55-do, the air temperature and specific humidity of the JRA-55 forecast fields are adjusted at 2 m height, because the reference fields of both variables (IABP-NPOLES and the atmospheric reanalysis products for computing the ensemble mean) are available at this height. The main adjustments to the forecast fields are made on the original (reduced TL319) grid points of JRA-55.

After the main adjustment on the surface air temperature and specific humidity (Sections 3.3.2 and 3.3.3), the following steps are taken to produce the final product of the surface meteorological variables.

- The equivalent neutral wind at 10 m height of JRA55-raw is estimated based on the adjusted air temperature and specific humidity at 2 m.
- The equivalent neutral wind field is adjusted (Section 3.4).
- The adjusted air temperature and specific humidity at 2 m are shifted upwards to 10 m and the adjusted wind vector is converted from neutral to actual stability.
- Additional adjustments are performed on the air temperature and specific humidity at 10 m (Section 3.3.4).

In the suite of operations, we use the bulk formula of Large and Yeager (2009) and a set of formulas to compute the properties of moist air based on Gill (1982) (Appendix B). The surface temperatures of the ocean grids with and without sea-ice are taken from the surface brightness temperatures of JRA-55 and from COBESST, respectively. The surface temperatures of land grids are taken from the brightness temperature of JRA-55. The computation of the bulk transfer coefficient is iterated five times at most.

Appendix B. Computation of properties of moist air

In producing the JRA55-do dataset, a set of formulas given by Gill (1982) is used to compute properties of moist air, which is thought to be more accurate than that used for producing the CORE dataset. We recommend using these formulas for driving ocean–sea-ice models. Formulas used for producing the CORE dataset and in the current framework of CORE/OMIP are given by Large and Yeager (2004), which is replicated here for comparison.

B1. Saturation specific humidity

We consider computing saturation specific humidity in an environment with the sea-surface temperature t (°C) and pressure p (hPa). The relation between the vapor pressure e (hPa) and specific humidity q is given by

$$e/p = q/(\omega + (1 - \omega)q), \tag{B.1}$$

where ω is the molecular weight ratio between water vapor and air:

$$\omega = m_w/m_a = 18.016/28.966 = 0.62197. \tag{B.2}$$

This is solved for the specific humidity as

$$q = \omega e/(p - (1 - \omega)e). \tag{B.3}$$

The relative humidity γ is the mixing ratio of the mass of vapor to the mass of dry air divided by that of the saturated one. The mixing ratio (r) of the mass of vapor to the mass of dry air is given by

$$r = \frac{q}{1 - q}. \tag{B.4}$$

Thus, the relative humidity is computed using the specific humidity q and the saturation specific humidity q_{sat} as

$$\gamma = \frac{q(1 - q_{sat})}{q_{sat}(1 - q)}. \tag{B.5}$$

B1.1. Gill (1982)

The saturation vapor pressure e_{sw} (in units hPa) of pure water vapor over a plane water surface is given by

$$\log_{10} e_{sw}(t) = (0.7859 + 0.03477\,t)/(1 + 0.00412\,t). \tag{B.6}$$

In air, the partial pressure e'_{sw} of water vapor at saturation is not exactly e_{sw} but is given by

$$e'_{sw} = f_w e_{sw}. \tag{B.7}$$

The value of f_w is given by

$$f_w = 1 + 10^{-6} p(4.5 + 0.0006\,t^2), \tag{B.8}$$

where p is the pressure (units in hPa).

The saturation vapor pressure over a salt solution is less than over freshwater. For sea water, the reduction is about 2% (a factor of 0.98 should be applied to e'_{sw}).

The saturation vapor pressure e_{si} of pure water vapor over ice is given by

$$\log_{10} e_{si}(t) = \log_{10} e_{sw}(t) + 0.00422\,t. \tag{B.9}$$

The saturation partial pressure e'_{si} in moist air is f_i times e_{si}. Values of f_i are given correct to 1 part in 10^4 by (B.8). Thus

$$e'_{si} = f_w e_{si}. \tag{B.10}$$

B1.2. CORE

Following Large and Yeager (2004), over sea water,

$$q_s = \rho_a^{-1} a_1 e^{a_2/(t+273.15)}, \tag{B.11}$$

where $a_1 = 0.98 \times 640380\,\mathrm{kg\,m^{-3}}$ and $a_2 = -5107.4\,\mathrm{K}$. The factor 0.98 applies only over sea-water. ρ_a is the density of air. Over sea-ice, the formula of the same form is used, but now $a_1 = 11637800\,\mathrm{kg\,m^{-3}}$ and $a_2 = -5897.8\,\mathrm{K}$.

In summary, we advocate replacing the CORE computation of saturation specific humidity (B.11) with the more accurate formulation given by (B.3) together with (B.7) and (B.10).

B2. Specific heat

The specific heat of air c_{pa} is given as follows.

B2.1. Gill (1982)

$$\begin{aligned} c_{pa} &= \frac{7}{2} R\left(1 - q + \frac{8q}{7\omega}\right), \\ &= 1004.6 \times (1 + 0.8735q)\,(\mathrm{J\,kg^{-1}\,K^{-1}}). \end{aligned} \tag{B.12}$$

Here, $R = 287.04\mathrm{Jkg^{-1}K^{-1}}$ is the gas constant of dry air.

B2.2. CORE

$$c_{pa} = 1000.5\,(\mathrm{J\,kg^{-1}\,K^{-1}}). \tag{B.13}$$

B3. Latent heat

The latent heat of vaporisation (L_v) and sublimation (L_s) are given as follows.

B3.1. Gill (1982)

$$L_v = 2.5008 \times 10^6 - 2.3 \times 10^3 t\,(\mathrm{J\,kg^{-1}}), \tag{B.14}$$

$$L_s = 2.839 \times 10^6 - 3.6(t + 35)^2\,(\mathrm{J\,kg^{-1}}). \tag{B.15}$$

B3.2. CORE

$$L_v = 2.5 \times 10^6\,(\mathrm{J\,kg^{-1}}), \tag{B.16}$$

$$L_s = L_v + L_f = 2.839 \times 10^6\,(\mathrm{J\,kg^{-1}}). \tag{B.17}$$

Here, L_f is the latent heat of fusion:

$$L_f = 3.337 \times 10^5\,(\mathrm{J\,kg^{-1}}). \tag{B.18}$$

As Brodeau et al. (2010) pointed out, choosing Gill's (1982) formula will result in a smaller latent heat loss from the ocean than the case where a constant as in CORE is chosen. The surface heat flux budget will be positively biased (heating of the ocean) in comparison with the evaluation presented by Large and Yeager (2009).

B4. Air density

The equation of state of moist air of temperature θ (K) under the pressure P (Pa) is given by

$$\rho_a = \frac{P}{R\theta(1 - q + q/\omega)} \equiv P/RT_v, \tag{B.19}$$

where

$$T_v \equiv \theta(1 - q + q/\omega) = \theta(1 + 0.6078q) \tag{B.20}$$

is called the virtual temperature.

B4.1. Gill (1982)

$$\rho_a = \frac{P}{R\theta(1 - q + q/\omega)}. \tag{B.21}$$

B4.2. CORE

$$\rho_a = 1.22\,\mathrm{kg\,m^{-3}}. \tag{B.22}$$

Appendix C. Details of the dataset

C1. Dataset description

The JRA55-do dataset consists of nine surface-atmospheric variables derived from JRA-55 and river runoff data (freshwater discharge at river mouths) resulting from several sources (Table 1). All surface-atmospheric fields are derived from the forecast phase of JRA-55. The temporal coverage is 3-hourly from the 1st of January 1958 to the present (to be updated at least annually). The downward surface fluxes, (the downwelling shortwave and longwave radiation fluxes) and precipitation (rain and snow), are averaged over three hours. The first datum of each year is averaged from 00:00 to 03:00 GMT on the 1st of January. Other surface-atmospheric fields, namely, the air temperature, specific humidity, wind vectors (all at 10 m height, see Appendix A.2 for the height shift of temperature and specific humidity), and sea level pressure, are 3-hourly instantaneous values starting at 00:00 GMT on the 1st of January of each year.

All variables except the sea level pressure are modified from their original fields by multiplicative or offsetting factors to fit the reference fields derived from observations or other datasets. The modification and adjustment procedures are explained in Sections 3 and 5.

JRA-55 does not directly provide the river runoff from rivers and glaciers at river mouths. The liquid runoff fields are obtained from a river-routing model forced by runoffs from the land-surface component of JRA-55 (Suzuki et al., 2017). The runoffs from Greenland and Antarctica, which contain a significant solid runoff component, are taken from independent estimates that combine satellite observations of solid discharge with high-resolution climate models of runoff and surface processes (Bamber et al. (2012) and Depoorter et al. (2013), respectively). The river runoff data are explained in Section 4. The daily runoff from Greenland is based on the monthly climatology (1961–1990) and the liquid-plus-solid runoff. For time interpolation from monthly to daily data, a method to preserve monthly mean values introduced by Killworth (1996) is used. The runoff from Antarctica is constant in time and the liquid-plus-solid runoff. Besides the merged runoff data, we provide the solid water discharge from Antarctica represented as the calving flux derived from Depoorter et al. (2013) (Table 2).

C2. Supplementary data

The dataset also includes the following supplementary data summarised in Table 2.

C2.1. Variables at the sea-surface

The variables at the sea-surface are necessary for computing surface fluxes. In most ocean–sea-ice models, these variables are taken from their own solution. Thus, including a set of sea-surface variables is not prerequisite to a dataset for driving ocean–sea-ice models. However, to assist computation of surface fluxes without using ocean–sea-ice models, the observation-based data for the sea-surface variables are provided as part of the dataset. We included surface temperature derived from brightness temperature of JRA-55, sea-surface temperature from COBESST (Ishii et al., 2005), sea-ice area fraction from both JRA-55 and COBESST, and surface oceanic current from the GlobCurrent dataset (Rio et al., 2014). As discussed in Section 3.4, the surface oceanic current may be added to the time series of the wind vector of this dataset to approximately construct a time-series of the absolute wind vector.

In most ocean–sea-ice model simulations uncoupled with atmospheric models, sea-surface salinity is restored to observational data to prevent model drifts. For this purpose, we provide monthly climatology of sea-surface salinity derived from the World Ocean Atlas 2013 version 2 (Zweng et al., 2013; Boyer et al., 2015). This is computed as an average in the upper 10 m, thus it should be more appropriately understood as salinity at 5 m depth.

C2.2. Land-sea mask

The land-sea mask for the atmospheric data on a TL319 grid is based on the original land-sea mask of JRA-55. The original land-sea mask (land = 1, sea = 0) on the reduced TL319 grid is linearly interpolated in the zonal direction onto the normal latitude - longitude (TL319) grid. A grid point valued at 0.5 or less is designated as a sea point; otherwise, it is assigned to land. Then, inland seas and lakes such as the Caspian Sea and Lake Victoria are manually buried and designated as land. In the data provided, land and sea grids are set to zero and unity, respectively.

C2.3. Grid information

The Earth's sphere is occupied by grid cells centred at the latitudes and longitudes provided in the data file for each variable. Cell boundaries are given by lat_bnds and lon_bnds variables contained in each file. Note that the grid spacing is different depending on the variable. Atmospheric variables derived from JRA-55 are put on a TL319 grid (~ 0.5625°). River runoff data are equally spaced by 0.25°, starting at 0.125° longitude and

− 89. 875° latitude. Therefore, the longitude and latitude bounds are also equally spaced, starting at 0° longitude and − 90° latitude. The areas of the cells are provided for the atmospheric grid (TL319) and the river runoff grid (0.25° × 0.25°).

C3. Planned updates and older versions

The latest version of JRA55-do as of April 2018 is 1.3. The plan is to continually update this version using near real-time updates to the raw JRA-55 reanalysis. The version number will advance, accompanied by a detailed document, whenever new datasets or adjustment methods are incorporated. We will soon upgrade (in version 1.4) the Greenland runoff to include interannualy-varying forcing from 1958 to 2016, incorporating an update to Bamber et al. (2012) that extends the seasonally-varying time-series to 2016 (Bamber et al., 2018). The updated time-series will also include runoff from Arctic glaciers and ice caps which have also started to rapidly lose mass since the early 2000s (Bamber et al., 2018), in addition to those over Greenland as reported by Bamber et al. (2012). The cumulative runoff anomaly in the new time-series will be about twice that of Bamber et al. (2012) because of the inclusion of, in particular, Canadian Arctic glaciers and the extension of the time-series to 2016. Separate components of runoff (liquid and solid) as well as the total runoff will be provided.

There are several older versions that deserve mention. Because there are many users of versions 1.1 and 1.2, we list in the following the fixes and upgrades included in versions 1.3 and 1.2 relative to their immediate predecessors as a convenient reference.

C3.1. Difference between versions 1.3 and 1.2

In version 1.2, the magnitude of the wind vector was adjusted by a multiplicative factor $R_S(\lambda, \phi)$, whereas an offsetting factor was used for version 1.3 (Section 3.4.2). The adjustment of the wind direction was the same as that described in the main text. The wind vector of JRA55-raw $(u_{\mathrm{JRA55}}, v_{\mathrm{JRA55}})$ at (λ, ϕ) was adjusted as follows (cf. (19)):

$$\begin{pmatrix} u_{\mathrm{adj}} \\ v_{\mathrm{adj}} \end{pmatrix} = R_S(\lambda, \phi) \begin{pmatrix} \cos\chi & -\sin\chi \\ \sin\chi & \cos\chi \end{pmatrix} \begin{pmatrix} u_{\mathrm{JRA55}} \\ v_{\mathrm{JRA55}} \end{pmatrix}, \tag{C.1}$$

where

$$R_S = \frac{\overline{W}_{\mathrm{ref}}}{\overline{W}_{\mathrm{JRA55}}}. \tag{C.2}$$

In this adjustment method, high winds are selectively modified by a large amount to produce a mean wind speed that matches that of the reference field. This treatment may significantly modify the variance of the wind speed and hence the magnitude of the wind stress, which is a quadratic function of the wind speed.

Figs. 33 and 34 show the comparison of the basin-wide zonal mean wind stress. As expected, the zonal wind stress (Fig. 33) is enhanced in version

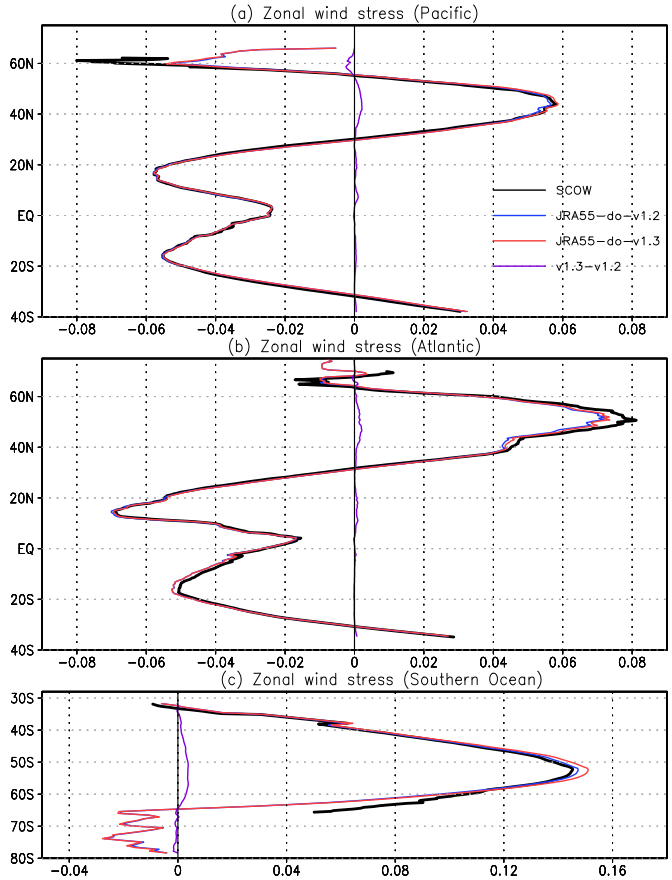

Fig. 33. Comparison of mean (Nov 1999–Oct 2009) basin-wide averaged zonal wind-stress ($\mathrm{N\,m^{-2}}$) in (red) JRA55-do-v1.3, (blue) JRA55-do-v1.2, and (purple) difference (v1.3 - v1.2). The black lines plot the Scatterometer Oceanic Wind Stress data of Risien and Chelton (2008). (For interpretation of the references to colour in this figure legend, the reader is referred to the web version of this article.)

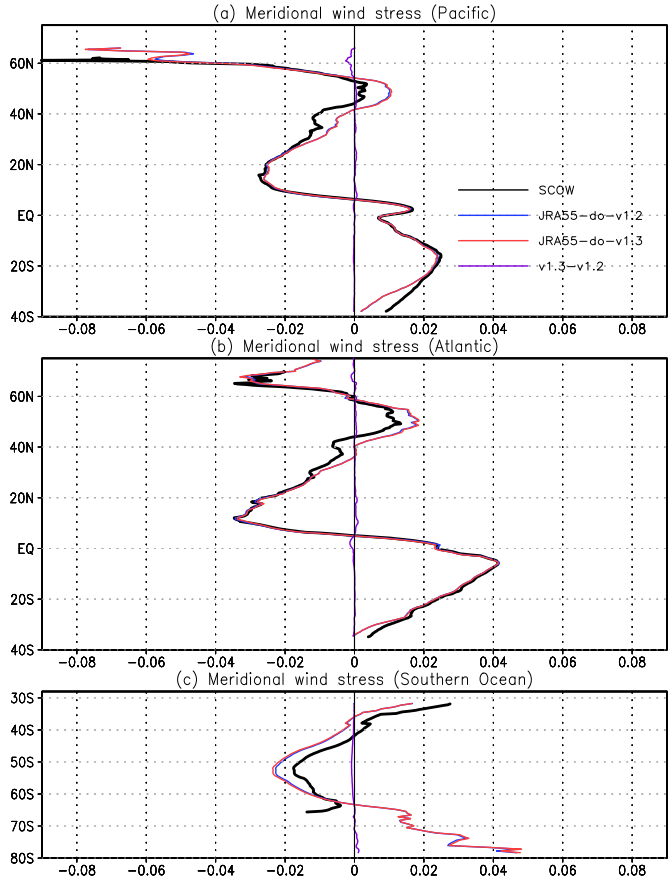

Fig. 34. Same as Fig. 33 but for the meridional wind-stress.

1.3 in the mid-latitude westerly region. Compared to the Scatterometer Oceanic Wind Stress (SCOW) product (Risien and Chelton, 2008), the zonal wind stress in version 1.3 in the mid latitudes of the Northern Hemisphere is reasonable, but the stress is too strong in the Southern Hemisphere. However, the Southern Ocean westerlies in version 1.3 still exhibit improvements relative to JRA55-raw (Fig. 28). The meridional wind stress is similar between versions 1.2 and 1.3 (Fig. 34). As shown in Fig. 29, version 1.3 is closer to SCOW than CORE and JRA55-raw. For these reasons, we made a shift to version 1.3.

C3.2. Difference between versions 1.2 and 1.1

Version 1.2 includes the following updates relative to version 1.1.

- (Bug fix) An error in computing the annual mean climatology of wind speed for JRA-55 and JRA-55C was corrected. This resulted in minor (less than 0.5%) changes in the adjustment factors for wind speed.
- (Bug fix) The temperature and specific humidity anomalies of CORE relative to JRA-55 were not added to JRA-55 in inland seas and lakes poleward of 40°N (Section 3.3.4).
- (Upgrade) The phase-III precipitation adjustment was further divided into 1999–2006 and 2006–2015 to suppress the recent positive trend (Section 3.6).
- (Upgrade) The contributions to the (ensemble mean) temperature and specific humidity reference data from NCEP-R1, NCEP-R2, and 20CRv2 were reduced around semi-enclosed seas (Section 3.3.1, Fig. 2).
- (Upgrade) The region of full ice-cover (fraction $>$ 0.99) used for smoothing temperature and specific humidity was determined based on daily, instead of monthly, COBESST data to facilitate quicker updating in the future (Section 3.3.4).
- (Upgrade) When calculating surface fluxes using the bulk formula to determine the globally uniform, constant adjustment factors applied to downward fluxes, scalar wind speed is first calculated on the original grid of the dataset and then interpolated onto the COBESST ($1^\circ \times 1^\circ$) grid. In the older version, the wind vector components were first interpolated onto the COBESST grid before computing the scalar wind speed (Sections 5 and 6).

Fig. 35 shows the comparison of surface fresh water fluxes between versions 1.1 and 1.2. The global ocean-integrated evaporation flux from versions 1.1 and 1.2 lie on top of each other, but the flux in version 1.1 is reduced by about 1% when the older wind treatment is used (the last item in the above list). This is reflected in slightly reduced precipitation in version 1.1 before 1996 (phases I and II), when the common, spatially-dependent adjustment factors are used. In version 1.1, the precipitation shows an increasing trend in the most recent decade. This motivated us to divide the phase-III at 2006, corresponding to the time period when GNSS-RO as well as an increased number of radiance observations from satellite water vapor channels were introduced in the reanalysis.

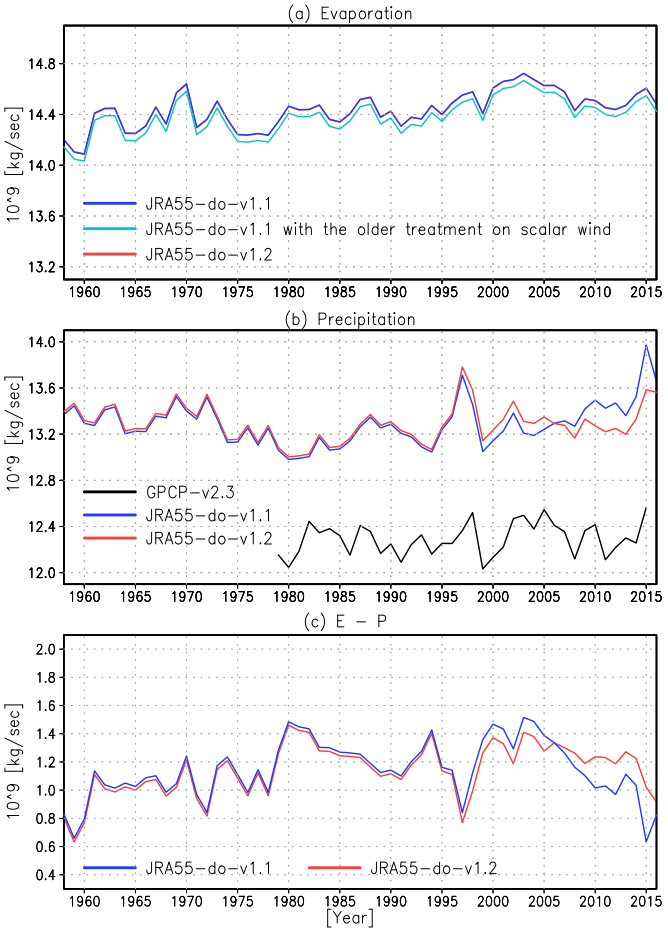

Fig. 35. Time-series of the annual mean global ocean-integrated (a) evaporation, (b) precipitation, (c) evaporation minus precipitation ($\times 10^9 \mathrm{kg\,s^{-1}}$) of JRA55-do-v1.1 (blue), and JRA55-do-v1.2 (red). Light blue line in (a) is the evaporation using the older treatment of scalar wind speed (see text). In (a), the blue (v1.1) and the red (v1.2) lines lie on top of each other. Black line in (b) is the precipitation of GPGP v2.3. Bulk formula and air-properties formulas are taken from Large and Yeager (2009) and Gill (1982), respectively. (For interpretation of the references to colour in this figure legend, the reader is referred to the web version of this article.)

Appendix D. COBESST

This appendix briefly introduces COBESST (Ishii et al., 2005), where 'COBE' is an acronym for centennial in situ observation-based estimates of the variability of SSTs and marine meteorological variables. COBESST is a daily objective analysis of sea-surface temperature on a $1^\circ \times 1^\circ$ grid spanning the global oceans for the period from 1870 to present. The objective analysis is based on optimal interpolation and reconstruction with empirical orthogonal functions. Only conventional observed datasets are used for the analysis. The COBESST dataset also contains sea-ice concentration (SIC) data derived from Walsh and Chapman (2001) in the pre-satellite period before October 1978 and from satellites afterwards. SST and SIC of COBESST were used as the lower boundary condition of JRA-55 (Kobayashi et al., 2015). For more details on the analysis method and the evaluation of the COBESST dataset, readers are referred to Ishii et al. (2005).

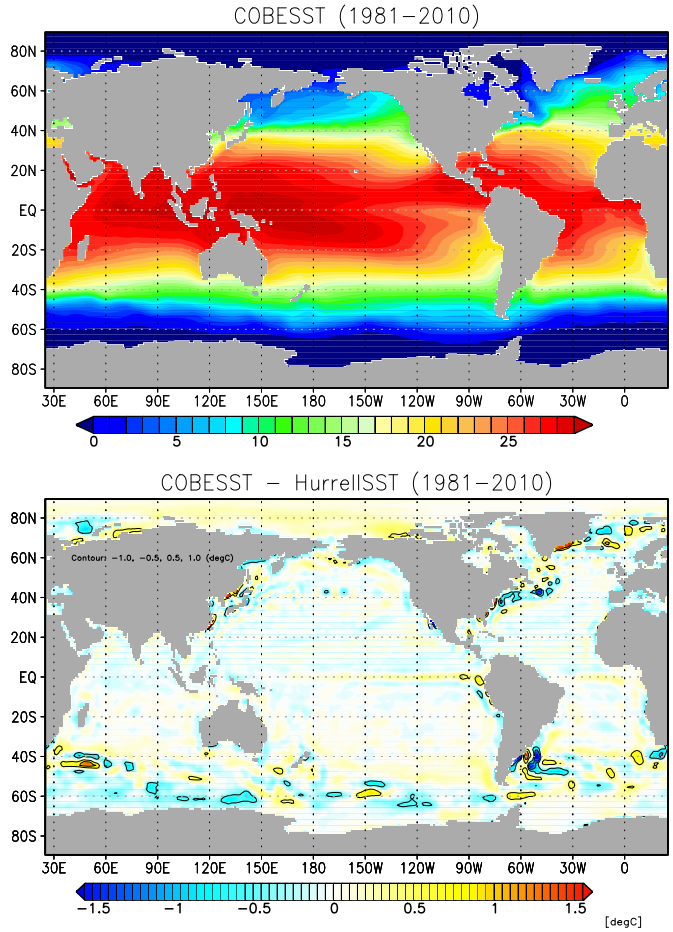

Fig. 36. Comparison between COBESST (Ishii et al., 2005) and the SST product by Hurrell et al. (2008). (a) Mean SST of COBESST (1981–2010) and (b) its difference from that of Hurrell et al. (2008).

Fig. 36 shows a long-term mean (1981–2010) SST from COBESST and the difference to Hurrell et al. (2008), which was used by Large and Yeager (2009) for evaluating surface fluxes based on the CORE dataset. COBESST exhibits features typical to low-resolution SST analyses: the weak SST fronts and the lack of explicit representation of mesoscale eddies. This would result in smooth surface flux distribution in the western boundary current regions (Appendix G). The difference from the SST product of Hurrell et al. (2008), which is also a low-resolution (1° × 1°) product, is less than 0.5 °C in most regions except for the mid-latitude frontal zones of the North and South Atlantic and the Southern Ocean. COBESST shows SSTs lower than the product of Hurrell et al. (2008) in the mid-latitude North and South Atlantic frontal zones. In a long-term average, this difference resulted in about 20 $\mathrm{W\,m^{-2}}$ less heat loss to the atmosphere due to latent plus sensible heat fluxes when COBESST was used as the lower boundary condition (not shown). Fig. 37 shows a long-term (1981–2010) root-mean-square difference from the monthly climatology and the comparison with the same quantity computed from the product of Hurrell et al. (2008). COBESST exhibits less variability than Hurrell et al. (2008), specifically in the SST frontal zones. This may have resulted in the reduced variability in the surface flux components when COBESST was used as the lower boundary condition. However, the difference in the long-term mean global ocean averaged heat fluxes is less than 0.5 $\mathrm{W\,m^{-2}}$ (Table 9) and is within the uncertainty ($\sim 0.5\,\mathrm{W\,m^{-2}}$; Loeb et al., 2012). Furthermore, the difference in the flux variability arising from the two different SST products is considerably smaller than the difference arising from the two different atmospheric fields (Fig. 22).

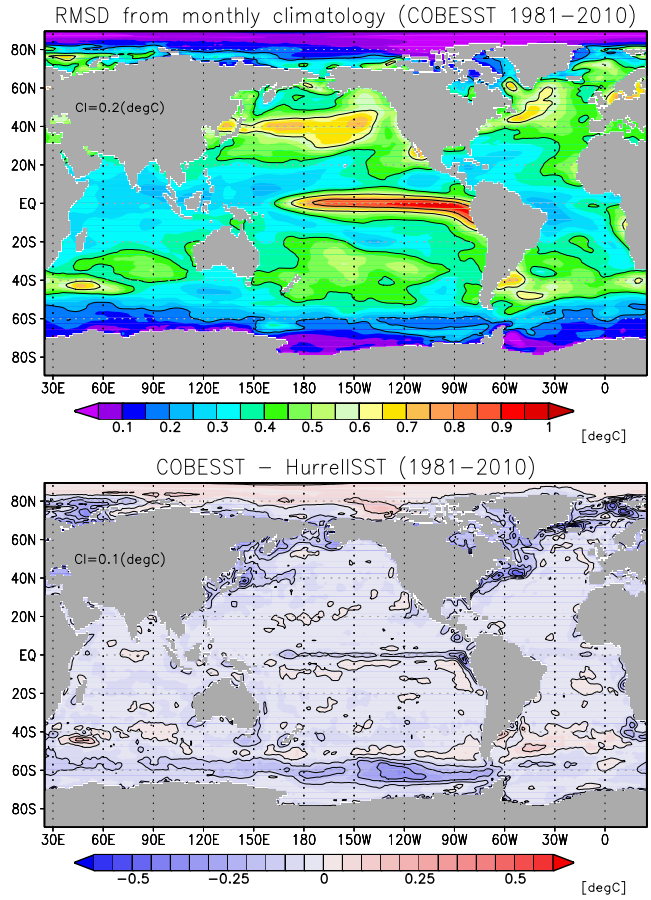

Fig. 37. (a) Root mean square difference (RMSD) from its monthly climatology for the time-series of monthly COBESST (1981–2010). (b) Its difference from the same quantity computed for the SST product by Hurrell et al. (2008).

Appendix E. Evaluation and adjustment to CERES-EBAF as a reference dataset

E1. Shortwave adjustment

Fig. 38 shows the biases relative to the buoy observations (expressed as percentages relative to the annual mean climatology) of the CERES downward shortwave radiation. To adjust the CERES radiation toward the buoy observations, this fraction is subtracted from (if positive) or added to (if negative) the annual mean values of the CERES radiation. The buoy observations were mainly available at low-latitudes. The biases revealed that

- CERES is positively biased in the tropics (except right at the Equator);
- The positive tropical biases in CERES are larger in the Northern Hemisphere than the Southern Hemisphere;
- Observations are limited at latitudes above ~ 30°N/S. Those available imply that the biases are generally small.

To evaluate the high-latitude radiation, we compared the CERES data with observations at land stations around the Arctic Ocean and the coastal zone of Antarctica. Fig. 39 shows the percentage biases from the land data in the monthly climatology of the CERES downward shortwave radiation. The bias typically reached +10% in the summer season of both hemispheres. The exceptions are stations GVN and NYA, where the areal fractions of sea-ice are small in summer (result not shown).

In conclusion, the downward shortwave radiation of CERES was reduced in the low-latitude regions as a function of latitude. In the mid-latitude regions, the downward shortwave radiation was unchanged. At high latitudes, the downward shortwave radiation was reduced by up to 10% over sea-ice, depending on the area fraction of the sea-ice (0% reduction for no ice coverage and 10% reduction for total ice coverage). Fig. 13a compares the downward shortwave radiations zonally averaged over the ocean among CORE, the raw CERES, and the adjusted CERES. The adjusted CERES generally gets close to CORE. The somewhat noisy structures of CERES at high latitudes are presumably because only polar orbit satellites are available poleward of around 60°. Fig. 13b shows the ratio of the adjusted CERES to the raw CERES, which represents the adjustment factor applied to the raw CERES as explained above. Then the adjusted downward shortwave radiation was applied as a reference field for adjusting the JRA-55 downward shortwave radiation.

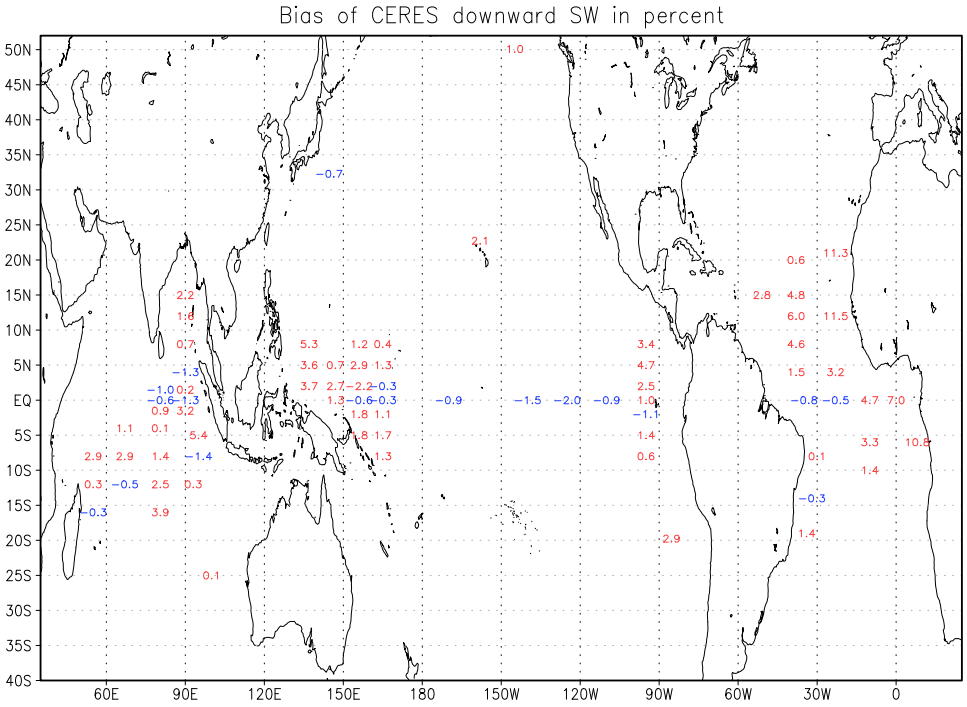

Fig. 38. Bias of downward shortwave radiation in the annual mean climatological values of CERES. Biases are expressed as percentage deviations from buoy observations. For adjustment toward the buoy observations, the bias fractions should be subtracted from (if positive) or added to (if negative) the annual mean CERES values. Comparison is made based on monthly data from Mar 2000 to Feb 2015. At each buoy location, the bias is depicted if buoy data are available for more than 12 months. An average of those available months is formally referred to as "annual mean climatology".

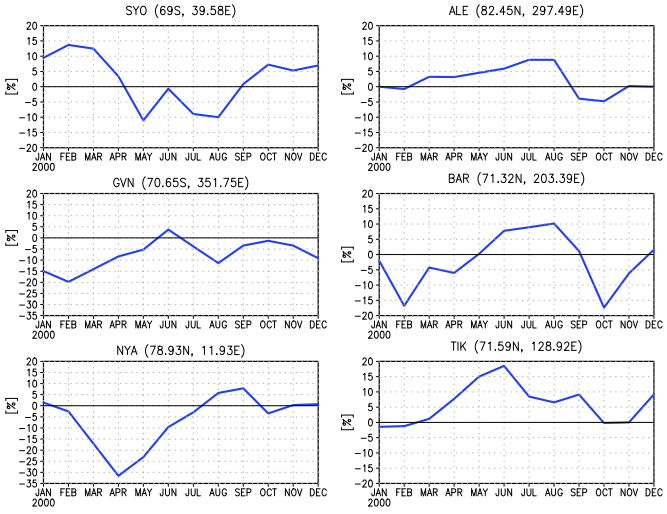

Fig. 39. Percentage bias that must be subtracted from (if positive) or added to (if negative) the CERES downward shortwave radiation to fit the high-latitude station observations. The bias fraction is based on comparisons between monthly climatologies. At each station, monthly climatologies for both in-situ observations and CERES are calculated using months when the station data are available in the period from Mar 2000 to Feb 2015. Note that in general, the positive biases are large in the summer months of both hemispheres. The station names are abbreviated as follows: SYO for Syowa (69°S, 39.58°E), GVN for Georg von Neumayer (70.65°S, 351.75°E), NYA for Ny Alesund (78.93°N, 11.93°E), ALE for Alert (82.45°N, 297.49°E), BAR for Barrow (71.32°N, 203.39°E), and TIK for Tiksi (71.59°N, 128.92°E).

E2. Longwave adjustment

Fig. 40 shows the percentage biases relative to the buoy observations in the annual mean climatology of the CERES downward longwave radiation. Note that the biases in the longwave radiation tend to offset those of the shortwave (Fig. 38), but the fractional differences are generally below 1%.

Fig. 41 shows the percentage biases in the monthly climatology of the CERES longwave radiation, relative to the observations at land stations around the sea-ice zones at high latitudes. Generally, the biases were less than 5% and their signs were not coordinated.

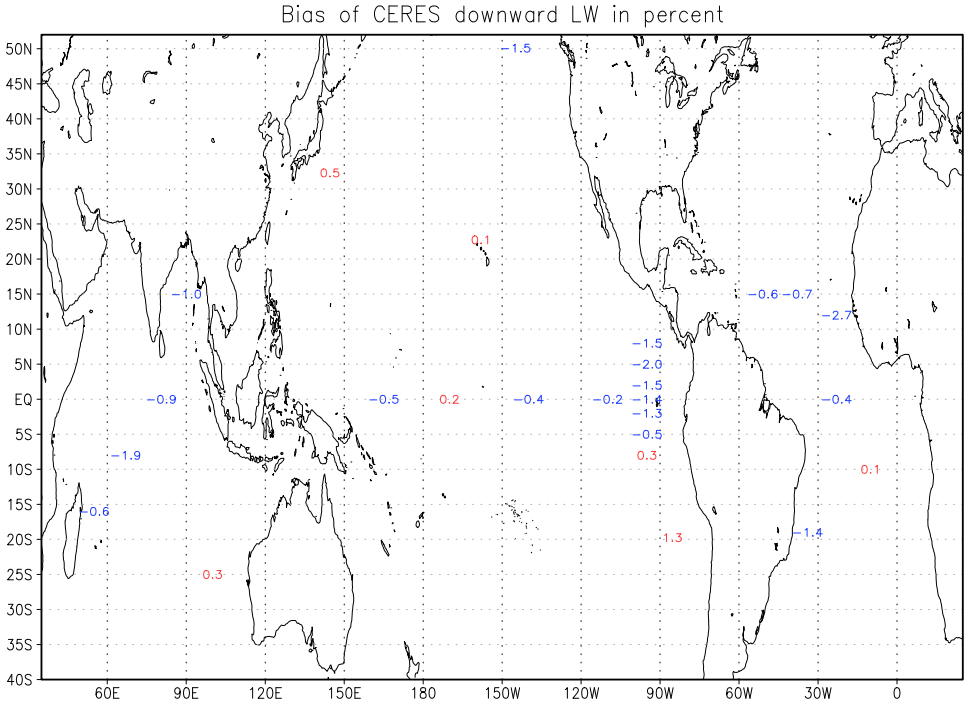

Fig. 40. Same as Fig. 38 but for the downward longwave radiation.

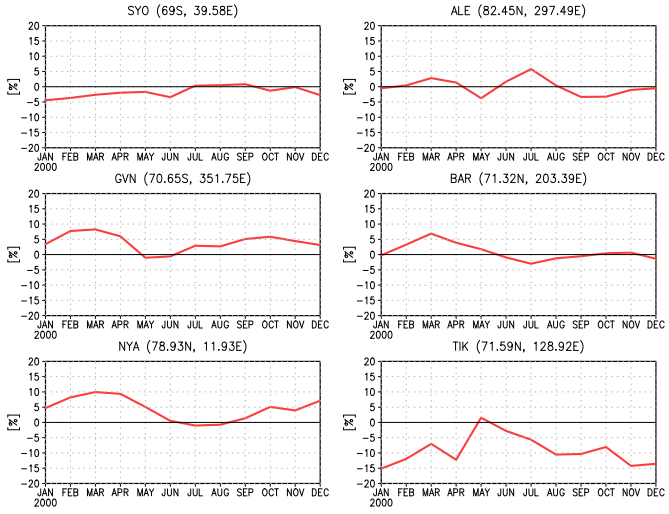

Fig. 41. Same as Fig. 39 but for the downward longwave radiation.

In conclusion, the downward longwave radiation of CERES is used as a reference field without adjustment. Note that in the second adjustment step, both the downward shortwave and longwave radiations are adjusted by a globally uniform, time-invariant factor that closes the surface heat flux budget (Section 5).

Appendix F. Comparison of marine meteorological variables with buoy data

Comparison of air temperature, specific humidity, and wind speed with buoy observations are presented in Figs. 42–47 for CORE, JRA55-raw, and JRA55-do. It is acknowledged that the buoy stations presented here do not represent the full array. It is hoped that more regionally focussed comparison studies by interested users will complement the present incomplete evaluation as the dataset is widely distributed. We understand the following features from the bias maps: The general cold bias of air temperature of JRA55-raw is corrected successfully in JRA55-do (Fig. 42). The specific humidity of JRA55-do has smaller bias than JRA55-raw and CORE in the middle and high latitudes, but it is lower than buoys in the tropics (Fig. 44). Recalling that the specific humidity of JRA55-raw was adjusted toward an ensemble of reanalyses in JRA55-do, the majority of reanalysis products have a low humidity bias in the tropics. The wind speed of CORE is generally higher than buoys (Fig. 46). As discussed in the main text, this is because the actual wind speed of NCEP-R1 was directly adjusted toward the equivalent neutral wind of QuikSCAT in CORE. From the scatter diagrams and the statistical values (Figs. 43, 45, and 47), we understand that JRA55-do gives the smallest root-mean-square errors and the highest

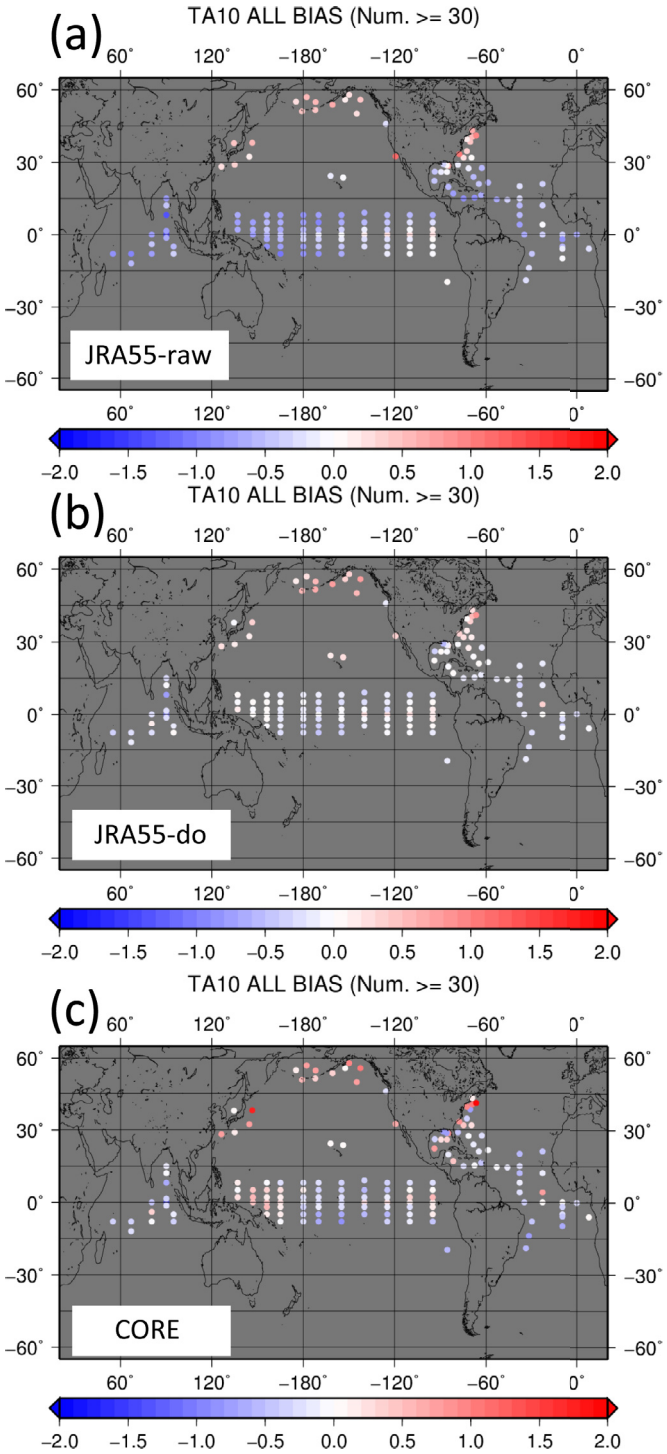

Fig. 42. Bias of air temperature at 10 m height relative to buoys (K). (a) JRA55-raw, (b) JRA55-do, and (c) CORE. Comparison is based on daily data from 2000 to 2009.

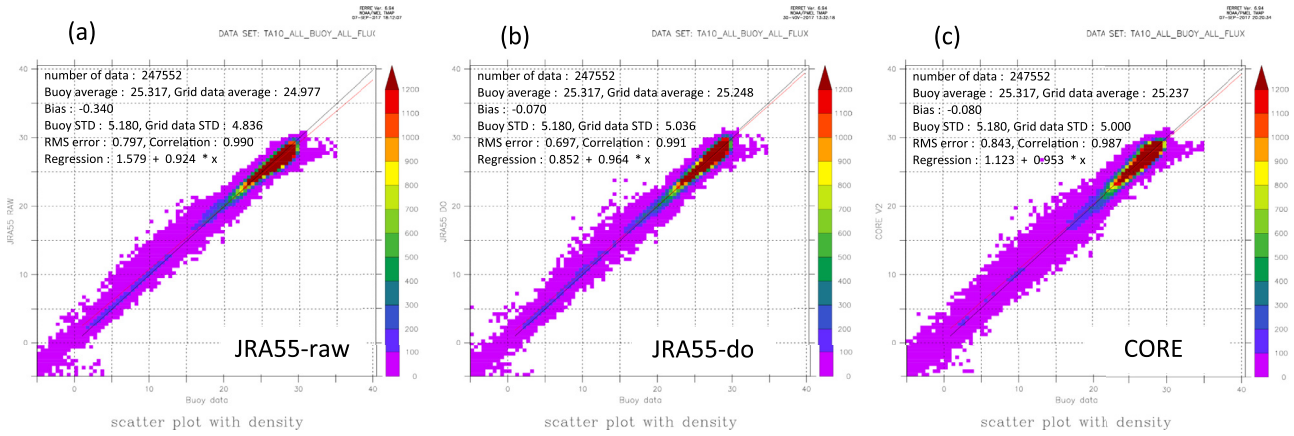

Fig. 43. Scatter diagram of air temperature at 10 m height between datasets and buoys. (a) JRA55-raw, (b) JRA55-do, and (c) CORE. Comparison is based on daily data from 2000 to 2009.

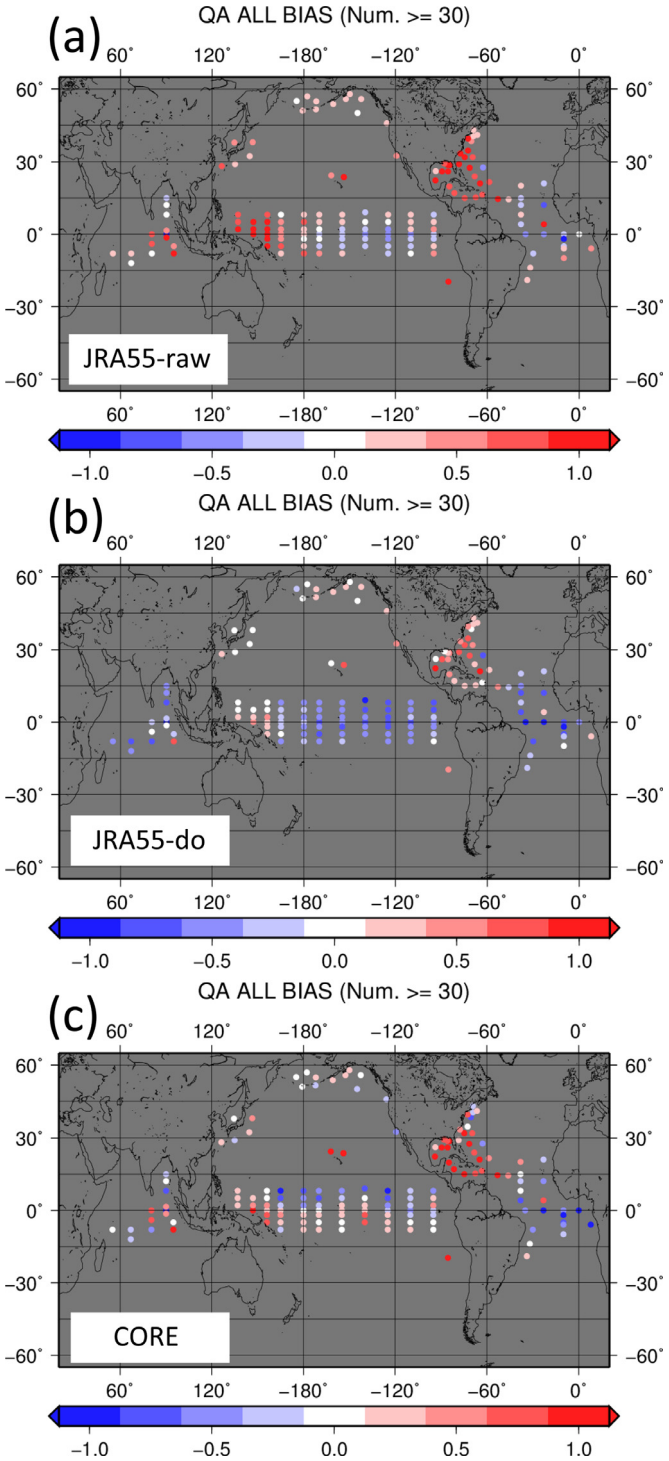

Fig. 44. Bias of specific humidity at 10 m height relative to buoys ($g\,kg^{-1}$). (a) JRA55-raw, (b) JRA55-do, and (c) CORE. Comparison is based on daily data from 2000 to 2009.

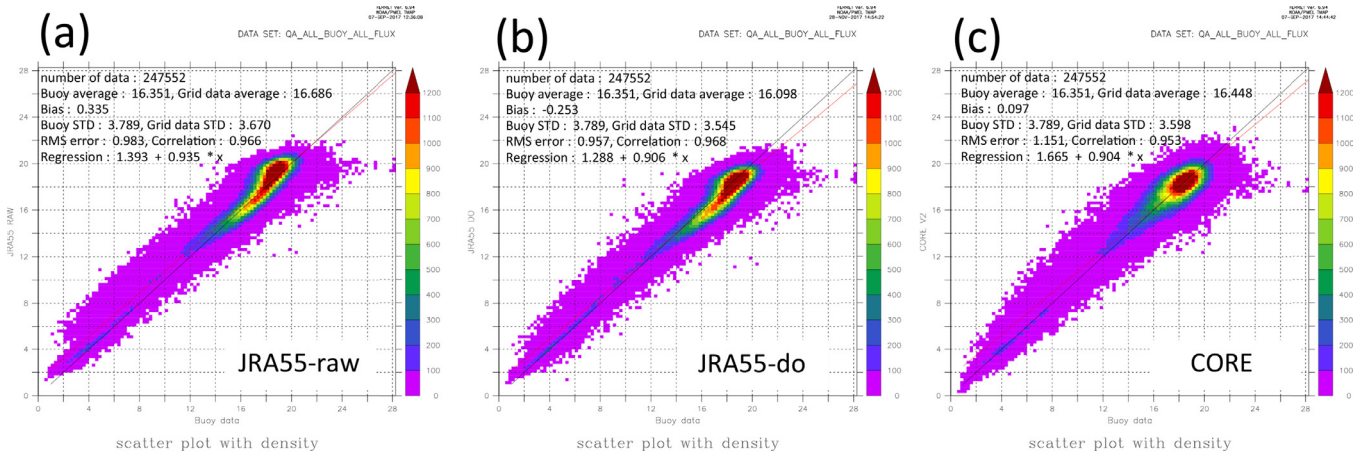

Fig. 45. Scatter diagram of specific humidity at 10 m height between datasets and buoys. (a) JRA55-raw, (b) JRA55-do, and (c) CORE. Comparison is based on daily data from 2000 to 2009.

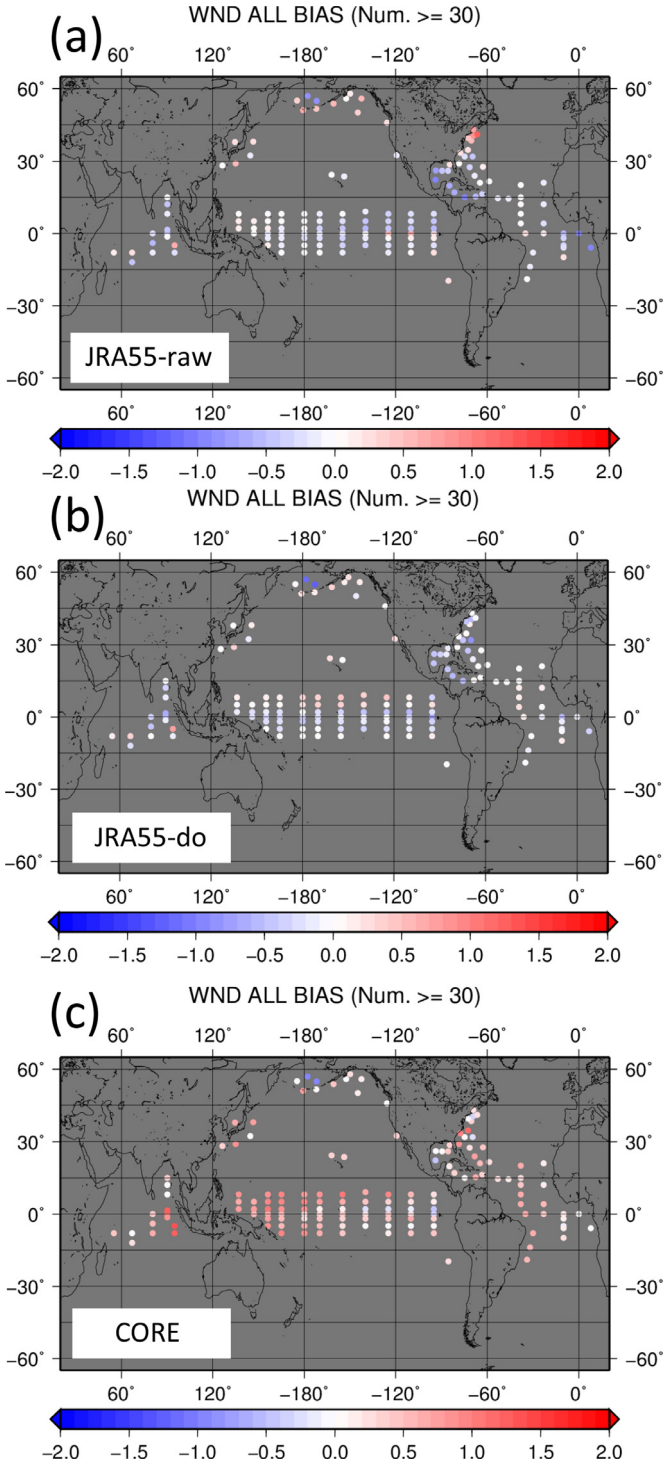

Fig. 46. Bias of scalar wind speed (equivalent neutral wind speed at 10 m height) relative to buoys ($m\,s^{-1}$). (a) JRA55-raw, (b) JRA55-do, and (c) CORE. Comparison is based on daily data from 2000 to 2009.

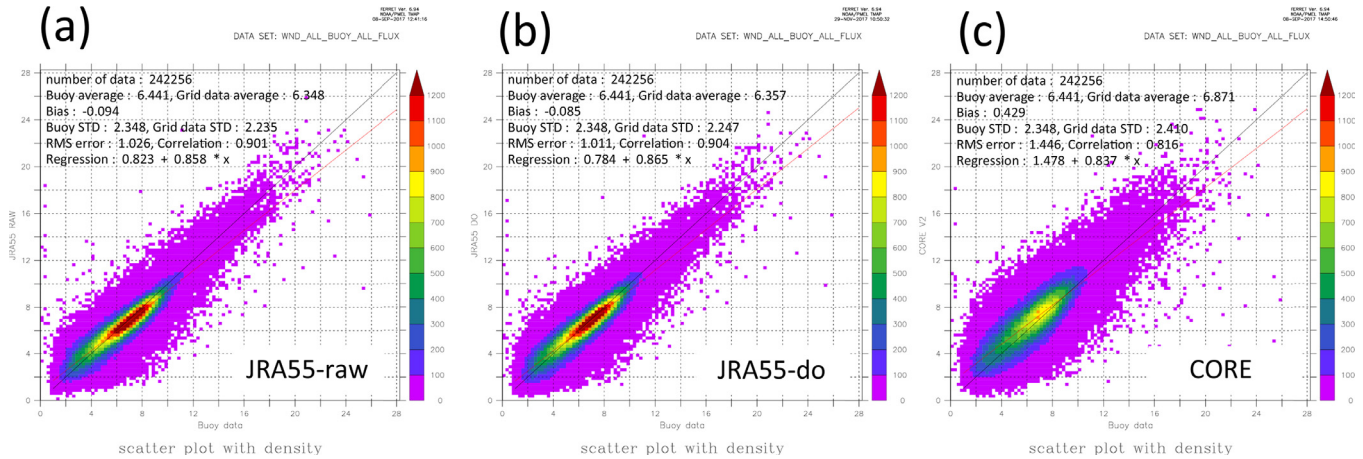

Fig. 47. Scatter diagram of wind speed (equivalent neutral wind speed at 10 m height) between datasets and buoys. (a) JRA55-raw, (b) JRA55-do, and (c) CORE. Comparison is based on daily data from 2000 to 2009.

correlation coefficients relative to buoys for all variables. The mean bias of JRA55-do is smallest for the air temperature and the wind speed. The mean bias of the specific humidity of JRA55-do is smaller than that of JRA55-raw, but it is larger than that of CORE. This is due to the low bias of the specific humidity of JRA55-do in the tropics as shown in the bias map (Fig. 44).

Appendix G. Atlas of surface flux distribution

G1. Heat flux

Figs. 48–Fig. 52 give the global map of the mean (1988–2007) total surface heat flux and components of JRA55-do as well as the difference from those of CORE. The total surface heat flux into the ocean of JRA55-do tends to be smaller in the tropics and larger in mid-latitudes, specifically in the North Atlantic, than that of CORE. This feature is dominated by the latent heat flux (Fig. 51). The differences of shortwave and longwave radiation flux from CORE (Figs. 49 and 50, respectively) are oppositely signed in the high latitudes, reflecting the compensatory natures of shortwave and longwave radiations in the radiative transfer models. In the tropics, only the shortwave radiation of CERES was reduced before it was used as the reference data to adjust the shortwave radiation of JRA55-raw based on the comparison with buoy observations (Appendix E and Fig. 13b). The wavy structures with $5° - 10°$ wave lengths in the difference of the sensible heat flux (the lower panel of Fig. 52) are due to those of the air temperature field of CORE, which are traceable to NCEP-R1.

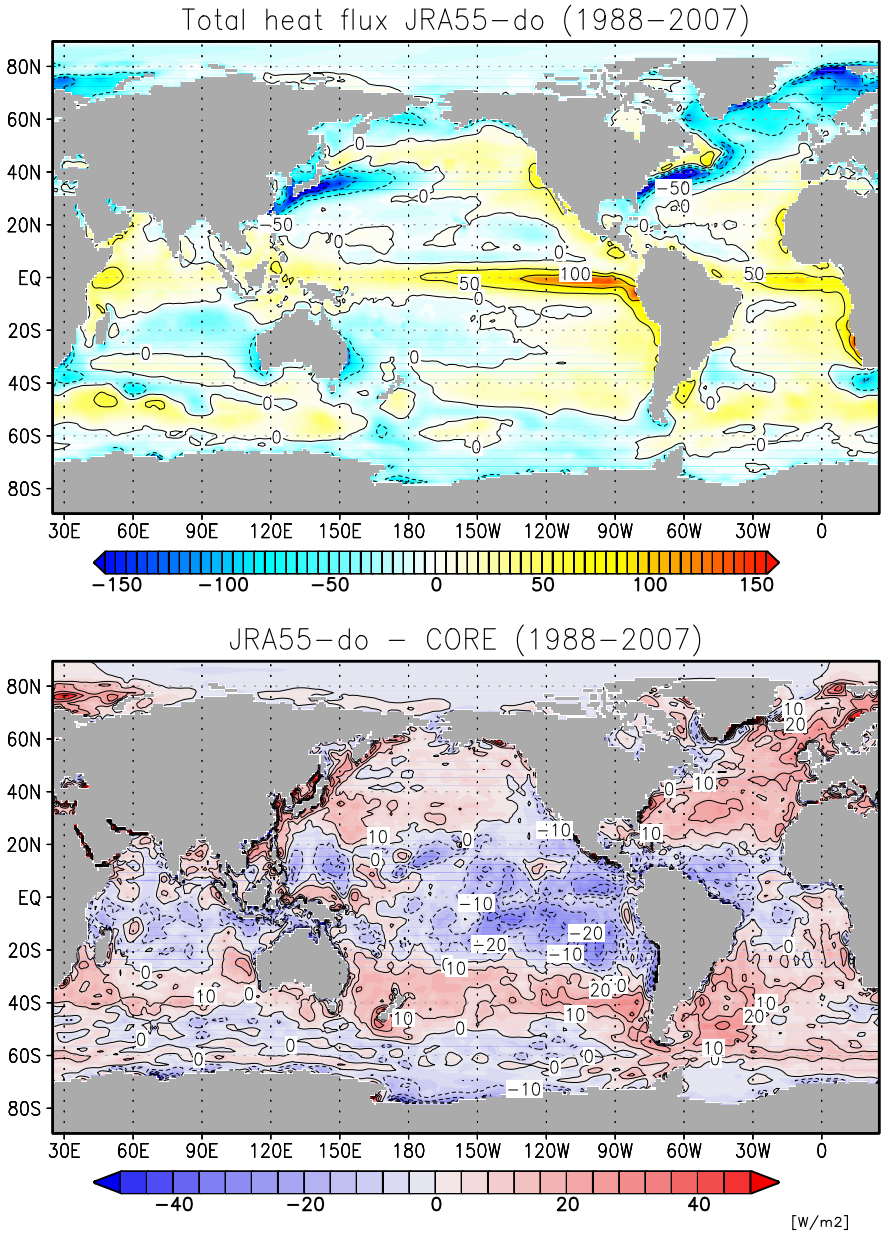

Fig. 48. Comparison of the total surface heat flux (the sum of net shortwave radiative, net longwave radiative, latent heat, and sensible heat fluxes). (upper) Mean (1988–2007) of JRA55-do and (lower) anomaly from CORE. Units are W m^{-2}. The direction is positive into the ocean.

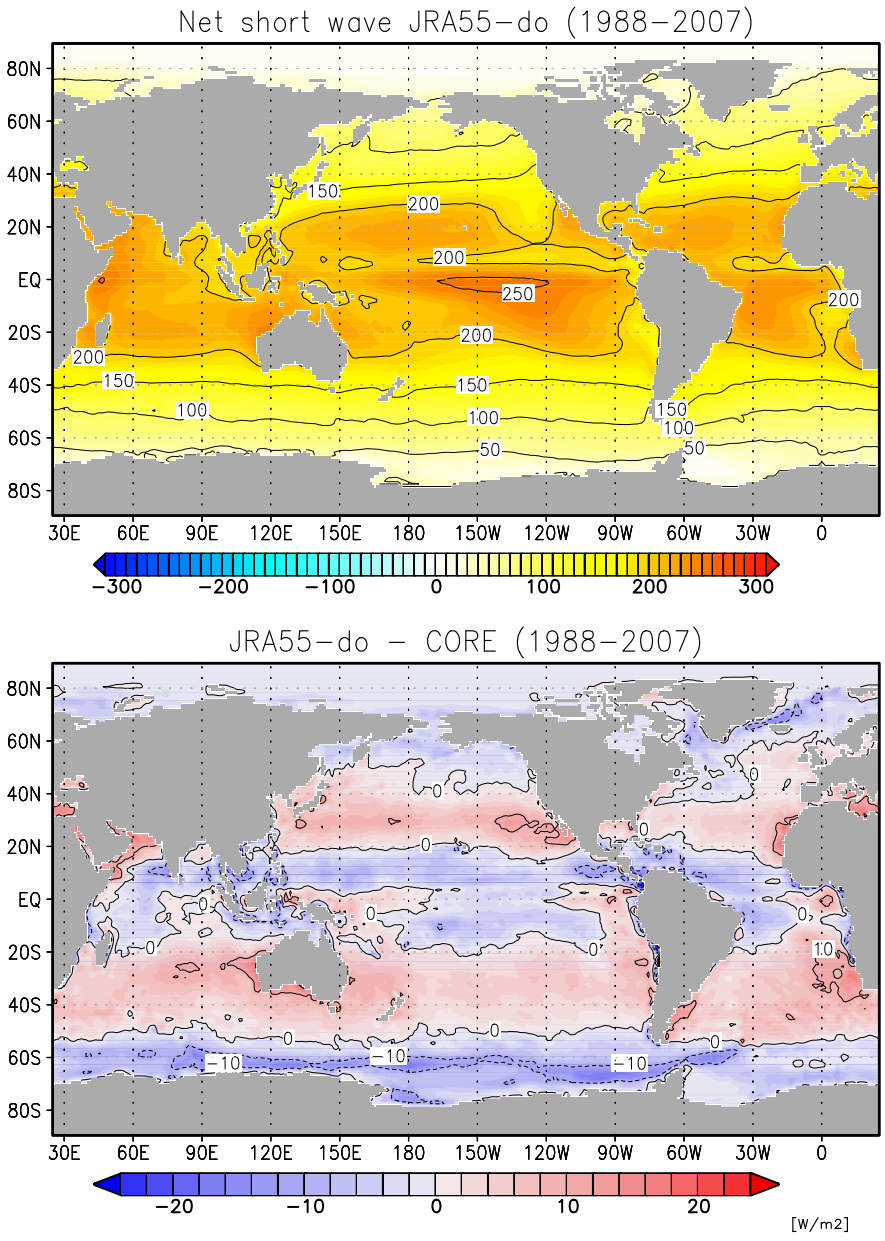

Fig. 49. Same as Fig. 48 but for the net shortwave radiative flux.

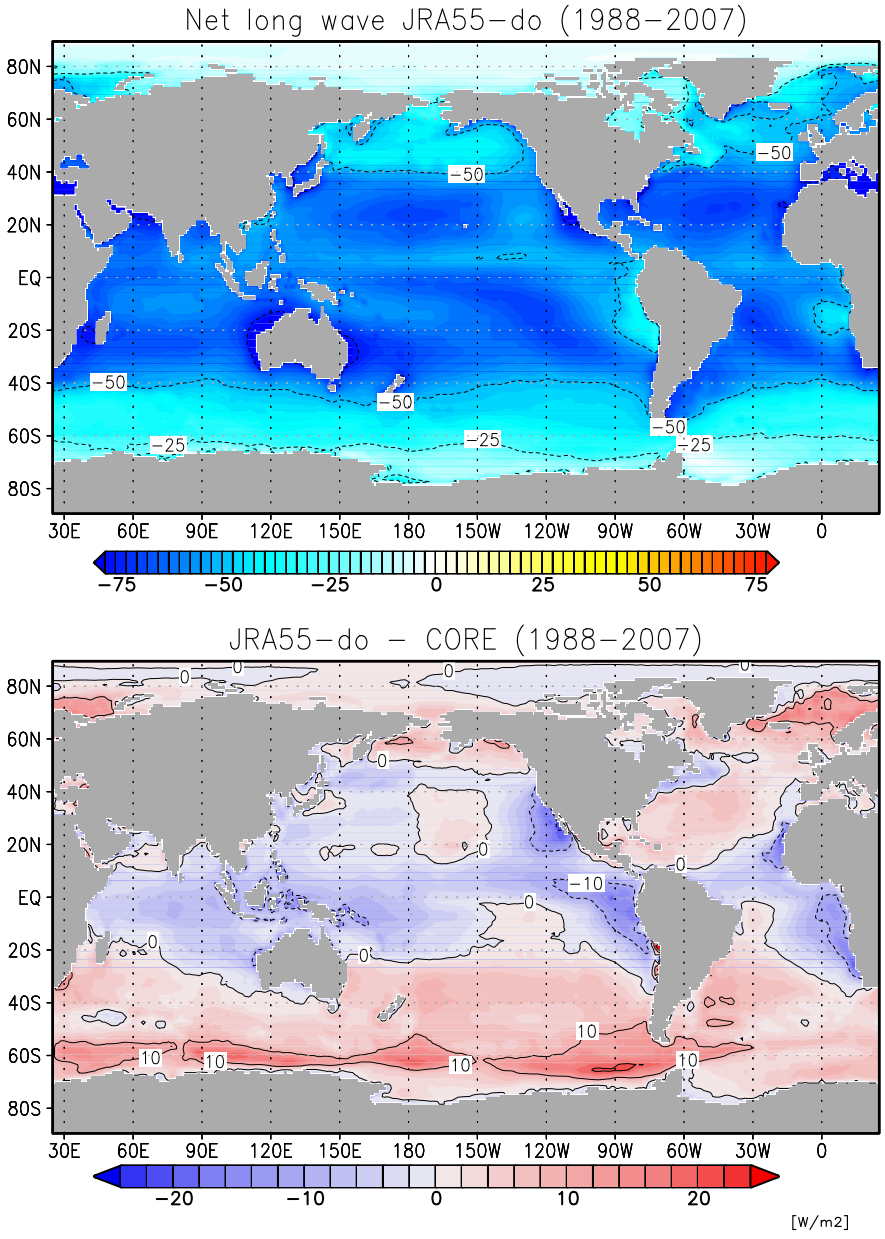

Fig. 50. Same as Fig. 48 but for the net longwave radiative flux.

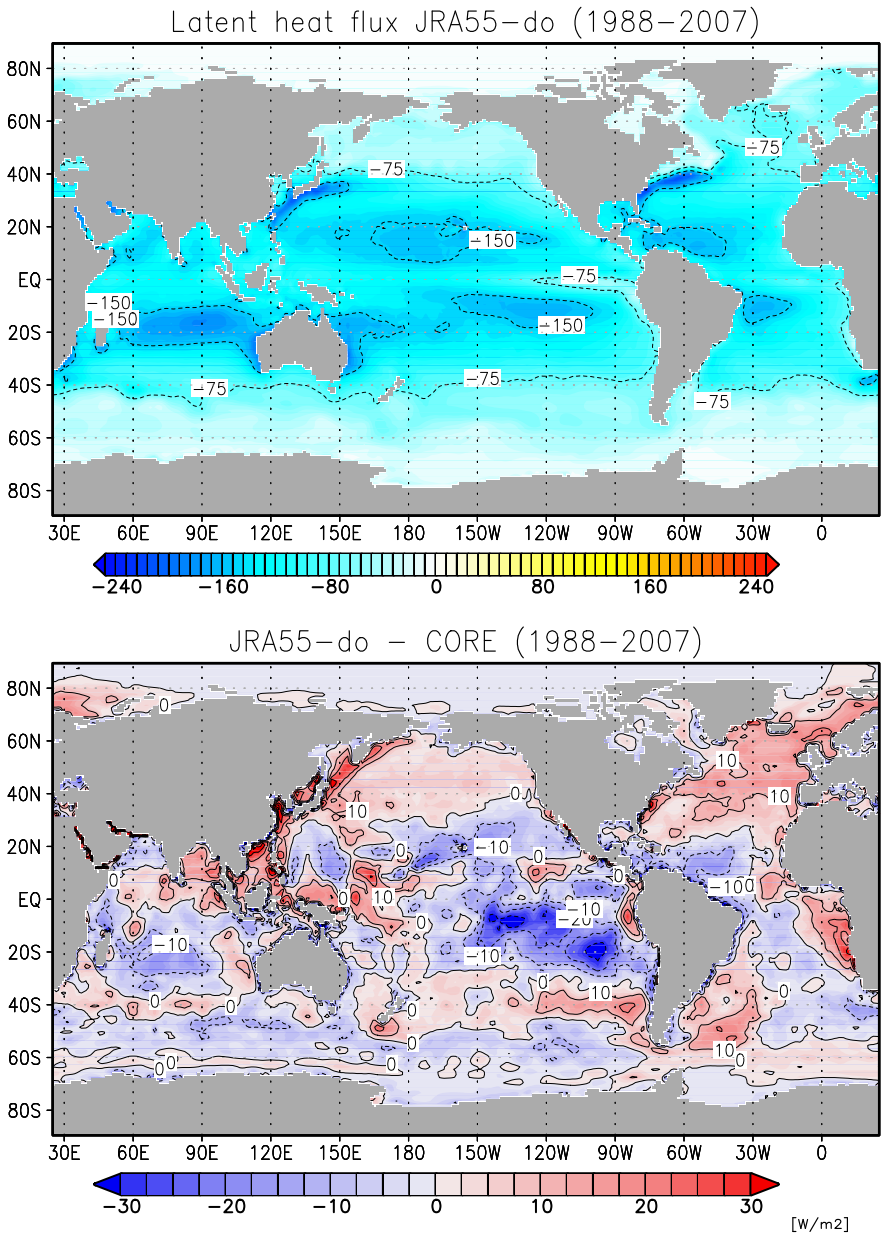

Fig. 51. Same as Fig. 48 but for the latent heat flux.

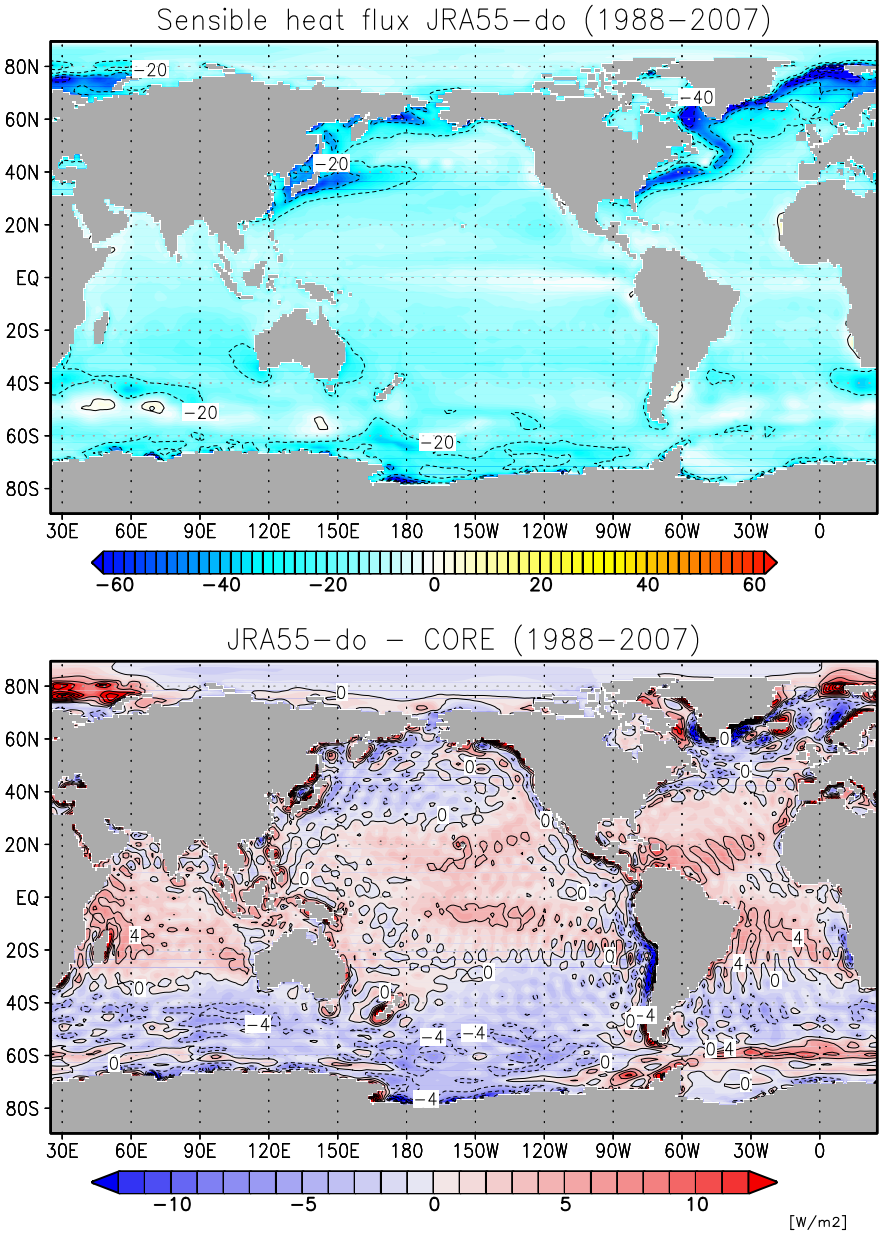

Fig. 52. Same as Fig. 48 but for the sensible heat flux.

G2. Fresh water flux

Figs. 53–Fig. 55 give the global map of the mean (1988–2007) precipitation minus evaporation, evaporation, and precipitation of JRA55-do as well as the difference from those of CORE. The difference of precipitation minus evaporation of JRA55-do relative to CORE tends to be negative (fresh water leaving the ocean) in the tropics and positive in mid-latitudes, specifically in the North Atlantic. This feature is dominated by the evaporation (Fig. 54). Because we applied an approximate enhancement of 2.1% to the precipitation in the final adjustment to impose an exact closure (Section 5), the precipitation of JRA55-do is slightly larger than that of CORE in most regions.

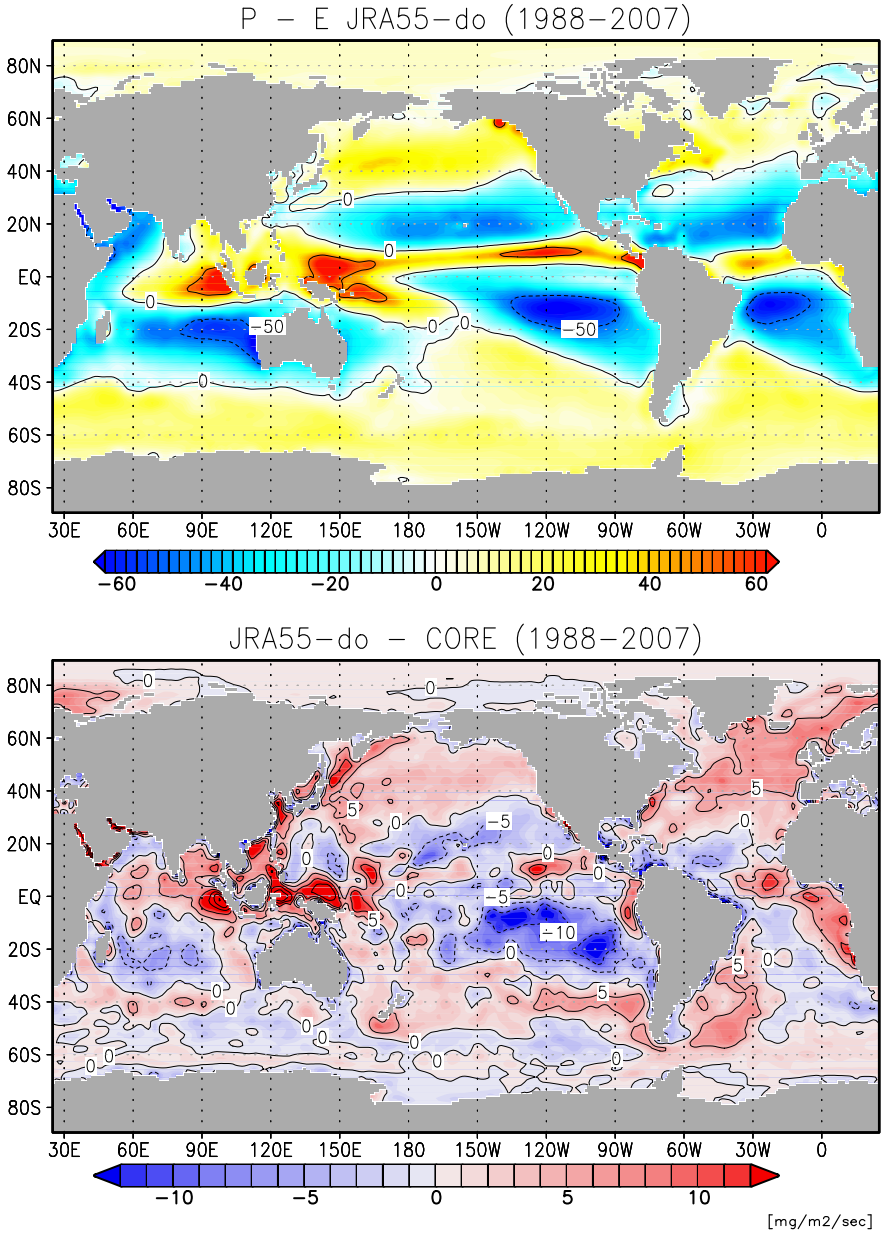

Fig. 53. Comparison of the total surface fresh water flux (the sum of precipitation and evaporation). (upper) Annual mean (1988–2007) of JRA55-do and (lower) anomaly from CORE. Units are mg m^{-2} s^{-1}. Direction is positive into the ocean.

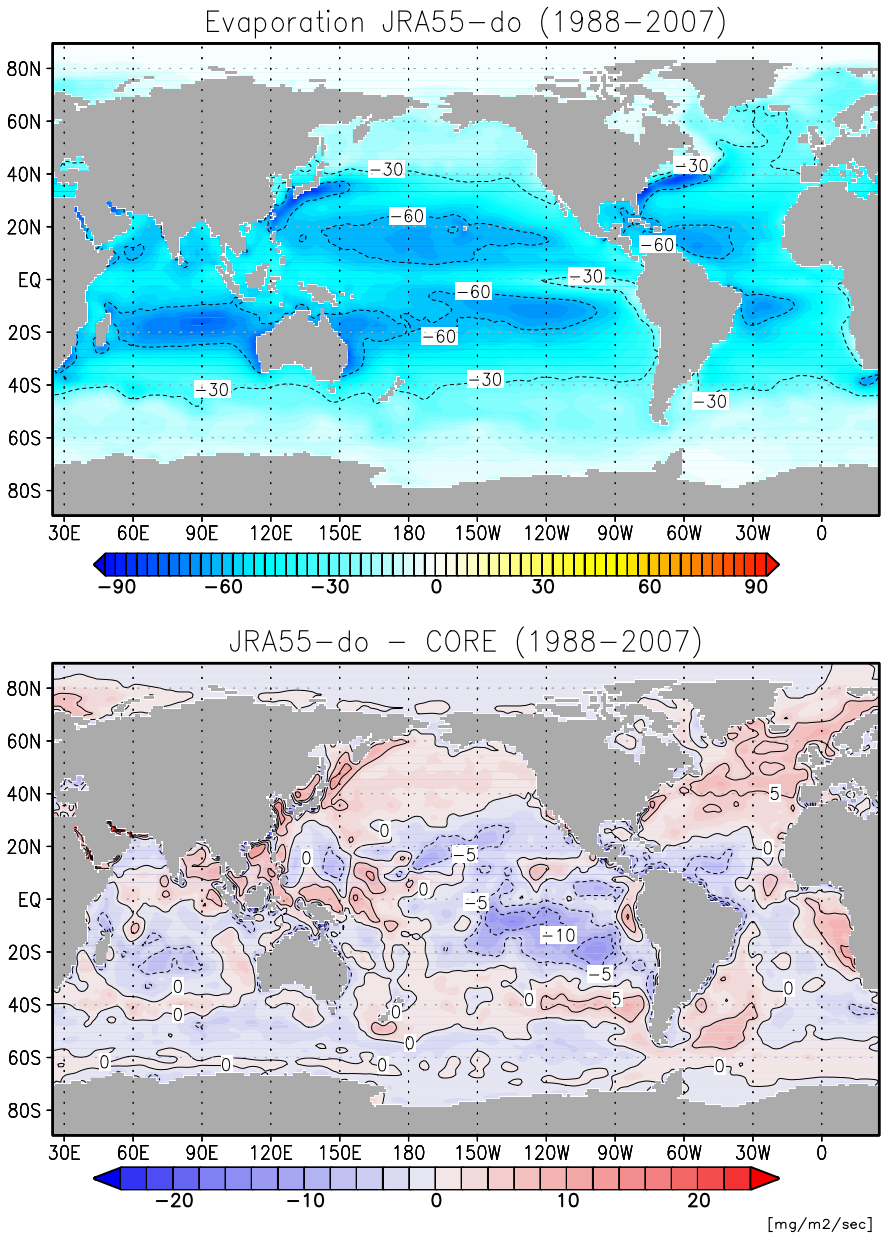

Fig. 54. Same as Fig. 53 but for the evaporation.

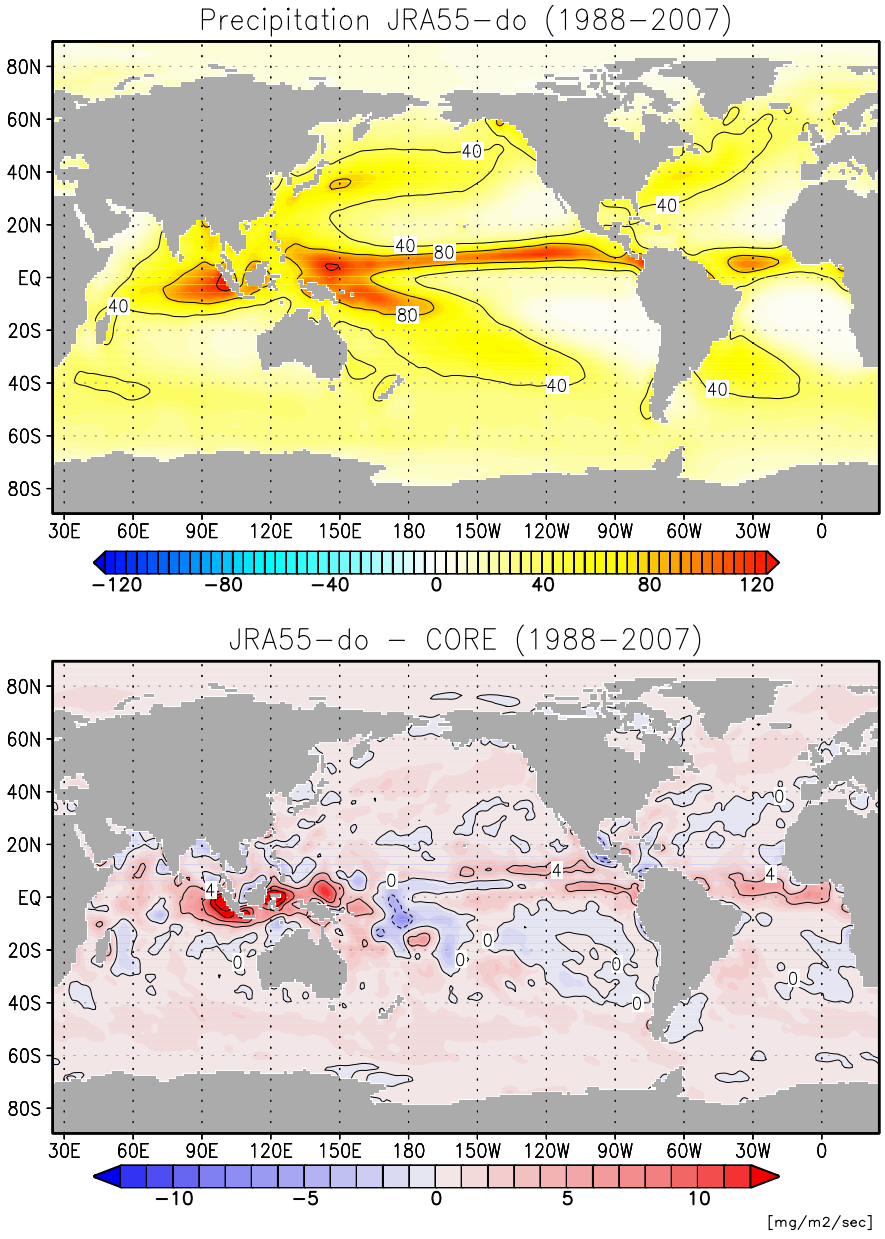

Fig. 55. Same as Fig. 53 but for the precipitation.

G3. Wind stress

Figs. 56 and 57 give the global map of the mean (1988–2007) surface zonal and meridional wind stress of JRA55-do as well as the difference from those of CORE. The wind stress of JRA55-do is weaker than CORE. This is because the equivalent neutral wind from QuikSCAT was directly used to adjust the actual NCEP-R1 wind to produce CORE.

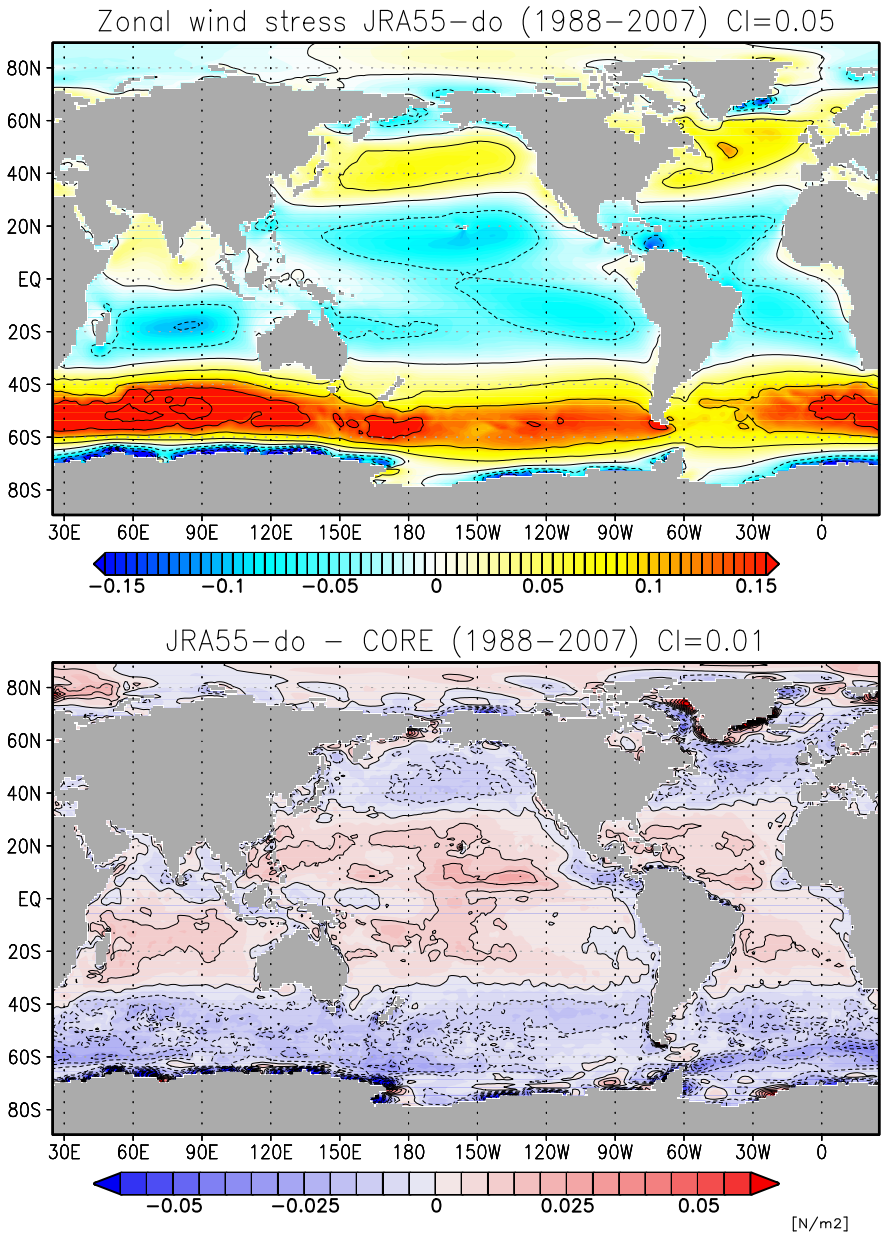

Fig. 56. Comparison of zonal wind stress ($N\,m^{-2}$) on the ocean. (upper) Annual mean (1988–2007) of JRA55-do (contour interval is 0.05 $N\,m^{-2}$) and (lower) anomaly from CORE (contour interval is 0.01 $N\,m^{-2}$).

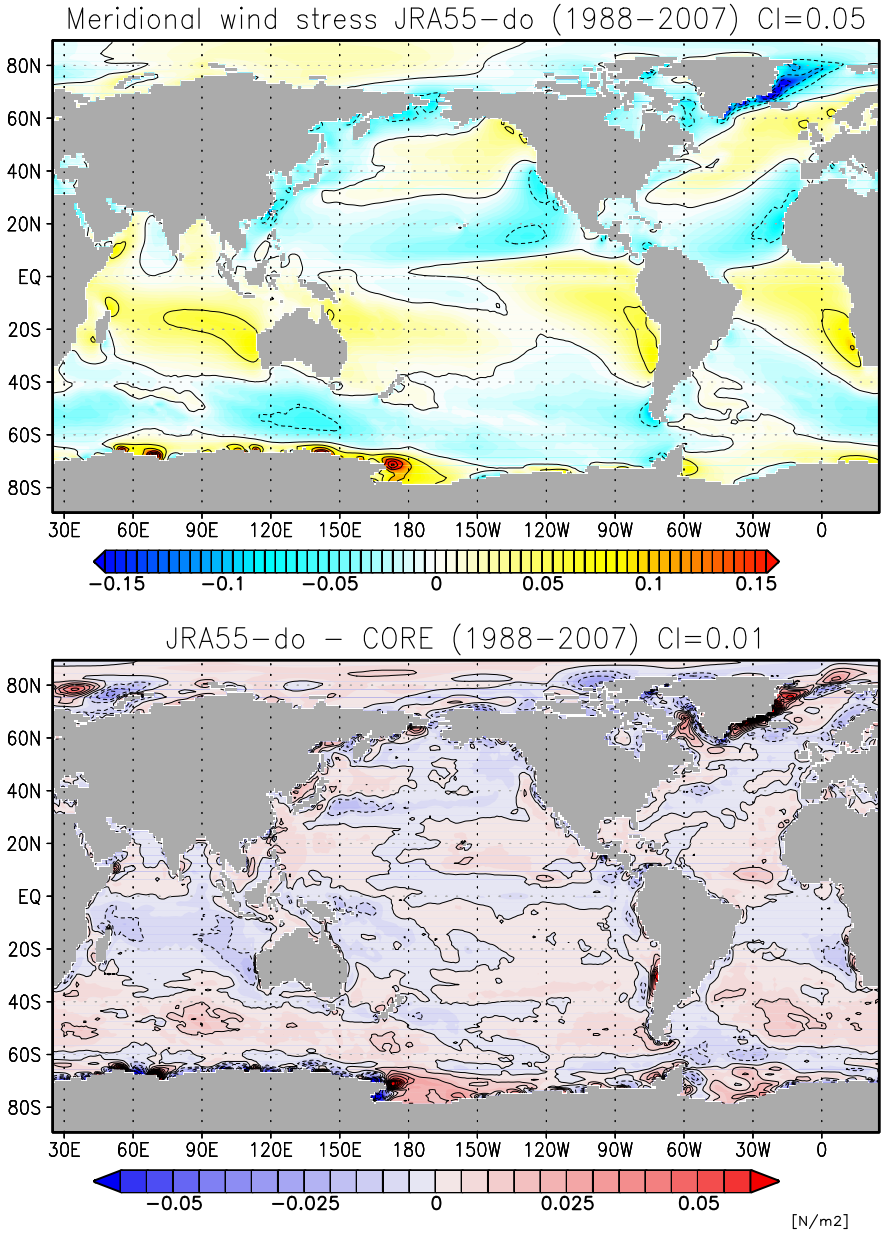

Fig. 57. Same as Fig. 56 but for the meridional wind stress ($N\,m^{-2}$) on the ocean.

Fig. 58 gives the mean (Nov 1999–Oct 2009) wind stress curl of JRA55-do and Scatterometer Oceanic Wind Stress product (SCOW) of Risien and Chelton (2008). JRA55-do reproduces SCOW well, implying that the adjustment on the wind direction was successful, at least in the offshore regions. A more dedicated assessment of the features around the coastal regions is presented in the companion paper (Taboada et al., 2018).

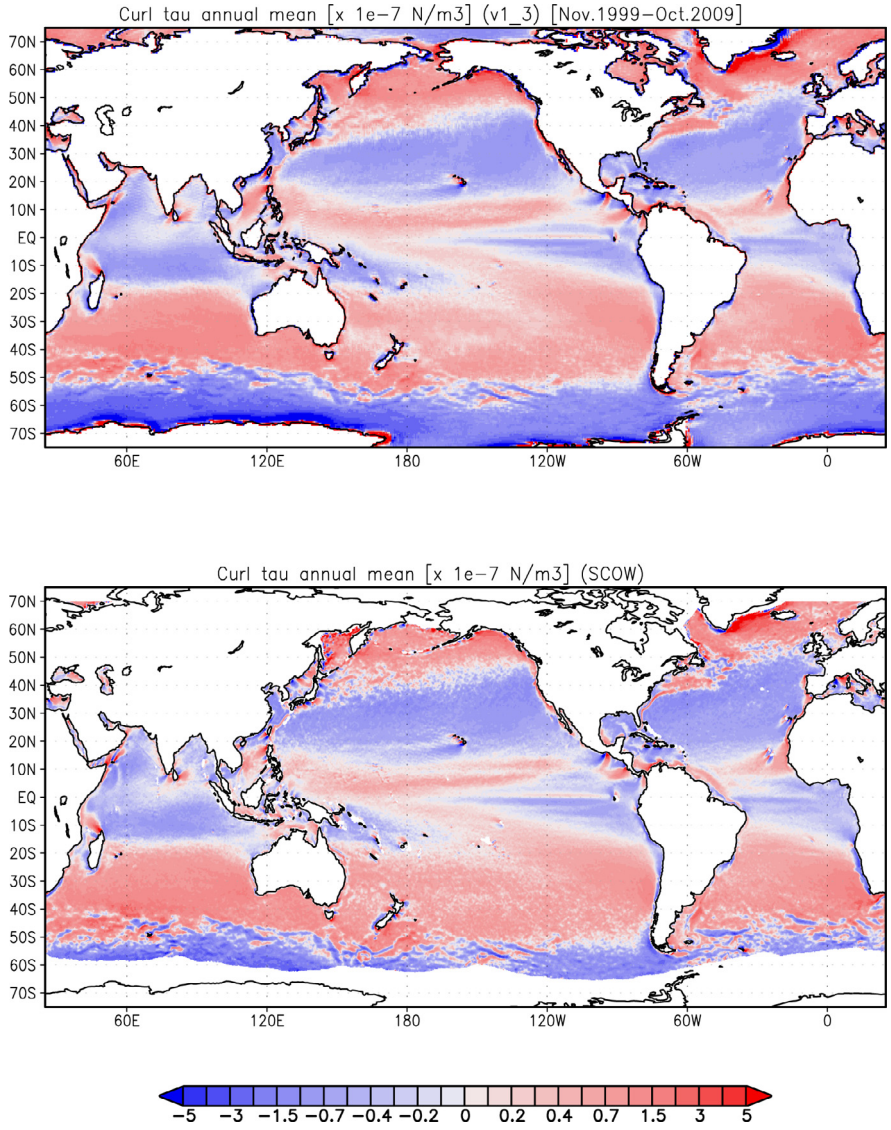

Fig. 58. Comparison of annual mean wind stress curl (Nov1999 - Oct2009) with Scatterometer Oceanic Wind Stress of Risien and Chelton (2008). (upper panel) JRA55-do and (lower panel) Risien and Chelton (2008). Units are N m^{-3}.

References

Abel, R., Böning, C.W., Greatbatch, R.J., Hewitt, H.T., Roberts, M.J., 2017. Feedback of mesoscale ocean currents on atmospheric winds in high-resolution coupled models and implications for the forcing of the ocean-only models. Ocean Sci. Discuss. https://doi.org/10.5194/os-2017-24.

Adler, R.F., Huffman, G.J., Chang, A., Ferrado, R., Xie, P.P., Janowiak, J., Rudolf, B., Schneider, U., Curtis, S., Bolvin, D., Gruber, A., Susskind, J., Arkin, P., Nelkin, E., 2003. The version-2 global precipitation climatology project (GPCP) monthly precipitation analysis (1979-present). J. Hydrometeor. 4, 1147–1166. https://doi.org/10.1175/1525-7541(2003)004<1147:TVGPCP>2.0.CO;2.

Andersson, A., Fenning, K., Klepp, C., Bakan, S., Grassl, H., Shulz, J., 2010. The hamburg ocean atmosphere parameters and fluxs from satellite data - HOAPS-3. Earth Syst. Sci. Data 2, 215–234. https://doi.org/10.5194/essd-2-215-2010.

Bamber, J., van den Broeke, M., Ettema, J., Lenaerts, J., Rignot, E., 2012. Recent large increases in freshwater fluxes from Greenland into the North Atlantic. Geophys. Res. Lett. 39, L19501. https://doi.org/10.1029/2012GL052552.

Bamber, J.L., Tedstone, A.J., King, M.D., Howat, I.M., Enderlin, E.M., van den Broeke, M.R., Noel, B., 2018. Land ice freshwater budget of the Arctic and North Atlantic Oceans: 1. Data, methods and results. J. Geophys. Res. 123, 1827–1837. https://doi.org/10.1002/2017JC013605.

Boyer, T., Locarnini, R.A., Zweng, M.M., Mishonov, A.V., Reagan, J.R., Antonov, J.I., Garcia, H.E., Baranova, O.K., Johnson, D.R., Seidov, D., Biddle, M.M., Hamilton, M., 2015. Changes to calculations of the World Ocean Atlas 2013 for version 2. Technical Report. NOAA. https://data.nodc.noaa.gov/woa/WOA13/DOC/woa13v2_changes.pdf

Brodeau, L., Barnier, B., Treguier, A.-M., Penduff, T., Gulev, S., 2010. An ERA40-based atmospheric forcing for global ocean circulation models. Ocean Model. 31, 88–104. https://doi.org/10.1016/j.ocemod.2009.10.005.

Church, J.A., White, N.J., Konikow, L.F., Domingues, C.M., Cogley, J.G., Rignot, E., Gregory, J.M., van den Broeke, M.R., Monagham, A.J., Velicogna, I., 2011. Revisiting the Earth's sea-level and energy budgets from 1961 to 2008. Geophys. Res. Lett. 38, L18601. https://doi.org/10.1029/2011GL048794.

Compo, G.P., Whitaker, J.S., Sardeshmukh, P.D., Matsui, N., Allan, R.J., Yin, X., Gleason Jr., B.E., Vose, R.S., Rutledge, G., Bessemoulin, P., Brönnimann, S., Brunet, M., Crouthamel, R.I., Grant, A.N., Groisman, P.Y., Jones, P.D., Kruk, M.C., Kruger, A.C., Marshall, G.J., Maugeri, M., Mok, H.Y., Nordli, Ø., Ross, T.F., Trigo, R.M., Wang, X.L., Woodruff, S.D., Worley, S.J., 2011. The twentieth century reanalysis project. Q. J. Roy. Meteorol. Soc. 137, 1–28. https://doi.org/10.1002/qj.776.

Dai, A., Qian, T., Trenberth, K.E., Milliman, J.D., 2009. Changes in continental freshwater discharge from 1948 to 2004. J. Clim. 22, 2773–2792. https://doi.org/10.1175/2008JCLI2592.1.

Danabasoglu, G., Yeager, S.G., Bailey, D., Behrens, E., Bentsen, M., Bi, D., Biastoch, A.,

Böning, C., Bozec, A., Canuto, V.M., Cassou, C., Chassignet, E., Coward, A.C., Danilov, S., Diansky, N., Drange, H., Farneti, R., Fernandez, E., Fogli, P.G., Forget, G., Fujii, Y., Griffies, S.M., Gusev, A., Heimbach, P., Howard, A., Jung, T., Kelley, M., Large, W.G., Leboissetier, A., Lu, J., Madec, G., Marsland, S.J., Masina, S., Navarra, A., Nurser, A.J.G., Pirani, A., Salas y Mélia, D., Samuels, B.L., Scheinert, M., Sidorenko, D., Treguier, A.-M., Tsujino, H., Uotila, P., Valcke, S., Voldoire, A., Wang, Q., 2014. North Atlantic simulations in Coordinated Ocean-ice Reference Experiments phase II (CORE-II). Part I: Mean states. Ocean Model. 73, 76–107. https://doi.org/10.1016/j.ocemod.2013.10.005.

Danabasoglu, G., Yeager, S.G., Kim, W.M., Behrens, E., Bentsen, M., Bi, D., Biastoch, A., Bleck, R., Böning, C., Bozec, A., Canuto, V.M., Cassou, C., Chassignet, E., Coward, A.C., Danilov, S., Diansky, N., Drange, H., Farneti, R., Fernandez, E., Fogli, P.G., Forget, G., Fujii, Y., Griffies, S.M., Gusev, A., Heimbach, P., Howard, A., Ilicak, M., Jung, T., Karspeck, A.R., Kelley, M., Large, W.G., Leboissetier, A., Lu, J., Madec, G., Marsland, S.J., Masina, S., Navarra, A., Nurser, A.J.G., Pirani, A., Romanou, A., Salas y Mélia, D., Samuels, B.L., Scheinert, M., Sidorenko, D., Sun, S., Treguier, A.-M., Tsujino, H., Uotila, P., Valcke, S., Voldoire, A., Wang, Q., Yashayaev, I., 2016. North Atlantic simulations in Coordinated Ocean-ice Reference Experiments phase II (CORE-II). Part II: Inter-annual to decadal variability. Ocean Model. 97, 65–90. https://doi.org/10.1016/j.ocemod.2015.11.007.

Dee, D.P., Uppala, S.M., Simmons, A.J., Berrisford, P., Poli, P., Kobayashi, S., Andrae, U., Balmaseda, M.A., Balsamo, G., Bauer, P., Bechtold, P., Beljaars, A.C.M., van de Berg, L., Bidlot, J., Bormann, N., Delsol, C., Dragani, R., Fuentes, M., Geer, A.J., Haimberger, L., Healy, S.B., Hersbach, H., Hólm, E.V., Isaksen, L., Kållberg, P., Köhler, M., Matricardi, M., McNally, A.P., Monge-Sanz, B.M., Morcrette, J.-J., Park, B.-K., Peubey, C., de Rosnay, P., Tavolato, C., Thépaut, J.-N., Vitart, F., 2011. The ERA-interim reanalysis: configuration and performance of the data assimilation system. Quart. J. Roy. Meteorol. Soc. 137, 553–597. https://doi.org/10.1002/qj.828.

Depoorter, M.A., Bamber, J.L., Griggs, J.A., Lenaerts, J.T.M., Ligtenberg, S.R.M., van den Broeke, M.R., Moholdt, G., 2013. Calving fluxes and basal melt rates of Antarctic ice shelves. Nature 502, 89–92. https://doi.org/10.1038/nature12567.

Downes, S.M., Farneti, R., Uotila, P., Griffies, S.M., Marsland, S.J., Bailey, D., Behrens, E., Bentsen, M., Bi, D., Biastoch, A., Böning, C., Bozec, A., Canuto, V.M., Chassignet, E., Danabasoglu, G., Danilov, S., Diansky, N., Drange, H., Fogli, P.G., Gusev, A., Howard, A., Ilicak, M., Jung, T., Kelley, M., Large, W.G., Leboissetier, A., Long, M., Lu, J., Masina, S., Mishra, A., Navarra, A., Nurser, A.J.G., Patara, L., Samuels, B.L., Sidorenko, D., Spence, P., Tsujino, H., Wang, Q., Yeager, S.G., 2015. An assessment of Southern Ocean water masses and sea ice during 1988 − 2007 in a suite of interannual CORE-II simulations. Ocean Model. 94, 67–94. https://doi.org/10.1016/j.ocemod.2015.07.022.

Farneti, R., Downes, S.M., Griffies, S.M., Marsland, S.J., Behrens, E., Bentsen, M., Bi, D., Biastoch, A., Böning, C., Bozec, A., Canuto, V.M., Chassignet, E., Danabasoglu, G., Danilov, S., Diansky, N., Drange, H., Fogli, P.G., Gusev, A., Hallberg, R.W., Howard, A., Ilicak, M., Jung, T., Kelley, M., Large, W.G., Leboissetier, A., Long, M., Lu, J., Masina, S., Mishra, A., Navarra, A., Nurser, A.J.G., Patara, L., Samuels, B.L., Sidorenko, D., Spence, P., Tsujino, H., Uotila, P., Wang, Q., Yeager, S.G., 2015. An assessment of Antarctic Circumpolar Current and Southern Ocean meridional overturning circulation during 1988 − 2007 in a suite of interannual CORE-II simulations. Ocean Model. 93, 84–120. https://doi.org/10.1016/j.ocemod.2015.07.009.

Gelaro, R., McCarty, W., Suárez, M.J., Todling, R., Molod, A., Takacs, L., Randles, C.A., Darmenov, A., Bosilovich, M.G., Reichle, R., Wargan, K., Coy, L., Cullather, R., Draper, C., Akella, S., Buchard, V., Conaty, A., da Silva, A.M., Gu, W., Kim, G.-K., Koster, R., Lucchesi, R., Merkova, D., Nielsen, J.E., Partyka, G., Pawson, S., Putman, W., Rienecker, M., Schubert, S.D., Sienkiewicz, M., Zhao, B., 2017. The modern-era retrospective analysis for research and applications, version 2 (MERRA-2). J. Clim. 30, 5419–5454. https://doi.org/10.1175/JCLI-D-16-0758.1.

Gill, A.E., 1982. Atmosphere-Ocean Dynamics. Academic Press 662 pp.

Griffies, S.M., Biastoch, A., Böning, C., Bryan, F., Danabasoglu, G., Chassignet, E.P., England, M.H., Gerdes, R., Haak, H., Hallberg, R.W., Hazeleger, W., Jungclaus, J., Large, W.G., Madec, G., Pirani, A., Samuels, B.L., Scheinert, M., Sen Gupta, A., Severijns, C.A., Simmons, H.L., Treguier, A.M., Winton, M., Yeager, S., Yin, J., 2009. Coordinated Ocean-ice Reference Experiments (COREs). Ocean Model. 26, 1–46. https://doi.org/10.1016/j.ocemod.2008.08.007.

Griffies, S.M., Danabasoglu, G., Durack, P.J., Adcroft, A.J., Balaji, V., Böning, C.W., Chassignet, E.P., Curchitser, E., Deshayes, J., Drange, H., Fox-Kemper, B., Gleckler, P.J., Gregory, J.M., Haak, H., Hallberg, R.W., Hewitt, H.T., Holland, D.M., Ilyina, T., Jungclaus, J.H., Komuro, Y., Krasting, J.P., Large, W.G., Marsland, S.J., Masina, S., McDougall, T.J., Nurser, A.J.G., Orr, J.C., Pirani, A., Qiao, F., Stouffer, R.J., Taylor, K.E., Treguier, A.M., Tsujino, H., Uotila, P., Valdivieso, M., Winton, M., Yeager, S.G., 2016. OMIP contribution to CMIP6: experimental and diagnostic protocol for the physical component of the Ocean Model Intercomparison Project. Geosci. Model Dev. 9, 3231–3296. https://doi.org/10.5194/gmd-9-3231-2016.

Griffies, S.M., Yin, J., Durack, P.J., Goddard, P., Bates, S.C., Behrens, E., Bentsen, M., Bi, D., Biastoch, A., Böning, C., Bozec, A., Chassignet, E., Danabasoglu, G., Danilov, S., Domingues, C.M., Drange, H., Farneti, R., Fernandez, E., Greatebatch, R.J., Holland, D.M., Ilicak, M., Large, W.G., Lorbacher, K., Lu, J., Marsland, S.J., Mishra, A., Nurser, A.J.G., Salas y Mélia, D., Palter, J.B., Samuels, B.L., Schröter, Schwarzkopf, F.U., Sidorenko, D., Treguier, A.-M., Tseng, Y.H., Tsujino, H., Uotila, P., Valcke, S., Voldoire, A., Wang, Q., Winton, M., Zhang, X., 2014. An assessment of global and regional sea level for years 1993 − 2007 in a suite of interannual CORE-II simulations. Ocean Model. 78, 35–89. https://doi.org/10.1016/j.ocemod.2014.03.004.

Harada, Y., Kamahori, H., Kobayashi, C., Endo, H., Kobayashi, S., Ota, Y., Onoda, H., Onogi, K., Miyaoka, K., Takahashi, K., 2016. The JRA-55 reanalysis: representation of atmospheric circulation and climate variability. J. Meteor. Soc. Jpn. 94, 269–302. https://doi.org/10.2151/jmsj.2016-015.

Huffman, G.J., Adler, R.F., Arkin, P., Chang, A., Ferraro, R., Gruber, R., Janowiak, J., McNab, A., Rudolf, B., Schneider, U., 1997. The global precipitation climatology project (GPCP) combined precipitation dataset. Bull. Amer. Meteor. Soc. 78, 5–20. https://doi.org/10.1175/1520-0477(1997)078<0005:TGPCPG>2.0.CO;2.

Hurrell, J.W., Hack, J.J., Shea, D., Caron, J.M., Rosinski, J., 2008. A new sea surface temperature and sea ice boundary dataset for the community atmosphere model. J. Clim. 21, 5145–5153. https://doi.org/10.1175/2008JCLI2292.1.

Ilicak, M., Drange, H., Wang, Q., Gerdes, R., Aksenov, Y., Bailey, D.A., Bentsen, M., Biastoch, A., Bozec, A., Böning, C., Cassou, C., Chassignet, E., Coward, A.C., Curry, B., Danabasoglu, G., Danilov, S., Fernandez, E., Fogli, P.G., Fujii, Y., Griffies, S.M., Iovino, D., Jahn, A., Jung, T., Large, W.G., Lee, C., Lique, C., Lu, J., Masina, S., Nurser, A.J.G., Roth, C., Salas y Mélia, D., Samuels, B.L., Spence, P., Tsujino, H., Valcke, S., Voldoire, A., Wang, X., Yeager, S.G., 2016. An assessment of the Arctic Ocean in a suite of interannual CORE-II simulations. Part III: Hydrography and fluxes. Ocean Model. 100, 141–161. https://doi.org/10.1016/j.ocemod.2016.02.004.

Ishii, M., Shouji, A., Sugimoto, S., Matsumoto, T., 2005. Objective analyses of sea-surface temperature and marine meteorological variables for the 20th century using ICOADS and the Kobe Collection. Int. J. Climatol. 25, 865–879. https://doi.org/10.1002/joc.1169.

JMA, 2007. Outline of the Operational Numerical Weather Prediction at the Japan Meteorological Agency. WMO Technical Progress Report on the Global Data-Processing and Forecasting System and Numerical Weather Prediction. JMA, Japan. http://www.jma.go.jp/jma/jma-eng/jma-center/nwp/nwp-top.htm

JMA, 2013. Outline of the Operational Numerical Weather prediction at the Japan Meteorological Agency. WMO Technical Progress Report on the Global Data-Processing and Forecasting System (GDPFS) and Numerical Weather Prediction (NWP) Research. JMA, Japan. http://www.jma.go.jp/jma/jma-eng/jma-center/nwp/nwp-top.htm

Josey, S.A., Yu, L., Gulev, S., Jin, X., Tilinina, N., Barnier, B., Brodeau, L., 2014. Unexpected impacts of the Tropical Pacific array on reanalysis surface meteorology and heat fluxes. Geophys. Res. Lett. 41 (17), 6213–6220. https://doi.org/10.1002/2014GL061302.

Kalnay, E., Kanamitsu, M., Kistler, R., Collins, W., Deaven, D., Gandin, L., Iredell, M., Saha, S., White, G., Woollen, J., Zhu, Y., Chelliah, M., Ebisuzaki, W., Higgins, W., Janowiak, J., Mo, K.C., Ropelewski, C., Wang, J., Leetmaa, A.,, Reynolds, R., Jenne, R., D., Joseph, 1996. The NCEP/NCAR 40-year reanalysis project. Bull. Am. Meteor. Soc. 77, 437–471. https://doi.org/10.1175/1520-0477(1996)077<0437:TNYRP>2.0.CO;2.

Kanamitsu, M., Ebisuzaki, W., Woollen, J., Yang, S.-K., Hnilo, J.J., Fiorino, M., Potter, G.L., 2002. NCEP-DOE AMIP-II Reanalysis (r-2). Bull. Amer. Meteor. Soc. 83, 1631–1643. https://doi.org/10.1175/BAMS-83-11-1631.

Kato, S., Loeb, N.G., Rose, F.G., Doelling, D.R., Rutan, D.A., Caldwell, T.E., Yu, L., Weller, R.A., 2013. Surface irradiances consistent with CERES-derived top-of-atmosphere shortwave and longwave irradiances. J. Clim. 26, 2719–2740. https://doi.org/10.1175/JCLI-D-12-00436.1.

Killworth, P.D., 1996. Time interpolation of forcing fields in ocean models. J. Phys. Oceanogr. 26 (1), 136–143. https://doi.org/10.1175/1520-0485(1996)026<0136:TIOFFI>2.0.CO;2.

Kistler, R., Kalnay, E., Collins, W., Saha, S., White, G., Woollen, J., Chelliah, M., Ebisuzaki, W., Kanamitsu, M., Kousky, V., van den Dool, H., Jenne, R., Fiorino, M., 2001. The NCEP-NCAR 50-year reanalysis: monthly means CD-ROM and documentation. Bull. Amer. Meteor. Soc. 82, 247–267. https://doi.org/10.1175/1520-0477(2001)082<0247:TNNYRM>2.3.CO;2.

Kobayashi, C., Endo, H., Ota, Y., Kobayashi, S., Onoda, H., Harada, Y., Onogi, K., Kamahori, H., 2014. Preliminary results of the JRA-55C, an atmospheric reanalysis assimilating conventional observations only. SOLA 10, 78–82. https://doi.org/10.2151/sola.2014-016.

Kobayashi, S., Ota, Y., Harada, Y., Ebita, A., Moriya, M., Onoda, H., Onogi, K., Kamahori, H., Kobayashi, C., Endo, H., Miyaoka, K., Takahashi, K., 2015. The JRA-55 reanalysis: general specifications and basic characteristics. J. Meteor. Soc. Jpn 93, 5–48. https://doi.org/10.2151/jmsj.2015-001.

Kundu, P.K., Allen, J.S., 1976. Some three-dimensional characteristics of low-frequency current fluctuations near the Oregon coast. J. Phys. Oceanogr. 6, 181–199. https://doi.org/10.1175/1520-0485(1976)006<0181:STDCOL>2.0.CO;2.

Large, W.G., Yeager, S.G., 2004. Diurnal to Decadal Global Forcing for Ocean and Sea-Ice Models: The Data Sets and Flux Climatologies. Technical Note NCAR/TN-460 + STR. CGD Division of the National Center for Atmospheric Research,https://doi.org/10.5065/D6KK98Q6.

Large, W.G., Yeager, S.G., 2009. The global climatology of an interannually varying air-sea flux data set. Clim. Dyn. 33, 341–364. https://doi.org/10.1007/s00382-008-0441-3.

Levitus, S., Antonov, J.I., Boyer, T.P., Baranova, O.K., Garcia, H.E., Lcarnini, R.A., Mishonov, A.V., Reagan, J.R., Seidov, D., Yarosh, E.S., Zweng, M.M., 2012. World ocean heat content and thermosteric sea level change (0 − 2000 m), 1955 − 2010. Geophys. Res. Lett. 39, L10603. https://doi.org/10.1029/2012GL051106.

Lind, R.J., Katsaros, K.B., 1986. Radiation measurements and model results from R/V Oceanographer during STREX 1980. J. Geophys. Res. 91, 13308–13314, https://doi.org/10.1029/JD091iD12p13308.

Lindsay, R., Wensnahan, M., Schweiger, A., Zhang, J., 2014. Evaluation of seven different atmospheric reanalysis products in the Arctic. J. Clim. 27 (7), 2588–2606. https://doi.org/10.1175/JCLI-D-13-00014.1.

Loeb, N.G., Lyman, J.M., Johnson, G.C., Allan, R.P., Doelling, D.R., Wong, T., Soden, B.J., Stephens, G.L., 2012. Observed changes in top of atmosphere radiation and upper ocean heating consistent within uncertainty. Nature Geosci. 5, 110–113. https://doi.org/10.1038/NGEO1375.

Macdonald, A., Baringer, M., 2013. Ocean Heat Transport. Ocean Circulation & Climate: A 21st Century Perspective. International geophysics series 103. Academic Press, pp.

759–785.
McDonagh, E.L., King, B.A., Bryden, H.L., Courtois, P., Szuts, Z., Baringer, M., Cunningham, S.A., Atkinson, C., McCarthy, G., 2015. Continuous estimate of Atlantic oceanic freshwater flux at 26.5°N. J. Clim. 28, 8888–8906. https://doi.org/10.1175/JCLI-D-14-00519.1.
Mitsuyasu, H., 1985. A note on the momentum transfer from wind to waves. J. Geophys. Res. 90 (C2), 3343–3345. https://doi.org/10.1029/JC090iC02p03343.
Paolo, F.S., Fricker, H.A., Padman, L., 2015. Volume loss from Antarctic ice shelves is accelerating. Science 348 (6232), 327–331. https://doi.org/10.1126/science.aaa0940.
Ricciardulli, L., Wentz, F.J., 2015. A scatterometer geophysical model function for climate-quality winds: QuikSCAT Ku-2011. J. Atmos. Oceanic Technol. 32, 1829–1846. https://doi.org/10.1175/JTECH-D-15-0008.1.
Ricciardulli, L., Wentz, F.J., Smith, D.K., 2011. Remote Sensing Systems QuikSCAT Ku-2011 Daily Ocean Vector Winds on 0.25 deg Grid, Version 4. Technical Report. Remote Sensing Systems, Santa Rosa, CA. http://www.remss.com/missions/qscat Accessed 09 Nov 2015
Rigor, I.G., Colony, R.L., Martin, S., 2000. Variations in surface air temperature observations in the Arctic, 1979–97. J. Clim. 13, 896–914. https://doi.org/10.1175/1520-0442(2000)013<0896:VISATO>2.0.CO;2.
Rio, M.H., Mulet, S., Picot, G., 2014. Beyond GOCE for the ocean circulation estimate: Synergetic use of altimetry, gravimetry, and in situ data provides new insight into geostrophic and Ekman currents. Geophys. Res. Lett. 41, 8918–8925. https://doi.org/10.1002/2014GL061773.
Risien, C.M., Chelton, D.B., 2008. A global climatology of surface wind and wind stress fields from eight years of QuikSCAT scatterometer data. J. Phys. Oceanogr. 38, 2379–2413. https://doi.org/10.1175/2008JPO3881.1.
Saha, S., Moorthi, S., Pan, H.-L., Wu, X., Wang, J., Nadiga, S., Tripp, P., Kistler, R., Woollen, J., Behringer, D., Liu, H., Stokes, D., Grumbine, R., Gayno, G., Wang, J., Hou, Y.-T., Chuang, H., Juang, H.-M. H., Sela, J., Iredell, M., Treadon, R., Kleist, D., Van Delst, P., Keyser, D., Derber, J., Ek, M., Meng, J., Wei, H., Yang, R., Lord, S., van den Dool, H., Kumar, A., Wang, W., Long, C., Chelliah, M., Xue, Y., Huang, B., Schemm, J.-K., Ebisuzaki, W., Lin, R., Xie, P., Chen, M., Zhou, S., Higgins, W., Zou, C.-Z., Liu, Q., Chen, Y., Han, Y., Cucurull, L., Reynolds, R.W., Rutledge, G., Goldberg, M., 2010. The NCEP climate forecast system reanalysis. Bull. Am. Meteor. Soc. 91 (8), 1015–1058. https://doi.org/10.1175/2010BAMS3001.1.
Schneider, U., Becker, A., Finger, P., Meyer-Christoffer, A., Rudolf, B., Ziese, M., 2011. GPCC Full Data Reanalysis Version 6.0 at 1.0°: Monthly Land-Surface Precipitation from Rain-Gauges built on GTS-based and Historic Data. Technical Report. Global Precipitation Climatology Centre. https://www.esrl.noaa.gov/psd/data/gridded/data.gpcc.html
Scully, M.E., Trowbridge, J.H., Fisher, A.W., 2016. Observations of the transfer of energy and momentum to the oceanic surface boundary layer beneath breaking waves. J. Phys. Oceanogr. 46, 1823–1837. https://doi.org/10.1175/JPO-D-15-0165.1.
Serreze, M.C., Hurst, C.M., 2000. Representation of mean Arctic precipitation from NCEP-NCAR and ERA reanalyises. J. Clim. 13, 182–201. https://doi.org/10.1175/1520-0442(2000)013<0182:ROMAPF>2.0.CO;2.
Suzuki, T., Yamazaki, D., Tsujino, H., Komuro, Y., Nakano, H., Urakawa, S., 2017. A dataset of continental river discharge based on JRA-55 for use in a global ocean circulation model. J. Oceanogr. 74, 421–429. https://doi.org/10.1007/s10872-017-0458-5.
Taboada, F.G., Stock, C.A., Griffies, S.M., Dunne, J., John, J.G., Small, R.J., Tsujino, H., 2018. Surface winds from atmospheric reanalysis lead to contrasting oceanic forcing and coastal upwelling patterns. Ocean Modell. in revision
Talley, L.D., 2008. Freshwater transport estimates and the global overturning circulation: Shallow, deep and throughflow components. Prog. Oceanogr. 78, 257–303. https://doi.org/10.1016/j.pocean.2008.05.001.
Tomita, H., Kubota, M., Cronin, M.F., Iwasaki, S., Konda, M., Ichikawa, H., 2010. An assessment of surface heat fluxes from J-OFURO2 at the KEO and JKEO sites. J. Geophys. Res. Oceans 115, C03018. https://doi.org/10.1029/2009JC005545.
Tseng, Y., Lin, H., Chen, H.-C., Thompsom, K., Bentsen, M., Böning, C., Bozec, A., Cassou, C., Chassignet, E., Chow, C.H., Danabasoglu, G., Danilov, S., Farneti, R., Fogli, P.G., Fujii, Y., Griffies, S.M., Ilicak, M., Jung, T., Masina, S., Navarra, A., Patara, L., Samuels, B.L., Scheinert, M., Sidorenko, D., Sui, C.-H., Tsujino, H., Valcke, S., Voldoire, A., Wang, X., Yeager, S.G., 2016. North and equatorial Pacific Ocean in CORE-II hindcast simulations. Ocean Model. 104, 143–170. https://doi.org/10.1016/j.ocemod.2016.06.003.
Tsujino, H., Hirabara, M., Nakano, H., Yasuda, T., Motoi, T., Yamanaka, G., 2011. Simulating present climate of the global ocean-ice system using the Meteorological Research Institute Community Ocean Model (MRI.COM): simulation characteristics and variability in the Pacific sector. J. Oceanogr. 67, 449–479. https://doi.org/10.1007/s10872-011-0050-3.
Uppala, S.M., Kållberg, P.W., Simmons, A.J., Andrae, U., Da Costa Bechtold, V., Fiorino, M., Gibson, J.K., Haseler, J., Hernandez, A., Kelly, G.A., Li, X., Onogi, K., Saarinen, S., Sokka, N., Allan, R.P., Andersson, E., Arpe, K., Balmaseda, M.A., Beljaars, A.C.M., Van De Berg, L., Bidlot, J., Bormann, N., Caires, S., Chevallier, F., Dethof, A., Dragosavac, M., Fisher, M., Fuentes, M., Hagemann, S., Hólm, E., Hoskins, B.J., Isaksen, L., Janssen, P.A.E.M., Jenne, R., Mcnally, A.P., Mahfouf, J.-F., Morcrette, J.-J., Rayner, N.A., Saunders, R.W., Simon, P., Sterl, A., Trenberth, K.E., Untch, A., Vasiljevic, D., Viterbo, P., Woollen, J., 2005. The ERA-40 re-analysis. Quart. J. Roy. Meteorol. Soc. 131, 2961–3012. https://doi.org/10.1256/qj.04.176.
Walsh, J.E., Chapman, W.L., 2001. 20th-century sea-ice variations from observational data. Ann. Glaciol. 33, 444–448. https://doi.org/10.3189/172756401781818671.
Wang, Q., Ilicak, M., Gerdes, R., Drange, H., Aksenov, Y., Bailey, D.A., Bentsen, M., Biastoch, A., Bozec, A., Böning, C., Cassou, C., Chassignet, E., Coward, A.C., Curry, B., Danabasoglu, G., Danilov, S., Fernandez, E., Fogli, P.G., Fujii, Y., Griffies, S.M., Iovino, D., Jahn, A., Jung, T., Large, W.G., Lee, C., Lique, C., Lu, J., Masina, S., Nurser, A.J.G., Rabe, B., Roth, C., Salas y Mélia, D., Samuels, B.L., Spence, P., Tsujino, H., Valcke, S., Voldoire, A., Wang, X., Yeager, S.G., 2016. An assessment of Arctic Ocean in a suite of interannual CORE-II simulations. Part I: Sea ice and solid freshwater. Ocean Model. 99, 110–132. https://doi.org/10.1016/j.ocemod.2015.12.008.
Wang, Q., Ilicak, M., Gerdes, R., Drange, H., Aksenov, Y., Bailey, D.A., Bentsen, M., Biastoch, A., Bozec, A., Böning, C., Cassou, C., Chassignet, E., Coward, A.C., Curry, B., Danabasoglu, G., Danilov, S., Fernandez, E., Fogli, P.G., Fujii, Y., Griffies, S.M., Iovino, D., Jahn, A., Jung, T., Large, W.G., Lee, C., Lique, C., Lu, J., Masina, S., Nurser, A.J.G., Rabe, B., Roth, C., Salas y Mélia, D., Samuels, B.L., Spence, P., Tsujino, H., Valcke, S., Voldoire, A., Wang, X., Yeager, S.G., 2016. An assessment of Arctic Ocean in a suite of interannual CORE-II simulations. Part II: Liquid freshwater. Ocean Model. 99, 86–109. https://doi.org/10.1016/j.ocemod.2015.12.009.
Wentz, F.J., 2013. SSM/I Version-7 Calibration Report. Remote Sensing Systems Tech. Rep. 011012. Remote Sensing Systems. http://www.remss.com/missions/ssmi, http://images.remss.com/papers/rsstech/2012_011012_Wentz_Version-7_SSMI_Calibration.pdf
Wijffels, S.E., 2001. Ocean transport of fresh water. Ocean Circulation & Climate. Academic Press, pp. 155–162.
Xie, P., Arkin, P.A., 1996. Analysis of global monthly precipitation using gauge observations, satellite estimates, and numerical model predictions. J. Clim. 9, 840–858. https://doi.org/10.1175/1520-0442(1996)009<0840:AOGMPU>2.0.CO;2.
Yamazaki, D., de Almeida, G.A.M., Bates, P.D., 2013. Improving computational efficiency in global river models by implementing the local inertial flow equation and a vector-based river network map. Water Resour. Res. 49, 7221–7235. https://doi.org/10.1002/wrcr.20552.
Yamazaki, D., Kanae, S., Kim, H., Oki, T., 2011. A physically based description of floodplain inundation dynamics in a global river routing model. Water Resour. Res. 47, W04501. https://doi.org/10.1029/2010WR009726.
Yang, D., 1999. An improved precipitation climatology for the Arctic Ocean. Geophys. Res. Lett. 26, 1625–1628. https://doi.org/10.1029/1999GL900311.
Yoshikawa, Y., Matsuno, T., Marubayashi, K., Fukudome, K., 2007. A surface velocity spiral observed with ADCP and HF radar in the Tsushima Strait. J. Geophys. Res. 112, C06022. https://doi.org/10.1029/2006JC003625.
Yu, L., Weller, R.A., 2007. Objectively analyzed air-sea heat fluxes for the global ice-free oceans (1981–2005). Bull. Amer. Meteor. Soc. 88, 527–540. https://doi.org/10.1175/BAMS-88-4-527.
Zhang, Y., Rossow, W.B., Lacis, A.A., Oinas, V., Mischenko, M.I., 2004. Calculation of radiative fluxes from the surface to the top of atmosphere based on ISCCP and other global data sets: refinements of the radiative transfer model and the input data. J. Geophys. Res. 109, D19105. https://doi.org/10.1029/2003JD004457.
Zweng, M.M., Reagan, J.R., Antonov, J.I., Locarnini, R.A., Mishonov, A.V., Boyer, T.P., Garciad, H.E., Baranova, O.K., Johnson, D.R., Seidov, D., Biddle, M.M., 2013. World Ocean Atlas 2013, Volume 2: Salinity. NOAA Atlas NESDIS 74. NOAA. https://data.nodc.noaa.gov/woa/WOA13/DOC/woa13_vol2.pdf